Diss. ETH Nr. 16424

Structural and chemical analyses of buffer layers in $Cu(In, Ga)Se_2$ thin-film solar cells

A dissertation submitted to the

SWISS FEDERAL INSTITUTE OF TECHNOLOGY ZURICH

for the degree of

DOCTOR OF SCIENCES

presented by

Daniel Abou-Ras

Dipl. Phys., University of Freiburg i.Br., Germany

born on January 20th, 1975

citizen of Germany

Accepted on the recommendation of

Prof. Dr. G. Kostorz, examiner
Prof. Dr. H.P. Strunk, co-examiner
Prof. Dr. A.N. Tiwari, co-examiner

Zurich, 2005

Acknowledgements

In the following, I would like to acknowledge all those persons who helped me to finish the present thesis successfully. I would also like to mention that the present work is the result of a cooperation of the Institute of Applied Physics and the Thin Film Physics Group at the Laboratory for Solid State Physics.

First of all, I would like to thank Prof. Dr. Gernot Kostorz for accepting me as Ph.D. student. Under his guidance, I was able to improve being a physicist in all respects, broaden my knowledge in divers topics and enhance my written style. Also, he supported my participation at various seminars and conferences.
I am very grateful to Prof. Dr. Ayodhya N. Tiwari for employing me in his group and guiding me during my thesis. Very generously, he introduced me from the beginning to the PV society on project meetings and conferences. I learned a lot from him about all kinds of issues concerning the physics in CIGS thin-film solar cells.
I would like to thank Prof. Dr. Horst P. Strunk for acting as a co-examiner of my thesis. His comments were all very helpful in order to improve the quality of my written work.

I am also grateful to

- PD Dr. Hans Zogg for employing me in his laboratory and for various discussions
- Dr. Debashis Mukherji and Prof. Dr. Helge Heinrich for introduction and help with TEM and many other topics
- all current and past members of the Thin-Film Physics group, of those especially to Dr. Dominik Rudmann, David Brémaud, and Dr. Marc Kaelin (thanks for all discussions and sample preparations!), Stefan Siegrist and Thomas Kämpfer (thanks for the help during the installation of the evaporation chamber!), and also to Dr. Alessandro Romeo, Dr. Franz-Josef Haug, Dr. Martin Krejci, Dr. Derk L. Bätzner and Dr. Fedor V. Kurdesau (thanks for various discussions and sample preparations!)
- all current and past members of the Institute of Applied Physics, of those especially to Erwin Fischer (thanks for the work with HF, for help with sample preparation and many other things!), Josef "Joe" Hecht (thanks for all help with the computers!), Ewald Vögele (thanks for the printing support!), Prof. Dr. Bernd Schönfeld, Dr. Alla S. Solugubenko, Dr. Mathias Terheggen and Dr. Myriam Aguirre (thanks for various discussions!), and also to Dr. Rolf Erni, Dr. Michael Portmann-Orlowski and Prof. Dr. Helge Heinrich (thanks for being my running partners!)

- all members of the Electron Microscopy Center of the ETH Zurich, EMEZ, of those especially to Dr. Heinz Gross (thanks for various discussions!), to Dr. Andres Käch (thanks for specimen preparation for SEM and TEM!), and to the participants of the TECNAI users meetings.
- the secretaries of the years 2002-2005: Gaby Strahm, Esther Schilling, Elisabeth Anner, Helga Stettler, and Ursula Huck
- all colleagues from various laboratories joining the EU-projects PROCIS and NEBULES, of those especially to Prof. Dr. Hans-Werner Schock, Dr. Andreas Strohm, Lorenz Eisenmann, Dr. Dimitri Hariskos, Stefanie Spiering, Dr. Michael Powalla, Dr. Richard Menner, Dr. Konrad Herz, Charlotte Platzer-Björkman, Dr. Susanne Siebentritt, Dr. Olga Papathanasiou, Dr. Nicolas Barreau and Prof. Dr. John Kessler
- Dr. Nicolas Allsop, HMI, Berlin, Germany, for providing the Spray-ILGAR-In_xS_y samples and for various discussions
- Dr. Thomas Schlenker, IPE, Stuttgart, Germany, for the hints on the evaluation of optical measurements.

Special thanks are due to

- Peter Wägli for the SEM measurements
- Roland Wessiken and Peter Tittmann for all the technical support at the transmission electron microscopes
- Dr. Max Döbeli and Dr. Christian Kottler for RBS and ERDA measurements
- Dr. Michael Wörle, Prof. Dr. Bernd Schönfeld, Marije van der Klis and Dr. David Sager for XRD measurements
- Paolo Losio for the help with the transmission and reflection measurements
- Dr. Elisabeth Müller and Dr. Mathias Terheggen for introduction into and help with TEM sample preparation and also with the work at the microscope

Particularly, I would like to acknowledge my two dear room mates and fellow Ph.D. students, Marije van der Klis and Fabio Krogh. I am grateful for the wonderful time in D18 with various discussions inside and outside of physics.
I am also grateful to various friends from all over the world who helped me to forget about physics for a while, every now and then...
Last but not least, I would like to thank my parents for continuous support during my studies, my sister Melanie for supporting and tolerating her brother and finally my dear Cíntia for everything she has given to me.

Contents

Summary

In the work presented in this thesis, thin-film solar cells based on $Cu(In, Ga)Se_2$ (CIGS) absorbers have been studied. Although the technical development of these solar cells has already reached a level sufficiently mature to enter into pilot and mass production, many questions remain unsolved, various phenomena can not be explained, and even more questions and phenomena arise from the further development of CIGS solar cells. The present thesis is dedicated to give answers and reasons for at least some of those questions and phenomena.
Since the p-n heterojunction in CIGS thin-film solar cells is formed at the interface between the p-type CIGS absorber and the n-type buffer layer (or at least close to this interface), the buffer/CIGS interface is also most important for the performance of a CIGS solar cell. The present thesis thus concentrates mainly on the study of CIGS/buffer interfaces in order to reveal their structural and chemical properties, to learn more about the effects of various parameters on interdiffusion at these interfaces and on the growth of the corresponding layers.

In order to study both, structural and chemical properties, of interfaces within one instrument, transmission electron microscopy and its related techniques provide powerful tools. The possibility to image areas of interest down to the angstrom scale and to perform chemical measurements with a similarly high accuracy provides the means for a careful investigation of all kinds of structural and chemical features, such as lattice match, orientation relationships or diffusion of elements.
By the help of these analyses, possible causes for the behavior of the solar-cell performance under variation of divers parameters and treatments - the substrate temperature and the presence of Na during the buffer-layer growth, and also the annealing in air of complete cells - were given. Cells with CdS buffer layers grown by chemical bath (CBD) and by physical vapor deposition (PVD) as well as cells with In_xS_y buffer layers grown by atomic layer deposition (ALD), by co-evaporation from the elements, by compound evaporation from In_2S_3 powder and by sputtering were studied. In addition, the possibility to apply $MoSe_2$ as a buffer layer between CIGS and a transparent conductive oxide (TCO) back contact was explored, and various parameters of the $MoSe_2$ growth were varied in order to optimize the $MoSe_2$

properties for a tunnelling quasi-ohmic contact.

As-grown CIGS solar cells with CBD-CdS buffers always show a higher efficiency than those with PVD-CdS buffers. It was shown that PVD-CdS layers exhibit much higher densities of structural defects at the CIGS/PVD-CdS interface than CBD-CdS at the CIGS/CBD-CdS interface, owing to a larger lattice mismatch at the CIGS/PVD-CdS interface. These defects may affect on the photovoltaic performance. For PVD-CdS, the interface to CIGS is quite abrupt, whereas on the CIGS side of the CBD-CdS/CIGS interface, Cu depletion and Cd enrichment have occurred. In addition, Cu diffuses to a large extent into CdS. Cu increases the photoconductivity of CdS, and Cd can occupy Cu vacancies in the CIGS layer near to the CIGS/CdS interface. This Cu-depleted and Cd-enriched near-interface region may enhance the band alignment between CIGS and CBD-CdS. The absence of such a region in as-grown solar cells with PVD-CdS buffer layers is a possible reason for their lower efficiencies compared with CBD-CdS-buffered solar cells.

CIGS solar cells with In_xS_y buffer layers produced by ALD and sputtering show increasing efficiencies with increasing In_xS_y deposition temperature up to about 230 °C. Interfaces between CIGS and these In_xS_y buffers deposited at temperatures ranging from about 60 to 230 °C were studied. Results from energy-dispersive x-ray spectrometry (EDX) exhibit interdiffusion of Cu, Ga and In across In_xS_y/CIGS interfaces. The Cu depletion and In enrichment found on the CIGS side of these interfaces may indicate the presence of an intermediate Cu-depleted Cu-(In,Ga)-Se layer between CIGS and In_xS_y (similar as at the CBD-CdS/CIGS interface). The width of this layer apparently increases with increasing temperature, as the Cu depletion and In enrichment are more enhanced at elevated temperature. Such an intermediate, Cu-depleted Cu-(In,Ga)-Se layer may considerably improve the band alignment between CIGS and In_xS_y and thus the solar-cell performance.

For complete solar cells with In_xS_y buffers evaporated from In_2S_3 powder, air-annealing at 200 °C for several minutes leads to an enhanced Cu diffusion from CIGS into In_xS_y and to a significant Cu depletion on the CIGS side of the interface. Air-annealing may reduce the anion defects and induces the formation of a compositionally graded In_xS_y/CIGS interface. A Cu-depleted and In-rich Cu-(In,Ga)-Se layer on the CIGS side of the interface may form, induced by the air-annealing, improving the band alignment between CIGS and In_xS_y and thus the solar-cell performance.

For substrate temperatures above about 250 °C, the deposition of In_xS_y on CIGS by any technique led to the formation of $CuIn_5S_8$. Its impact on the band alignment is not yet clear. However, the intrinsically large densities of vacancies and

planar defects - probably stacking faults and twins - of this layer may affect recombination of the generated charges, and thus reduce considerably the efficiency of the solar cell.

Na was shown to affect the growth of ALD-In_2S_3 buffers on CIGS considerably. Quantum efficiency spectra revealed smaller carrier collection and short-circuit current densities for Na free solar cells. As shown by EDX, Cu and Ga diffusion from CIGS into In_2S_3 are clearly enhanced in these cells. These results indicate that both, Cu and Na, diffuse into the In_2S_3 layer, occupying In sites and vacancies. Probably, the enhanced Cu diffusion from CIGS into In_2S_3 for Na free solar cells deteriorates the electrical and optical properties of the CIGS/In_2S_3 interface and of the In_2S_3 buffer layer, which lowers the overall performance of the solar cells.

The formation of $MoSe_2$ by selenization of polycrystalline Mo layers and Mo single crystals was studied in dependence of the substrate temperature, the Mo crystal orientation and the Na concentration. For all $MoSe_2$ layers, a hexagonal crystal structure was found. It was shown that a $MoSe_2$ layer formed at 450 °C has a *c*-axis oriented preferably perpendicular to the Mo surface, whereas at 580 °C, the *c*-axis is oriented preferably parallel to the Mo surface. The smaller $MoSe_2$ layer thickness at 450 °C can be explained by a Se diffusion through $MoSe_2$ impeded by a *c*-axis orientation perpendicular to the Mo surface. For the $MoSe_2$ growth at 450 and 580 °C, Na appears to induce a *c*-axis orientation perpendicular to the Mo surface. The orientation of the Mo substrate has no influence on the preferred orientation of $MoSe_2$. Both, the $MoSe_2$ layer thickness and the Mo grain size, are affected by the oxygen concentration in Mo prior to the selenization.

Zusammenfassung

Im Rahmen der vorliegenden Doktorarbeit wurden auf $Cu(In, Ga)Se_2$ (CIGS)-Absorber basierende Dünnschichtsolarzellen untersucht. Obwohl die Entwicklung dieser Zellen bereits so weit fortgeschritten ist, dass mit der Pilot- und Massenproduktion begonnen werden konnte, sind immer noch viele Fragen unbeantwortet, viele Phänomene können nicht erklärt werden, und immer mehr Fragen und Phänomene tauchen bei der weiter andauernden Entwicklung der CIGS-Solarzellen auf.
Da der p-n-Heteroübergang in CIGS-Dünnschichtsolarzellen an der Grenzfläche (oder zumindest in deren Nähe) zwischen dem p-leitenden CIGS-Absorber und der n-leitenden Pufferschicht gebildet wird, ist diese Grenzfläche auch die wichtigste in diesen Zellen. In der vorliegenden Doktorarbeit wird deshalb hauptsächlich von der Untersuchung an CIGS/Puffer-Grenzflächen berichtet, deren strukturelle und chemische Eigenschaften es zu ermitteln gilt, um mehr über die Einflüsse verschiedener Parameter auf Interdiffusionsprozesse an diesen Grenzflächen und auf das Wachstumsverhalten der entsprechenden Schichten zu lernen.

Um sowohl die strukturellen als auch die chemische Eigenschaften von Grenzflächen in CIGS-Solarzellen innerhalb nur einer Messapparatur zu untersuchen, stellen die Transmissionselektronenmikroskopie und ihre zugehörigen Messtechniken leistungsfähige Instrumente dar. Die Möglichkeit, interessante Gebiete einer Probe bis in den Ångström-Bereich abzubilden und chemische Messungen mit einer ähnlich hohen räumlichen Auflösung durchzuführen, erlaubt eine sehr genaue Untersuchung von vielen verschiedenen strukturellen und chemischen Merkmalen wie zum Beispiel Gitteranpassung, Orientierungsbeziehungen und Diffusion von Elementen.
Mit Hilfe dieser Analysen war es möglich, Ursachen für das Leistungsverhalten der CIGS-Solarzellen unter Variation von verschiedenen Herstellungsparametern und -behandlungen (der Substrattemperatur und das Vorhandensein von Na während des Pufferschichtwachstums, sowie das Tempern von fertigestellten Zellen) anzugeben. Es wurden CIGS-Solarzellen mit CdS-Pufferschichten untersucht, die entweder durch Abscheidung im chemischen Bad (chemical bath deposition, CBD)

oder durch Verdampfen von CdS-Pulver (physical vapor deposition, PVD) hergestellt wurden, und auch Zellen mit In_xS_y-Pufferschichten, welche mittels Atomlagendeposition (atomic layer deposition, ALD), Verdampfen von In- und S-Pulver, Verdampfen von In_2S_3-Pulver oder Sputtering produziert wurden. Zusätzlich wurde die Möglichkeit ausgewertet, $MoSe_2$ als Pufferschicht zwischen CIGS und einem Rückkontakt einzusetzen, der durch ein transparentes, leitfähiges Oxid (transparent conductive oxide, TCO) gebildet wird. Zahlreiche Parameter des $MoSe_2$-Wachstums wurden variiert, um die Eigenschaften der $MoSe_2$-Schicht als quasi-ohmschen Tunnelkontakt zu optimieren.

Unbehandelte CIGS-Solarzellen mit CBD-CdS-Puffern haben immer einen höheren Wirkungsgrad als diejenigen mit PVD-CdS-Puffern. Es konnte gezeigt werden, dass PVD-CdS-Pufferschichten eine viel höhere Defektdichte an der CIGS/PVD-CdS-Grenzfläche aufweisen als CBD-CdS-Puffer an der Grenzfläche zu CIGS, wahrscheinlich wegen der grösseren Gitterfehlpassung. Diese Defekte können einen Einfluss auf die Leistung der Solarzelle haben. Die PVD-CdS/CIGS-Grenzfläche verläuft eher abrupt, während die CIGS-Seite der CBD-CdS/CIGS-Grenzfläche Cu verarmt und Cd angereichert ist. Ausserdem ist Cu in grossem Masse in die CdS-Schicht hineindiffundiert. Cu erhöht die Fotoleitfähigkeit des CdS, und Cd kann Cu-Leerstellen in der CIGS-Schicht nahe der CIGS/CdS-Grenzfläche besetzen. Diese an Cu verarmte und Cd-angereicherte Schicht in der Nähe der Grenzfläche könnte die Energiebandanpassung zwischen CIGS und CBD-CdS verbessern. Das offenbare Fehlen einer solchen intermediären Schicht im Falle von unbehandelten Solarzellen mit PVD-CdS-Puffern ist ein möglicher Grund für deren geringere Solarzellenleistung, verglichen mit CBD-CdS-gepufferten Solarzellen.

CIGS-Solarzellen mit In_xS_y-Puffern, die mittels ALD oder Sputtering hergestellt wurden, weisen steigende Wirkungsgrade mit steigender In_xS_y-Depositionstemperatur bis zu Werten von etwa 230 °C auf. Grenzflächen zwischen In_xS_y-Pufferschichten, welche bei Temperaturen zwischen 60 und 230 °C hergestellt wurden, und CIGS wurden untersucht. Ergebnisse von energiedispersiven Röntgenspektrometriemessungen (energy-dispersive x-ray spectrometry, EDX) zeigen Interdiffusion von Cu, In und Ga über die In_xS_y/CIGS-Grenzfläche hinweg. Die Cu-Verarmung und In-Anreicherung auf der CIGS-Seite der Grenzfläche deuten eine Cu-verarmte Cu-(In,Ga)-Se-Schicht zwischen CIGS und In_xS_y an (ähnlich wie bereits an der CBD-CdS/CIGS-Grenzfläche). Offensichtlich verbreitert sich die diese Schicht mit ansteigender Substrattemperatur, da die Cu-Verarmung und In-Anreicherung bei höherer Temperatur verstärkt sind. Ein solche Cu-verarmte, intermediäre Cu-(In,Ga)-Se-Schicht könnte erheblich zu einer verbesserten Energiebandanpassung zwischen CIGS und In_xS_y und somit zu einer Verbesserung der Solarzellenleistung beitragen.

Das Tempern an Luft von fertiggestellten Solarzellen mit In_xS_y-Pufferschichten, welche durch Verdampfen von In_2S_3-Pulver hergestellt wurden, führt zu einer verstärkten Cu-Diffusion vom CIGS ins In_xS_y und zu einer signifikanten Cu-Verarmung auf der CIGS-Seite der Grenzfläche. Dieser Temperschritt könnte Anionendefekte verringern und ruft eine von der Zusammensetzung her abgestufte Grenzfläche hervor. Es könnte sich eine Cu-verarmte und In-angereicherte Cu-(In,Ga)-Se-Schicht auf der CIGS-Seite der Grenzfläche ausbilden, welche die Energiebandanpassung zwischen CIGS und In_xS_y verbessert und somit die Leistung der Solarzellen.

Für Substrattemperaturen über etwa 250 °C führte die Abscheidung von In_xS_y auf CIGS, unabhängig von der Herstellungstechnik des In_xS_y, zur Bildung von $CuIn_5S_8$. Der Einfluss dieser Schicht auf die Energiebandanpassung zwischen CIGS und Pufferschicht ist noch nicht geklärt, jedoch können die hohen Dichten an intrinsischen Leerstellen und die strukturellen Defekte der $CuIn_5S_8$-Schicht die Rekombination von erzeugten Ladungen beeinflussen, und somit zu der gemessenen, verschlechterten Leistung der Solarzelle beitragen.

Es wurde gezeigt, dass Na das Wachstum von ALD-In_2S_3-Pufferschichten massgeblich beeinflusst. Quanteneffizienzspektren zeigen eine verminderte Ladungsträgersammlung und Kurzschlussstromdichten für Na-freie Solarzellen. Wie durch EDX gezeigt wurde, sind die Cu- und auch die Ga-Diffusion vom CIGS ins In_2S_3 für diese Zellen deutlich erhöht. Diese Resultate deuten an, dass Cu und Na beide von der CIGS- in die In_2S_3-Schicht diffundieren und dort Leerstellen und In-Gitterplätze besetzen. Wahrscheinlich verschlechtert die erhöhte Cu-Diffusion vom CIGS ins In_2S_3 für Na-freie Solarzellen die elektrischen und optischen Eigenschaften der CIGS/In_2S_3-Grenzfläche und auch die der In_2S_3-Schicht, was die Leistung der Solarzelle insgesamt herabsetzt.

Die Bildung von $MoSe_2$ mittels Selenisieren von polykristallinen Mo-Schichten und Mo-Einkristallen wurde in Abhängigkeit von der Substrattemperatur, der Mo-Kristallorientierung und der Na-Konzentration untersucht. Alle $MoSe_2$-Schichten wiesen eine hexagonale Kristallstruktur auf. Es wurde für eine bei 450 °C hergestellte $MoSe_2$-Schicht gezeigt, dass deren *c*-Achse im Mittel senkrecht zur Mo-Oberfläche steht. Bei 580 °C liegt die *c*-Achse im Mittel parallel zur Mo-Oberfläche. Die deutlich kleinere $MoSe_2$-Schichtdicke der bei 450 °C hergestellten Probe kann dadurch erklärt werden, dass eine senkrecht zur Mo-Oberfläche orientierte *c*-Achse die Se-Diffusion durch die $MoSe_2$-Schicht zur $MoSe_2$/Mo-Grenzfläche deutlich behindert und somit das $MoSe_2$-Wachstum erheblich verlangsamt. Na scheint eine Orientierung der *c*-Achse senkrecht zur Mo-Oberfläche bei 450 wie auch bei 580 °C hervorzurufen. Die Orientierung des Mo-Substrats hat keinen Einfluss auf die

Orientierung der $MoSe_2$-Schicht. Die Sauerstoffkonzentration in den Proben beeinflusst die $MoSe_2$-Schichtdicke und auch die Mo-Korngrösse massgeblich.

Chapter 1

Introduction

1.1 Research and development in photovoltaics

The starting point of the research and development of solar cells was set by the discovery of the photovoltaic effect by the French experimental physicist Aléxandre Edmond Becquerel in 1839 [1]. Together with his father, he found that the current between two metal plates immersed into hydrochloric acid shows a higher value when these plates are exposed to outdoor sun light than if they are kept in the laboratory. Over the following years, more materials exposing photovoltaic effects were revealed, e.g., selenium, and the first "solar cell" was produced in 1877 by W.G. Adams and R.E. Day [2], who studied junctions formed by selenium plates and platinum wires. This "solar cell" as well as others presented until the 1950s showed conversion efficiencies of well below 1%, thus, these cells could not have been used as efficient sources of electrical energy.

The first solar cells yielding efficiencies of about 6% [3] were developed in 1954 by D.M. Chapin, C.S. Fuller and G.L. Pearson at the Bell Laboratories, USA, based on silicon wafers from crystals produced by the Czochralski process. Such "solar batteries", as they were called in these days, were used as power supplies for rural telephone lines by the Bell Telephone System company in Georgia, USA, substituting regular batteries (Fig. 1.1). However, these novel cells were still rather expensive compared with other electrical energy sources. If there had not been a need for independent electrical power sources for space applications, the research and development of solar cells would have never been performed as rapidly as it has been during the last 50 years. Urged by the competition between Russia and the United States about the dominance in space, various satellite programs were conducted, and first satellites were successfully launched into earth orbit in 1957. Since then, it would not have been possible to realize countless satellite and space

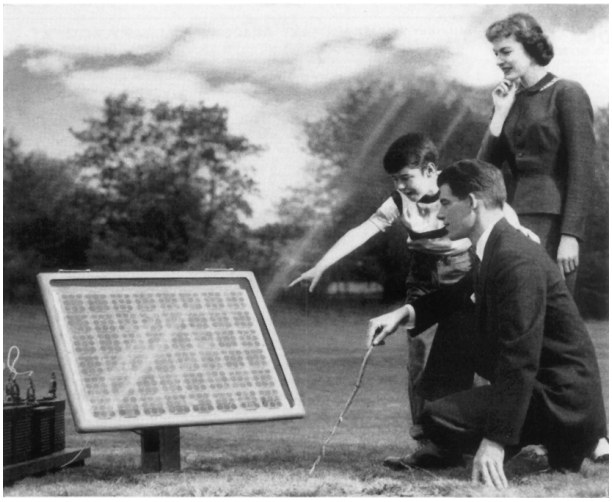

Figure 1.1: Magazine advertisement by the Bell Telephone system in 1954. (Source: Lucent Technologies, USA)

programs without the continuing development and application of solar cells. The knowledge gained in these programs was the basis of the research and development of photovoltaic devices for terrestrial applications.

Over the last decades, the number of solar cells produced as energy source for terrestrial and space applications has constantly increased. The consolidated world production of photovoltaic cells summed up to only 500 kW total electric power in 1977, but it increased to about 9.3 MW in 1982 and reached 1146 MW in 2004 [4]. It is forecast that this exponential growth of the solar-cell market will continue for the coming decades, taking into account a further strongly increasing demand for electrical power.

The efficiencies of commercial photovoltaic modules are constantly increasing, leading to a decreased cost-per-watt ratio. Also, while solar cells in the 1980s and 1990s were uneconomical due to their much longer energy pay-back time (i.e., the time needed for a module to deliver the same amount of energy as was required for its fabrication and installation), the solar modules of today show much shorter energy pay-back times of down to two or three years [5] with an expected life time of up to 25-30 years. For thin-film solar cells, the energy pay-back time is expected to even drop to less than one year within the next decade [5].

In conclusion, photovoltaic cells exhibit an energy source with continuously improving technology and thus perpetually growing importance. The energy these cells provide may be obtained locally and present independence from any external

energy supplier.

1.2 Cu(In,Ga)Se_2 thin-film solar cells

Solar cells available today are based on various materials and are produced by a number of techniques. Prominent examples are cells based on crystalline Si or III-V semiconductors, those produced by thin-film techniques, or those belonging to the group of dye-sensitized or organic solar cells. All of these different types of photovoltaic cells have different advantages and disadvantages, which will not be addressed here. In the present thesis, $Cu(In, Ga)Se_2$ (CIGS) thin-film solar cells have been investigated. Of all thin-film solar cells, CIGS devices have yielded highest efficiencies to date of up to 19.5% [6]. These cells consist of a stack of thin-film layers deposited on a, e.g., soda-lime glass (SLG) substrate. The *p*-*n* junction of the solar cell is formed by the *p*-type CIGS absorber and an *n*-type semiconductor window layer, e.g., CdS, In_2S_3 or ZnSe. To facilitate the charge transport from the *p*-*n* junction, a back (e.g., Mo) and a front contact layer (e.g., a i-ZnO/ZnO:Al bilayer) are applied. Normally, a Ni-Al grid is deposited on top of the i-ZnO/ZnO:Al window layer to increase the charge collection. This CIGS solar cell in the so-called "substrate configuration" is illuminated from the ZnO side, thus, the ZnO is also referred to as "window layer". A bright-field transmission electron micrograph of the SLG/Mo/CIGS/In_2S_3/i-ZnO/ZnO:Al cross-section is shown in Fig. 1.2.

$Cu(In, Ga)Se_2$ is an alloy of $CuInSe_2$ (CIS) and $CuGaSe_2$(CGS). In the beginning of the 1970s, research and development had been concentrated on thin-film solar cells based on CIS absorbers [7, 8, 9]. This absorber material has been attractive owing to its very high absorption coefficients of about 10^5 cm^{-1} over most of the visible solar spectrum [10]; thus, absorber thicknesses of about 2 μm are sufficient, which offers a low-cost perspective for industrial production (in contrast, crystalline Si solar cells need by a 100 times thicker absorbers owing to the lower absorption coefficient of Si).

However, the optimal absorber band-gap energy for terrestrial solar energy conversion using single junction solar cells had been established to be in the range of 1.3 to 1.5 eV [11, 12, 13], substantially greater than the 1.04 eV value of $CuInSe_2$ [14]. Hence, considerable effort has been invested in the band-gap engineering of CIS by alloying it with CGS [15], which has a band-gap energy of 1.69 eV [16]. Moreover, in current production of high-efficiency CIGS solar cells, the CIGS absorber does not show a homogeneous composition, but reveals a gradient in the Ga content as a function of depth in the CIGS films. The Ga content (the ratio

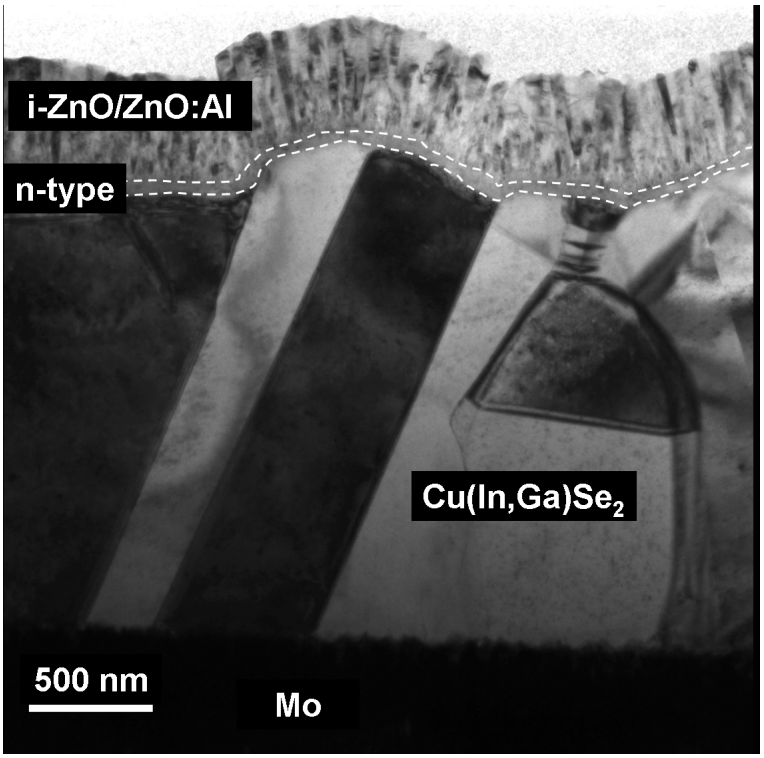

Figure 1.2: Bright-field transmission electron micrograph of the SLG/Mo/CIGS/In_2S_3/i-ZnO/ZnO:Al cross-section

Ga/(Ga+In) ranges approximately from 20 to 35 at.% for all samples studied in the present work) increases towards the back of the film (for CIGS films grown by the 3-stage process, introduced in section 2.1, there is enhanced Ga concentration also at the surface of the CIGS layer). As the band gap increases with higher Ga contents, the gradient in Ga corresponds to a grading of the band gap [17]. It was shown by Dullweber et al. [18] that the open-circuit voltage increase - compared with non-graded CIS cells (band-gap energy 1.04 eV) - is directly related to the increased band-gap energy at the back surface, probably owing to a reduced back contact recombination (a possible reason for this increase of the open-circuit voltage may also be an enhanced Cu concentration in the near-surface region of the CIGS layer, which leads to an enhanced built-in potential).

According to available quasi-binary phase diagrams of the Cu_2Se-In_2Se_3 system (e.g., [19, 20]), Cu concentrations of about 22-24 at.% are necessary in order to form $CuInSe_2$ (and $CuGaSe_2$), i.e., the CIGS alloy is non-stoichiometric. Its *p*-type semiconductivity results from Cu vacancies. With Cu concentrations ranging between 22 and 24 at.% and for growth temperatures between 450 and 580 °C,

the crystal structure of CIS and CGS is normally that of tetragonal chalcopyrite ($CuFeS_2$), which is based on the cubic zincblende structure (Fig. 1.3). The $CuInSe_2$ and $CuGaSe_2$ phases with chalcopyrite crystal structure are referred to as

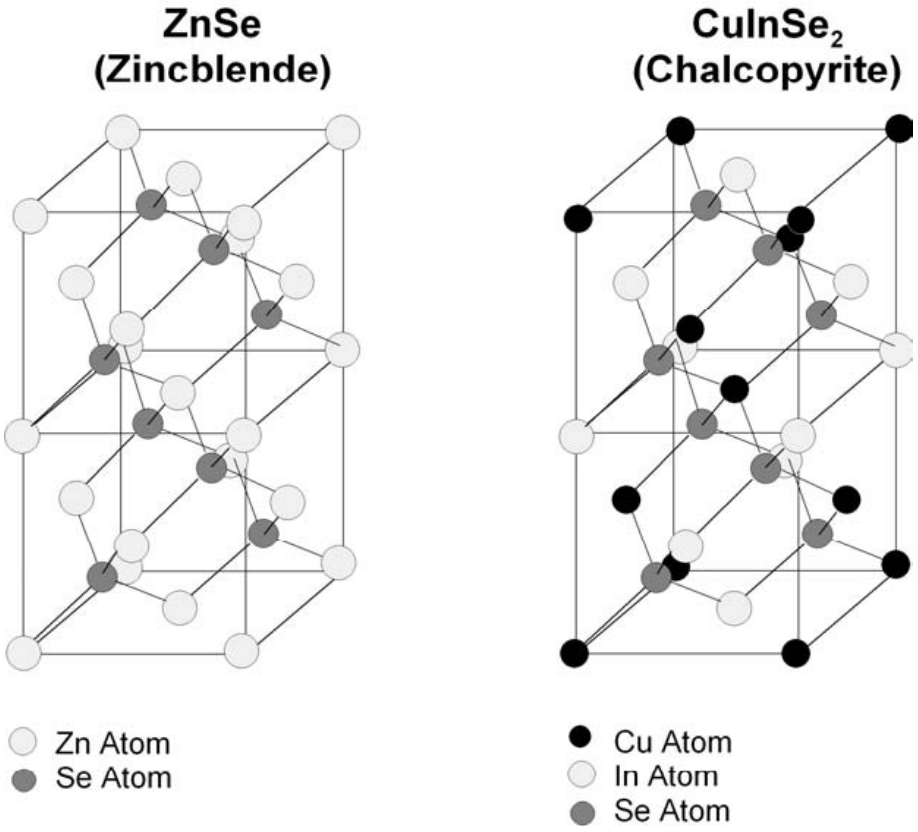

Figure 1.3: Unit cells of ZnSe (zincblende structure) and $CuInSe_2$ (chalcopyrite). Partial substitution of In for Ga in the $CuInSe_2$ unit cell leads to the structure of $Cu(In, Ga)Se_2$ (from [21]).

α-CIS and α-CGS. In general, $CuInSe_2$ films may contain impurities of $CuIn_3Se_5$ or $CuIn_5Se_8$ for Cu-poor layers and impurities of Cu_xSe ($x<2$) for Cu-rich layers.

A particular feature of this type of solar cells is their excellent stability under terrestrial and space conditions, as confirmed by proton and electron irradiation [22, 23, 24]. Especially for space applications, a weight reduction of the solar modules is desired. Therefore, CIGS solar cells are also produced on flexible substrates such as polymer or metal foils. The most efficient CIGS solar cell on polyimide, η=14.1% [25], has to date been produced in the Thin-Film Physics Group at ETH Zurich.

A broader overview of CIS and CIGS solar cells can be found in various review articles [26, 27, 28, 29].

1.3 Buffer layers in Cu(In,Ga)Se_2 thin-film solar cells

CIGS thin-film solar cells may be formed by combining the p-type CIGS absorber with a wide-band, n-type, semiconducting window layer (the cell is illuminated from the window side). First CIS cells were produced with a CdS window layer of several micrometers thickness (e.g., [9]). Since CdS has a band-gap energy of only 2.4-2.5 eV [30] and thus absorbs a large part of the solar spectrum (all photons with energies larger than 2.4-2.5 eV), CdS had soon after been replaced by a $Cd_{1-x}Zn_xS$ alloy (e.g., [15]). By adjusting the value x, it was possible to vary the band-gap energy from 2.5 eV to 3.7 eV (the band-gap energy of ZnS, [31]). Eventually, the CdS window has been reduced to a 50 nm thin buffer layer between CIS (in order to minimize the absorption) and a transparent conducting ZnO window layer ([32, 33]). ZnO has a band-gap energy of about 3.4-3.5 eV [34], thus reducing the absorption above the solar spectrum to a minimum. In current high-efficiency CIGS solar cells, the ZnO window consists of a i-ZnO/ZnO:Al bilayer. The doping of ZnO by Al leads to a very high n-doping (10^{20} cm^{-3}). It is not yet clear what the role of the i-ZnO layer is; e.g., it may help to reduce the Al diffusion into CdS and CIGS and act as an adjustable local series resistance [35].
The term "buffer layer" refers to the role of this layer as adjusting element between absorber and window layer; this adjustment can be divided into:

- electronic adjustments, i.e., band alignments of conduction and valence bands
- structural adjustments, i.e., lattice matching
- chemical adjustments, i.e., reducing or enhancing interdiffusion processes

Also, the buffer layer helps to protect the CIGS surface from ion damage during the i-ZnO/ZnO:Al sputtering. Out of these items, the electronic adjustments are most important, since they are responsible for an optimal junction formation between the p-type and the n-type semiconductors. There are several reports on the importance of band alignments in CIGS solar cells; e.g., Minemoto et al. [36] showed that adjusting the conduction band offset between window and CIGS layers by an appropriate choice of the window layer is essential to decrease the majority carrier recombination via the window/CIGS interface. A typical equilibrium energy-band diagram of a ZnO:Al/i-ZnO/CdS/CIGS/Mo stack is shown in Fig. 1.4, indicating the positions of the conduction band, the valence-band and the Fermi energy for

each layer. An analysis of this equilibrium energy-band diagram along with a review of the understanding of electronic properties of CIGS solar cells can be found in Ref. [37].

CIS and CIGS solar cells have yielded highest efficiencies with CdS buffer layers deposited by chemical bath deposition (CBD). Omitting the buffer layer always resulted in lower efficiencies (e.g., [39]). Also, as-grown CIGS cells with CdS

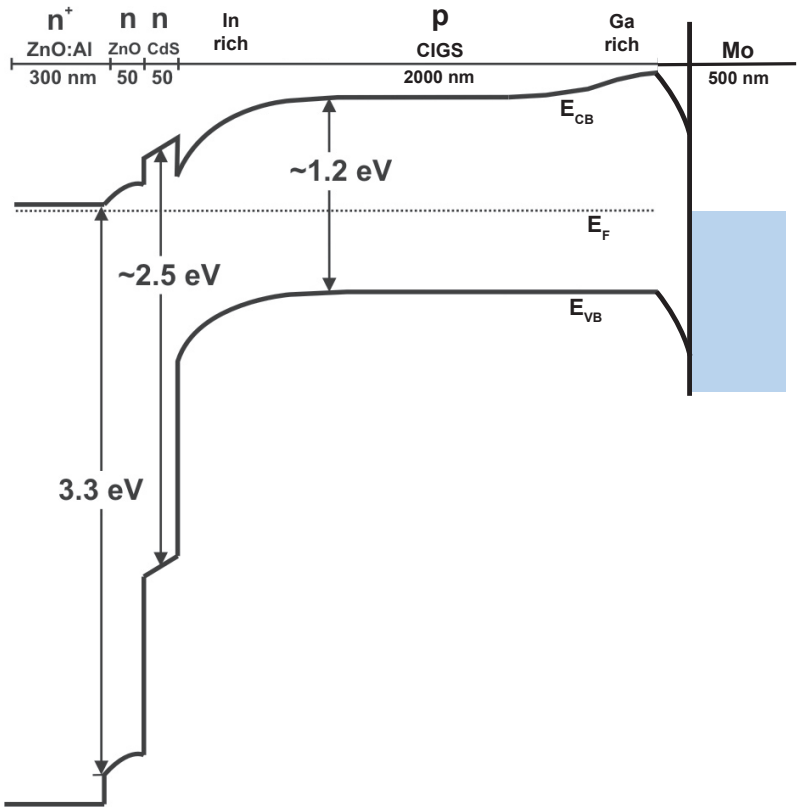

Figure 1.4: Typical equilibrium energy-band diagram of a ZnO:Al/i-ZnO/CdS/CIGS/Mo stack. E_{CB} is the conduction-band, E_{VB} the valence-band, and E_{F} the Fermi energy (based on Ref. [38]).

buffers deposited by physical vapor deposition (PVD) have always shown significantly lower efficiencies than cells with CBD-CdS buffers [40, 41]. Obviously, it is not the material CdS alone which leads to highest efficiencies. There are several models proposed to explain the influence of the chemical bath on the p-n junction

formation. All of these models deal with possible surface modifications by the ingredients of the chemical bath and the resulting structural, chemical and electronic changes at the CBD-CdS/CIGS interface. The role of the CBD-CdS buffer in the *p*-*n* junction formation will be treated in chapter 4.

Apart from CdS, alternative buffer-layer materials have also currently been investigated. Even though highest efficiencies have been achieved using CBD-CdS, there are several reasons for a desired substitution of CdS as buffer layer material and CBD as deposition method:

- the relatively small band-gap energy of 2.4-2.5 eV for CdS, i.e., the undesired absorption of high-energy photons in the buffer layer
- environmental aspects using a Cd (i.e., heavy metal) compound in an electronic device and expected market cautions
- the CBD process is not compatible with the in-line vacuum deposition of the CIGS absorber and the transparent conducting oxide front contact layers (ZnO:Al/i-ZnO)
- CBD solution disposal and waste recycling could be a matter of concern in industrial manufacturing

It has to be pointed out that regardless of toxicity, compatibility or waste aspects, manufacturers of CIGS solar cells still preferably apply CBD-CdS buffers - simply because these buffers result in highest efficiencies.
Out of numerous alternative materials, especially Zn- and In-based buffers deposited by various techniques have yielded promising results in CIGS solar cells. In the present thesis, In_2S_3 buffers and their interfaces to CIGS have been studied. These buffer layers may be deposited by atomic-layer deposition (ALD), co-evaporation from the elements, compound-evaporation from In_2S_3 powder and sputtering. These techniques will be introduced in section 2.2.

1.4 Back-contact materials for Cu(In,Ga)Se_2 thin-film solar cells

Various metal contacts to *p*-type CIS were examined by Matson et al. [42] concluding that only Au and Ni ensure an ohmic contact. Orgassa et al. [43] fabricated CIGS solar cells with different back-contact materials and found that W and Mo contacts provide the best CIGS/back contact interface passivation. Nowadays, Mo grown by sputtering or electron-beam evaporation is the most commonly used back

contact for CIGS solar cells.
Early results by Russell et al. [44] suggested that Mo back contacts for CIS form a Schottky-type barrier. But recently, Shafarman et al. [45] who analyzed the Mo/CIS interface separately from the cell, showed the contact to be ohmic, probably because of the formation of a $MoSe_2$ layer between Mo and CIS [46]. Its influence on the ohmic contact behavior at the CIGS/Mo interface makes the $MoSe_2$ formation an important issue. $MoSe_2$ may be considered a buffer layer between Mo and CIS (or CIGS) which leads to a better energy-band alignment and thus to an improved electrical contact [47].
$MoSe_2$ is regularly found in a hexagonal phase (Fig. 1.5), which consists of Se-Mo-Se sheaths oriented perpendicular to the *c*-axis. From this anisotropic crystal

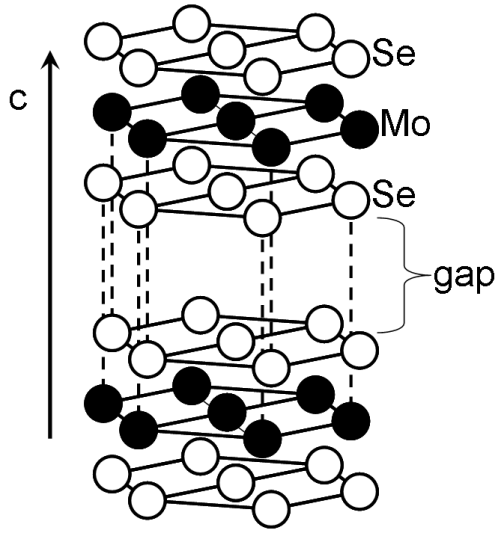

Figure 1.5: Anisotropic crystal structure of hexagonal 2H-$MoSe_2$. It consists of Se-Mo-Se sheaths which are separated from each other by a gap. The *c*-axis of this crystal structure is perpendicular to the Se-Mo-Se sheaths.

structure, possible applications arise for $MoSe_2$, e.g., as lubricant [48]. Mechanical and electrical properties of the 2H-$MoSe_2$ crystal structure will be further addressed in detail in chapter 7.

Even if widely used as back-contact material in CIGS solar cells, Mo easily oxidizes [49], and the oxide is water-soluble. This leads to a long-term degradation of the solar cell performance. Thus, there is a need to study other back-contact concepts. E.g., a very thin, intentionally grown layer of $MoSe_2$ may be applied to act as a buffer layer on, e.g., a transparent conducting oxide (TCO) back contact, prior to the CIGS deposition, so that a tunnel junction is formed, which facilitates

a quasi-ohmic contact to the CIGS absorber. Recently, it has been reported (e.g., [50]) that solar cells on a TCO back contact with an intentionally grown $MoSe_2$ intermediate layer show a better photovoltaic performance than without the $MoSe_2$ intermediate layer.

A profound understanding of the reaction kinetics of the $MoSe_2$ formation is vital for the development of low resistance electrical back contacts for high efficiency CIGS solar cells, since the thickness and the crystallographic orientation of $MoSe_2$ determine the adhesion and electrical properties of the CIGS-Mo interface. Thus, in chapter 7 of the present thesis, an overview on the formation of $MoSe_2$ and results from characterization of $MoSe_2$ layers grown on Mo substrates under variation of divers parameters will be given.

1.5 The role of Na in Cu(In,Ga)Se_2 thin-film solar cells

In ZnO:Al/i-ZnO/CdS/CIGS/Mo solar cells deposited on soda-lime glass (SLG), Na diffuses from the SLG into the Mo and CIGS layers during the absorber growth at elevated temperatures. The diffusion of Na through the Mo back contact appears to be primarily determined by the microstructure of the Mo layer and Mo oxide phases, present at grain boundaries [51, 52]. Hedström et al. [53] were the first to find Na diffusing from the SLG substrate into CIS, causing improved solar-cell efficiency. These authors studied the influence of "contaminants" on the CIS growth and concluded that Na may have a considerable impact on the preferred orientation of CIS. Although thereafter numerous groups have investigated the effects of Na on CIGS solar cells, no comprehensive interpretation of the structural and electronic effects of Na has been achieved up to now.

The most obvious electronic effect of Na incorporation into CIGS films is a decrease in resistivity by as much as two orders of magnitude (e.g., [54]). Contreras et al. [55] proposed a model where Cu vacancies in the CIGS lattice are preferably occupied by Na. This process may reduce the number of In_{Cu} defect states, thus, the hole concentration in the absorber may be increased. According to Rudmann [56], Na-induced cell efficiency improvements are dominated by electronic effects which may induce structural effects. Since the solubility of Na in CIGS single crystals is very low, Na resides in CIGS thin films at grain boundaries. This author assumes that Na improves the quality of CIGS films by passivating grain boundaries and surfaces.

While the effects of Na on the Mo and CIGS growth have been investigated extensively, results about the influence of Na on the buffer-layer growth are scarce. Early results by Henry et al. [57] suggest that Na acts as shallow acceptor in CdS crystals. Studying CBD-CdS/CIGS interfaces by means of x-ray emission spectrometry and photoelectron spectrometry, Heske et al. [58] found that Na is incorporated and localized at these interfaces. According to these authors, Na may be responsible for an altered electronic structure of the heterojunction. For co-evaporated In_2S_3 buffers, Barreau et al. [59] showed that Na leads to a significant increase of the band-gap energy and also to an increase in the conductivity of these layers. Sterner et al. [60] reported that the conduction band offset at the ALD-In_2S_3/CIGS interface is larger for Na-free devices, indicating an unfavorable band alignment at the heterojunction.

The issue of Na will be addressed concerning the effects of Na on ALD-In_2S_3/CIGS interfaces, and on the growth of $MoSe_2$ in chapters 5 and 7.

1.6 Studies of interfaces in Cu(In,Ga)Se_2 thin-film solar cells

The complete knowledge about the processes taking place at the interfaces of CIGS thin-film solar cells would allow any electrical parameter of these cells to be predicted, and thus would help to design solar cells of enhanced performance. E.g., recombination of generated charges at the p-n junction reduce the number of the collected charges, leading to a reduced current density. However, it is rather difficult to access the complete knowledge about these processes.

Since the p-n heterojunction in CIGS thin-film solar cells is formed at the interface between the p-type CIGS absorber and the n-type buffer layer (or at least close to this interface), the buffer/CIGS interface is also most important in these cells. The present thesis thus concentrates mainly on the study of CIGS/buffer interfaces in order to reveal their structural and chemical properties, to learn more about interdiffusion properties and the effects on the growth of the according layers.

In general, studies of interfaces in CIGS thin-film solar cells may be divided into electronic, structural and chemical characterization. Since there is no technique which is able to reveal all occurring processes in the solar cells on its own, several methods have to be combined in order to study these interfaces and interpret the phenomena found. Among those techniques applied to reveal electronic properties of interfaces in CIGS thin-film solar cells are scanning tunnelling (STM, e.g., [61])

and scanning Kelvin probe microscopy (SKPM, e.g., [62]), ultraviolet (UPS) and x-ray photoelectron spectrometry (XPS) (e.g., [63]), photoluminescence (PL, e.g., [64]), cathodoluminescence (CL) and electron beam induced current (EBIC) measurements (e.g., [65]). Capacitance-voltage or other capacitance-related techniques contribute as well to a better insight into electronic features at interfaces such as the effect of defect states (e.g., [66]).

In addition to these electrical characterization methods, several techniques for structural (e.g., x-ray diffraction) and chemical characterization (e.g., Auger electron, AES, x-ray photoelectron, XPS, or secondary ion-mass spectrometry, SIMS) may be applied. In order to reveal both, structural and chemical properties, of interfaces in CIGS thin-film solar cells within one machine, transmission electron microscopy (TEM) and its related techniques provide powerful tools. The possibility to image areas of interest down to the angstrom scale and to perform chemical measurements with a similarly high accuracy provides the means for a careful investigation of all kinds of structural and chemical features. Therefore, TEM and its related techniques are also most important characterization methods applied within the frame of the present thesis. All these techniques will be introduced in chapter 3.

1.7 Objectives and outline of the present thesis

Although the technical development of CIGS thin-film solar cells has already reached a level sufficiently mature to enter into pilot and mass production of these cells (as demonstrated by, e.g., the companies Würth Solar, Marbach, Germany, and Shell Solar, Munich, Germany), many questions remain unsolved, various phenomena can not be explained, and even more questions and phenomena arise from the still further development of CIGS solar cells. Unfortunately, the CIGS solar-cell system is very complex and therefore difficult to study. Altogether, there are not less than 10 elements involved, which are not always restricted to their regular positions in the layers but may interdiffuse across the interfaces and along grain boundaries. It is also inconvenient that many of the alloys formed during the deposition of the layers show an inhomogeneous composition and a considerable density of impurities.

During the course of the present thesis, study the structural and chemical properties of buffer layers grown by various techniques were characterized, and also their interfaces to CIGS were analyzed, mainly by means of TEM and its related characterization techniques, in order to give answers to at least some of the open questions arisen from their research and development. It was possible to give

reasons for the behavior of the solar-cell performance under variation of divers parameters during the buffer-layer growth, e.g., the substrate temperature and the presence of Na. Cells with CdS buffer layers grown by CBD and by PVD as well as cells with In_xS_y buffer layers grown by ALD, by co-evaporation from the elements, by compound evaporation from In_2S_3 powder and by sputtering were studied. In addition, the possibility to apply $MoSe_2$ as a buffer layer between CIGS and a TCO back contact was exploited, and various parameters of the $MoSe_2$ growth were varied in order to optimize the $MoSe_2$ properties for a tunnelling quasi-ohmic contact.

The open questions mentioned above are summarized in the following:

- Why do CIGS solar cells with CBD-CdS buffers show an enhanced solar-cell performance as compared with PVD-CdS-buffered cells?

- Why is the optimum substrate temperature during the ALD-In_2S_3 deposition about 210-220 °C, and why do ALD-In_2S_3 cells with Na show a better solar-cell performance than those without Na?

- Why is the optimum substrate temperature during the sputtering of In_xS_y buffers about 210-220 °C, and what have the In_xS_y/CIGS interfaces of these cells in common with those of the ALD-In_2S_3 samples?

- What is the effect of air-annealing of the complete CIGS solar-cell with PVD-In_xS_y buffer?

- Why do CIGS solar cells with In_2S_3 or more generally In_xS_y buffers always show very low efficiencies when a substrate temperature above about 250 °C is chosen during the In_xS_y deposition?

- What are the optimum parameters during the $MoSe_2$ formation by selenization of Mo substrates in order to achieve $MoSe_2$ buffer layers on a TCO contact which may be able to replace Mo as back-contact material?

In order to provide answers to these questions, the present thesis is structured in the following way. In chapter 2, the production procedures of layers in CIGS solar cells are described, followed by an introduction of all characterization methods applied within the frame of the present thesis in chapter 3. Chapter 4 deals with the structural and chemical differences of CIGS solar cells containing CBD-CdS and PVD-CdS buffer layers. Structural and chemical features in cells with In_2S_3 and In_xS_y buffers will be addressed in chapter 5. These cells show an interfacial phase formation between the buffer layer and CIGS for substrate temperatures exceeding about 250 °C. This phenomenon will be discussed in chapter 6 for various In_2S_3 deposition techniques. The growth of $MoSe_2$ as buffer layer between CIGS and the

Mo back contact and its properties under various growth conditions will be covered in chapter 7. Finally, concluding remarks and an outlook are given in chapter 8.

Chapter 2

Production of $Cu(In,Ga)Se_2$ solar cells

A micrograph of the cross-section of a typical CIGS thin-film solar cell is shown in Fig. 1.2. Such a solar cell consists of a Mo/CIGS/buffer/i-ZnO/ZnO:Al stack grown on a substrate. This is mostly soda-lime glass (SLG), but also flexible substrates such as polymer or metal foils are applied. In the following, a short description of the deposition techniques for each of these layers is given. Only those techniques are mentioned which were applied to produce the samples studied in the frame of the present thesis.

2.1 Deposition of back contact, absorber and window layers

Mo back contact and Na barriers

Mo is commonly deposited by dc magnetron sputtering or by electron-beam evaporation. When produced by sputtering, the layer properties are varied primarily by changing the sputter power, resulting in different kinetic energies of the sputtered Mo atoms arriving at the substrate. For a high sputter power (e.g., 2 kW), the adhesion of the Mo film to the SLG substrate is enhanced compared with low-power (e.g., 0.3 kW) films. However, continuous sputtering at high sputter power may cause delamination of undesired flakes from the deposition chamber walls [56], and also Mo films at high power exhibit a larger resistivity compared with low-power films. Therefore, commonly, a Mo bilayer is applied as back contact. First, a thinner layer is deposited at high sputter power (e.g., 100 nm at 2 kW), then a thicker layer is deposited at low sputter power (e.g., 850 nm at 0.3 kW).

Within the frame of the present thesis, samples with Na diffusing from the SLG and Na-free samples have been investigated. In order to prevent Na diffusion from the SLG substrate, Al_2O_3 layers were deposited between the SLG and the Mo layers. Al_2O_3 was shown to impede Na diffusion from the SLG substrate efficiently [67]. Further materials suitable to reduce the Na diffusion from the SLG have been reported by Palm et al. [68].

CIGS absorber

All of the CIGS thin-films for the solar cells studied within the frame of the present thesis were produced by co-evaporation from the elements Cu, In, Ga and Se, either using the so-called *single-layer* or the so-called *3-stage process* [17]. The ratio Ga/(Ga+In) ranges approximately from 20 to 35 at.% for all samples studied in the present work.
The *single-layer process* is the simplest technique to produce CIGS layers, since the elements are evaporated simultaneously at constant evaporation rates and substrate temperatures. The resulting CIGS films are always Cu poor. Such a process was applied by the Würth Solar GmbH & Co. KG, Marbach, Germany, which provided the CIGS/Mo/SLG and the CIGS/Mo/Al_2O_3/SLG substrates for the studies of the ALD-In_2S_3/CIGS and sputtered In_xS_y/CIGS interfaces presented in chapter 5. Details on this CIGS deposition process can be found in Ref. [69].

The *3-stage process* consists of the following production steps:

- deposition of an $(In,Ga)_2Se_3$ precursor layer at low temperature (250-400 °C)

- co-deposition of Cu and Se at about 550 °C until the overall composition is Cu-rich

- co-evaporation of a small amount of In,Ga and Se until the layer shows the Cu deficiency required

Naturally, the control of the parameter for the *3-stage process* is much more complicated than for the *single-layer process*. However, CIGS produced by the *3-stage process* exhibits enhanced structural and electrical properties. For high-efficiency solar cells, the [In]/[Ga] ratio is additionally increased during the *3-stage process* in order to achieve a Ga gradient, i.e., a band-gap grading as a function of depth in the CIGS films, as mentioned in section 1.2. A *3-stage process* was applied by the Institut für Physikalische Elektronik (IPE), University of Stuttgart, Germany, and by the Thin-Film Physics Group, ETH Zürich, Switzerland, in order to produce samples studied in the frame of the present thesis.

i-ZnO/ZnO:Al window and Ni-Al grid

The most common window applied in CIGS solar cells consists of two layers. The first layer, a thin i-ZnO film, is deposited by rf magnetron sputtering and has normally a thickness of about 50 nm. The second layer is the actual front contact and consists of ZnO:Al, also deposited by rf magnetron sputtering. Typical ZnO:Al thicknesses are 300-500 nm.
The current collection by the window layer is commonly supported by a Ni-Al metal grid deposited on the front contact. Ni is applied to reduce the formation of a resistive Al_2O_3 barrier. The Ni and Al layers are deposited by electron-beam evaporation with thicknesses of about 50 nm and 1 µm. Although the application of a grid is beneficial for the solar-cell performance, it contributes also to a reduction of the active cell area.

2.2 Deposition methods of buffer layers

All buffer layers studied for the present thesis were produced by various colleagues from the Zentrum für Solarenergie- und Wasserstoff-Forschung (ZSW), Stuttgart, Germany, the Institut für Physikalische Elektronik (IPE), University of Stuttgart, Germany, and the Thin-Film Physics Group, Laboratory for Solid State Physics, ETH Zürich, Switzerland. If not noted otherwise, buffer layers were deposited at the Thin-Film Physics Group, ETH Zürich.

It is important to point out that all substrate temperatures given in the present thesis were measured in different laboratories and thus under different conditions. In general, errors of about 10-20 K may be assumed, and caution is advised when comparing temperature values measured by different laboratories.

2.2.1 CdS by chemical bath deposition

For the deposition of CdS by chemical bath deposition (CBD), the samples were immersed into an aqueous solution of Cd acetate ($Cd(C_2H_3O_2)_2)_4$), thiourea ($SC(NH_2)_2$) and ammonia (NH_3) at a temperature of about 70 °C for 15 min. The overall reaction can be described as [70]

$$Cd(NH_3)_4^{2+} + SC(NH_2)_2 + 2OH^- \rightarrow CdS + CN_2H_2 + 4NH_3 + 2H_2O.$$

Typical CBD-CdS layer thicknesses are about 30-60 nm.

2.2.2 CdS by evaporation of CdS powder

The deposition of CdS buffer layers grown by physical vapor deposition (PVD) was performed from a crucible containing CdS powder in a high-vacuum thermal evaporation system at 10^{-8} mbar and at a substrate temperature of 50 °C for 30 min. The resulting buffer layers showed thicknesses of about 50-70 mn.

2.2.3 In_2S_3 by atomic layer deposition

In_2S_3 buffer layers by atomic layer deposition (ALD) were deposited at the ZSW, Stuttgart, Germany, at temperatures ranging from 140 °C to 240 °C. Reactants in this process were indium acetylacetonate ($In(CH_3COCHCOCH_3)_3$), which was evaporated from a glass crucible at about 130 °C, and hydrogen sulfide (H_2S) gas. These precursors of In and S were alternatingly introduced into the reaction chamber and distributed over the substrate surface, while nitrogen (N_2) was used as a carrier and purging gas. The deposition duration was between 70 and 130 min, depending on the substrate temperature. For all samples, the final In_xS_y layer thickness was determined to be approximately 30-40 nm.

2.2.4 In_xS_y by physical vapor deposition

Co-evaporation, compound-evaporation, and sputtering are all physical vapor deposition (PVD) methods. In-S buffer layers deposited by these techniques are not merely In_2S_3, but consist of different other In-S compounds [71] (e.g., InS and In_6S_7), owing to a sulfur loss during the evaporation or sputtering process. Thus, in the present thesis, the notation "In_xS_y" is used for these In-S buffer layers.

In_xS_y by co-evaporation of In and S powders

Elemental In and S were evaporated at constant rates in an ultra-high-vacuum system at the IPE, University of Stuttgart, Germany. Although a high-temperature S cracker cell was used, the S vapor mainly contained S molecules. Normally, excess S was provided by switching-off the In-source before the S source. The buffer-layer deposition temperature was 280 °C and the buffer layer thickness about 70 nm.

In_xS_y by evaporation of In_2S_3 powder

In_2S_3-powder was evaporated from a boron nitride crucible heated to about 725 °C, also at the IPE, University of Stuttgart, Germany. Since the melting point of In_2S_3 is 1050 °C, a sublimation process takes place [72]. Buffer-layer deposition

temperatures between 23 and 300 °C were chosen, and the buffer-layer thicknesses ranged from 30 to 90 nm.

In_xS_y by sputtering from In_2S_3 targets

Sputtered In_2S_3 layers were deposited at the ZSW, Stuttgart, Germany, in a von Ardenne CS 730S laboratory magnetron sputtering system with a base pressure of $2x10^{-7}$ mbar. In_2S_3 buffers were sputtered from a ceramic In_2S_3 (3N) target with a diameter of 200 mm and a target-to-substrate distance of 74 mm. The In_2S_3 layers were deposited at a rate of about 20 nm/min and at a power density of 1 W/cm^2 using Ar (5N) as sputter gas. The pressure during the sputtering process was kept at $1x10^{-2}$ mbar. The sputtering chamber provides three positions for the sample; a load-lock position for mounting and removing the sample, an annealing position where the sample is placed in front of a heater and the sputtering position. In the sputtering chamber, the substrates can be annealed in vacuum, before as well as after the sputtering process (pre-annealing and post-annealing). Best results have been achieved for pre-annealed samples [73]. Therefore, for all samples studied, the CIGS/Mo/SLG substrates were pre-annealed prior to the buffer layer deposition for 10 min, and the substrate temperature was measured during the sputtering process. Fig. 2.1 shows the substrate temperature as well as the according position of the sample in the sputtering chamber in dependence of the duration. The average substrate temperatures during the sputtering were 60, 230 and 340 °C, and after these values, the samples were termed.

2.2.5 $MoSe_2$ by the selenization of single-crystalline and polycrystalline Mo substrates

Polycrystalline Mo layers or Mo single crystals were selenized under various conditions. The parameters varied were:

- the selenization duration
- the substrate temperature during the selenization
- the Mo orientation using Mo single crystals
- the thickness of the NaF layer as Na source
- the background pressure in the selenization chamber
- the use or absence of N_2 as transport gas.

Polycrystalline Mo substrates were selenized for various durations ranging from 10 min to 3 h using the following methods:

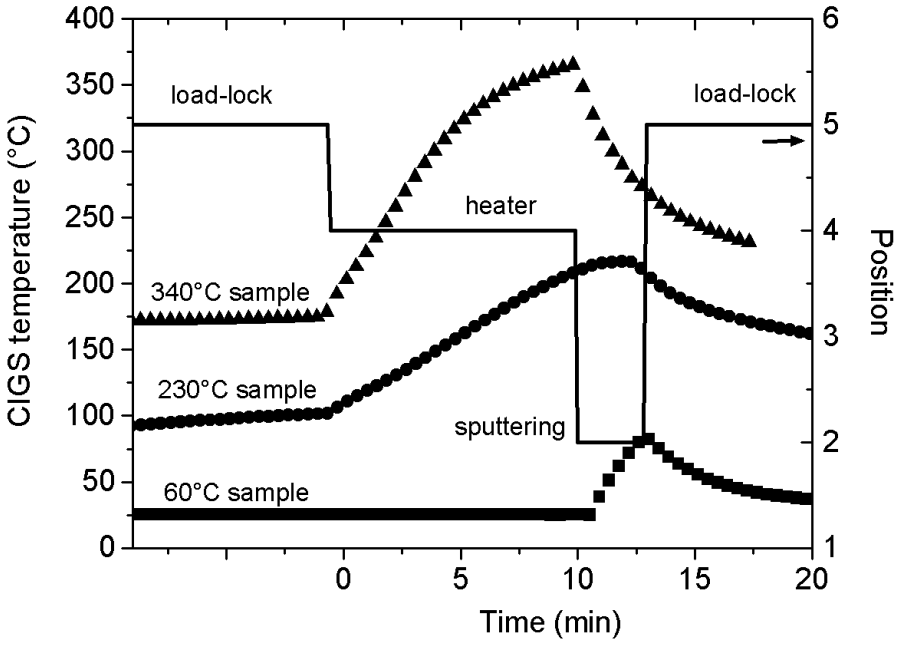

Figure 2.1: Substrate temperature and position of the sample in the sputtering chamber in dependence of the duration. The samples were termed after the average substrate temperatures during the sputtering, 60, 230 and 340 °C.

i. Selenization in a two-temperature zone quartz tubular reactor where the temperature of the Se source was 350-400 °C, and the Se vapor was transported on the substrate by a N_2 flux at a pressure of about 10 mbar.

ii. Selenization in a vacuum chamber at a pressure of about 10^{-7}-10^{-6} mbar and at Se source temperatures of 300-350 °C.

Mo layers of different thicknesses were deposited on Si(001) wafers by dc-magnetron sputtering at 3x10^{-3} mbar. The Na concentration in the samples was regulated by the deposition of NaF layers with different thicknesses (5, 10 and 15 nm) on the same Si wafer, prior to the Mo deposition, thermally evaporated from NaF crystals.
Additionally, in order to study the influence of the Mo orientation on the $MoSe_2$ growth, Mo single crystals oriented in [100], [110] and [111] were used as substrates. These single crystals were selenized at 580 °C for 2 h using method (i) in order to obtain $MoSe_2$ layers with thicknesses sufficiently large for the thickness and composition measurements.

Chapter 3

Methods of characterization

3.1 Transmission electron microscopy

A transmission electron microscope consists basically of an electron source (or electron gun), condenser lenses, an objective lens, magnification or projection lenses, and a viewing screen (Fig. 3.1). In principle, the illumination system of this microscope accelerates the electrons by a potential difference of typically 80-300 kV from the gun to a specimen giving either a broad (conventional transmission electron microscopy, TEM, mode) or a focussed beam (scanning TEM mode). Additionally, apertures in the condenser lenses are used to control the beam current and the convergence of the beam hitting the specimen. In the specimen, the electrons are scattered mainly by the electrical potential in the crystal lattice. The objective lens focuses the transmitted beam in the back-focal plane, and a projection image of the specimen is formed in the image plane. The electron-diffraction pattern is located in the back-focal plane of the objective lens. Depending on the desired application, either the projection of the specimen or the diffraction pattern may be magnified on the viewing screen (or on the CCD camera/photographic film) using an appropriate configuration of magnification lenses.

TEM is a very powerful tool to study structural and chemical properties of layers and interfaces in CIGS solar cells on the angstrom scale. However, it should always be considered that it is a two-dimensional technique applied to study three-dimensional systems. Thus, the interpretation of transmission electron micrographs and also of chemical studies is not at all straightforward and becomes the more complicated the higher the resolution is.

The most important step is not the work at the microscope, but the preparation of the specimen for TEM analyzes. Therefore, the preparation step will be

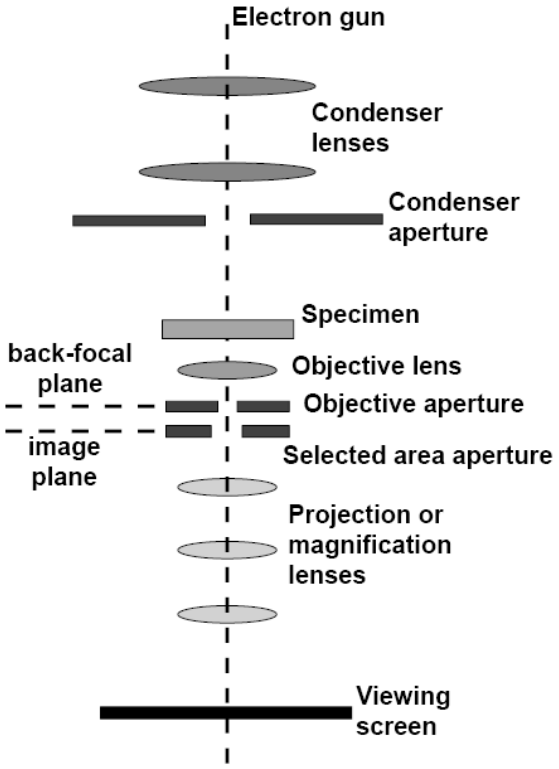

Figure 3.1: Typical set-up of a transmission electron microscope. The electron-diffraction pattern is generated in the back-focal plane of the microscope.

presented prior to the detailed description of modes and techniques available at the microscope. During the course of the present thesis, a PHILIPS CM 30 and an FEI TECNAI F30, both, operated at 300 kV, were used. An introduction to TEM and a detailed description of technical details, modes and techniques can be found in, e.g., [74].
During the course of the present thesis, only cross-section samples were prepared for TEM. This is because the main interest were the analyzes of structural and chemical properties of interfaces in CIGS solar cells.

3.1.1 Preparation of cross-section samples

Slices of 2 mm width and 4 - 6 mm length were cut out of the appropriate sample using a diamond wire saw. Slices of about 2 mm width and 4 - 6 mm length were cut out of a Si waver using a diamond scriber. Since these slices were finally embedded in tubes with an inner diameter of about 2.12 mm, their width had to be smaller than this value.

A slice of a Si wafer was then glued on top of a slice of the appropriate sample (with Si on top of the layers). The total stack thickness had to be smaller than the inner diameter of the metal tube (about 2.12 mm). To achieve the appropriate thickness, the substrate of the sample had to be ground at times. In general, the layers of interest were situated in the middle of the stack, so that they were in the center of the final TEM sample. For gluing, GATAN two-component epoxy glue was used. The standard ratio between hardener and resin was 1:10. At 120 °C, the hardening time was about 2 min.

After annealing the stack for a few minutes, it was ground so that it could easily be introduced into a tube composed of steel with an outer diameter of 3 mm and an inner diameter of about 2.12 mm. This was done to stabilize the TEM sample. The stack was embedded in the tube again with the GATAN two-component epoxy glue.

For cutting disks out of the tube, Al holders with an appropriate notch for the tubes were used. The tube was glued onto the Al holder with thermo-wax and cut using a diamond wire-saw. Polishing the disks down to a thickness of about 80 - 120 µm was performed using a lapping machine on wet grinding paper.

Using a GATAN 656 dimple-grinder, a spherical-segment-shaped deepening was

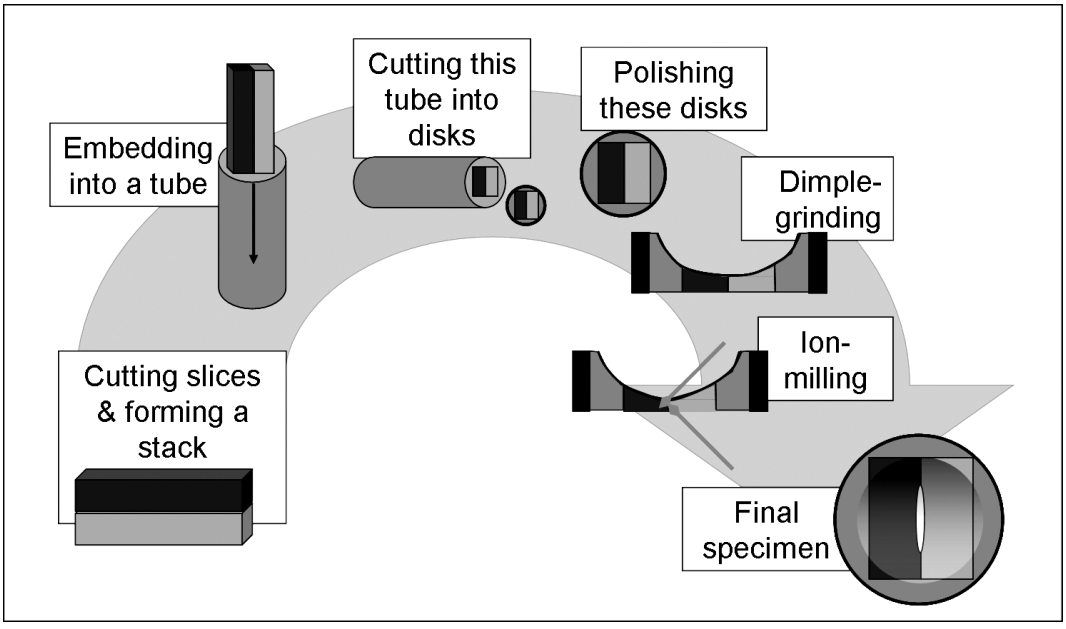

Figure 3.2: Summary of the preparation of cross-section samples from CIGS thin-film solar cells.

ground into the polished disk. The dimple-grinder consists of a specimen mount on which the glass cylinder with the polished disk was mounted, and a dimpling wheel. For the polishing procedure, a suspension of diamond particles in oil was used. The disks were dimple-ground from one side. The depth of the deepening was 70-75 µm. The remaining sample thickness in the middle of the deepening was about 25-30 µm. The counterweight was varied from 20 g in the beginning to 32 g towards the end the dimple-grinding procedure.

For the ion milling process, a GATAN 691 Precision Ion Polishing System (PIPS) was used. In this machine, two focussed Ar ion beams mill the dimple-ground sample in such a way that a hole results at the desired position. As ion-milling parameters, 3.5° (angle between ion beam and specimen surface) and 4 kV acceleration voltage were chosen; these parameters guarantee careful ion milling of the brittle CIGS solar cell. The beam modulation was activated, since it not only reduces the local temperature on the sample but also prevents preferential etching of the adhesive between the crystal platelets and also of layers with higher etching rates (these weaker materials are shaded).
In general, the final TEM specimens are contaminated by hydrocarbonates, and also degrade owing to oxidation or other chemical processes. The complete specimen-preparation process takes about 6 - 8 h and is summarized in Fig. 3.2.

3.1.2 Conventional transmission electron microscopy

In the conventional TEM (CTEM) mode, a broad, nearly parallel electron beam with a diameter of several micrometers hits the sample. Apertures in the back-focal plane and in the image plane may be applied to increase the contrast or select an area of interest.

Selected-area electron diffraction

Inserting an aperture into the image plane of the microscope (Fig. 3.1) results in the formation of a virtual aperture in the plane of the specimen. Those electrons falling outside the dimensions of this virtual aperture will be shielded from the imaging system. Selected-area electron diffraction (SAED) is a very useful tool to acquire an electron-diffraction pattern from a certain area of interest on the specimen.

Bright-field and dark-field TEM

These techniques are useful to increase the crystallographic contrast in polycrystalline samples such as CIGS solar cells. In order to apply bright-field (BF) or

dark-field (DF) imaging, an aperture is inserted into the back-focal plane of the microscope (objective aperture, Fig. 3.1), where the electron-diffraction pattern is formed.
In bright-field TEM, the objective aperture is placed around the zero reflection in the electron-diffraction pattern. The direct, non-diffracted beam stays on the optical axis, and diffracted electrons are shielded by the objective aperture de-

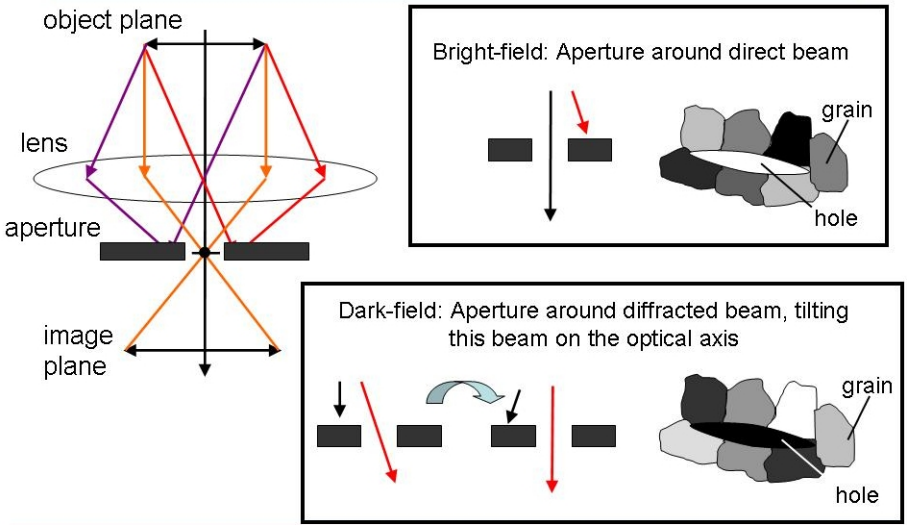

Figure 3.3: The principles of bright-field and dark-field TEM.

pending on its size. This generates a contrast in the image where grains which diffract electrons into regions shielded by the aperture appear dark, and the hole of the specimen appears bright.
In dark-field TEM, the objective aperture is placed around a certain reflection other than the zero reflection. In general, subsequently, the electron beam forming this reflection is tilted into the optical axis, i.e., the grains which diffract the corresponding electrons appear bright, and the hole appears dark. Instead of tilting the diffracted beam on the optical axis, annular dark-field detectors which are centered around the optical axis may as well be used to image a certain area of interest evaluating diffracted electrons.

High-resolution TEM

Unlike the CTEM techniques in low/medium magnification (up to about 200'000 times) that employ mass-thickness or the diffraction contrast, the high-resolution TEM (HR-TEM) technique uses the phase contrast to image lattice fringes and atomic structures. To be more precise, the HR-TEM images shown in the present

thesis are two-dimensional electron-beam interference patterns, which were generated by interference of electron waves diffracted at atomic planes of the specimen. The imaging of an atomic lattice requires its orientation in such a way that the atomic columns of this lattice are oriented parallel to the incident electron beam.

3.1.3 Analytical transmission electron microscopy using the scanning mode of the microscope

Differently from CTEM, in the scanning TEM (STEM) mode, a convergent electron beam or electron probe with few angstroms in diameter is used. This electron probe can be scanned over the surface of the specimen using a set of deflection coils. The STEM mode allows a careful probing of areas of interest on the specimen. Chemical analyses with a spatial resolution of about 1-2 nm are possible and have been performed during the course of the present thesis. However, it has to be considered that from such a small volume, the accuracy of the measurements is always limited due to poor statistics.
Electrons impinging on a specimen induce the emission of x-rays and also lose energy owing to an interaction with the electron shells of the atoms. These processes can be used to chemically analyze a certain area of interest. In addition, electron beams diffracted by atomic planes of the specimen may be detected by an annular detector in order to image the specimen.

Imaging using a high-angle annular dark-field detector

The high-angle annular dark-field (HAADF) detector is an annular detector consisting of an scintillator photomultiplier. In the FEI TECNAI F30, it is situated above the projection lenses (Fig. 3.1) and has been developed for two main aspects: single-electron sensitivity and high-angle collection. The acceptance angle is changed by varying the camera length. A general rule for the use of camera lengths is that a short camera length results in an increased chemical or Z-contrast (high collection angle, thus, elastically scattered electrons are preferably detected), while a large camera length improves the diffraction contrast in the image (small collection angle, thus, inelastically scattered electrons are preferably detected).

3.1.4 Energy-dispersive x-ray spectrometry

When electrons pass through a specimen, they interact with the electrons bound to atoms. An incident electron may collide with an inner-shell electron, which is then ejected from the atomic shell and may be detected as secondary electron (Fig. 3.4). The empty inner-shell state is subsequently occupied by another inner-shell electron from a higher energy level, and an x-ray quantum is emitted. Naturally,

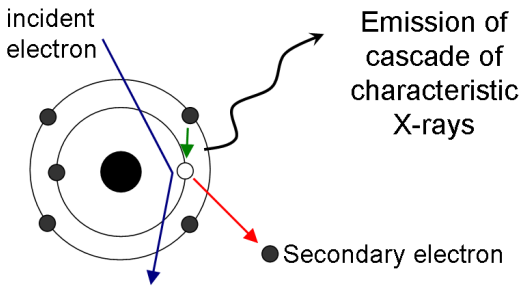

Figure 3.4: Principle of energy-dispersive x-ray spectrometry.

as a huge number of electrons impinge on the specimen per second and square nanometer, a whole cascade of x-rays is emitted from the specimen, which may be detected by an x-ray detector. The energy of a specific x-ray is equal to the energy difference between the two inner-core electron states corresponding to the transition, thus, it can be related to a specific element. Since apart from these characteristic x-rays, also, e.g., bremsstrahlung x-rays are generated, which are emitted preferably in forward direction (with respect to the incident beam), the energy-dispersive x-ray spectrometry (EDX) detector is always situated above the specimen in order to reduce the background signal in the EDX spectrum.

The x-ray detector used for the present thesis consists of a lithium-doped Si crystal with a Be window. X-rays with energies between 0 and 40 keV were detected with an accuracy of ± 10 eV. For the acquisition of EDX spectra on CIGS thin-film solar cells, the specimens were aligned in such a way in the specimen holder that the interfaces of the solar cell (i.e., the interface between the Si wafer and the substrate of the solar cell) were parallel to the α-tilting axis. Thus, an optimal orientation of the interfaces to the EDX detector could be guaranteed. Also, the specimen was not tilted in any way in order to have the interfaces aligned nearly parallel to the incident electron beam (edge-on).

Detailed description of the EDX measurements performed for the present thesis

Studying the chemical properties of layers and their interfaces in CIGS solar cells, EDX is the most important tool to reveal concentrations of elements in certain layers and interdiffusion processes across their interfaces. This is because most of the elements present in the cells are relatively heavy, and such elements are particularly well detected by EDX. Also, the possibility to chemically analyze an area of interest with a spatial resolution of 1-2 nm is especially useful in layers with an inhomogeneous composition and at interfaces where the concentration of

each element may change gradually.

One of the most interesting issues at interfaces in CIGS solar cells is how the composition changes across the interfaces. Therefore, line scans may be appropriate, i.e., EDX spectra are acquired on specific points along a line across the interfaces. However, during the course of the present thesis, it turned out that line scans are not sufficiently accurate to measure the elemental distribution across the interfaces of interest; these distributions showed fluctuations which were apparently in the same order of magnitude as the effects which should be revealed. Thus, elemental maps were acquired instead of bare line scans.

The principle of elemental mapping is shown in Fig. 3.5 considering as an example a CIGS/In_xS_y/ZnO interface. For each point of the grating shown, an EDX spectrum was acquired. Drift correction applied during the acquisition of an elemental map reduced the effects of specimen movements induced by, e.g., charging, to a minimum. For each spectrum acquired, the total number of counts under one

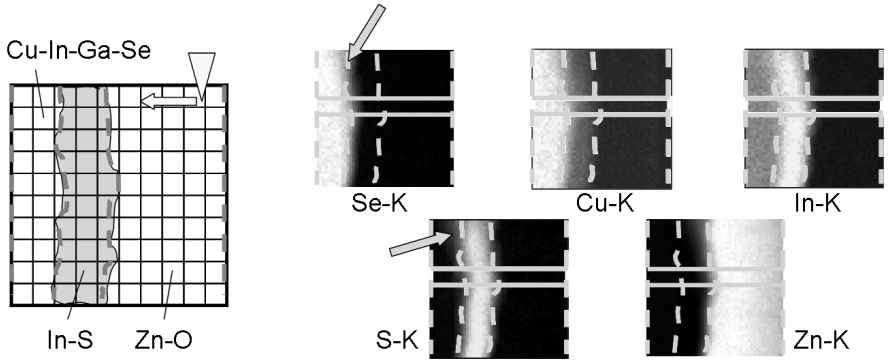

Figure 3.5: Principle of the elemental mapping of interfaces in CIGS solar cells. In the elemental maps, those areas are indicated by white frames from which four elemental distribution profiles were extracted. The arrows indicate positions where the S and Se signals appear diffuse.

or several peaks of x-ray signals emitted from a certain element (approximation by Gaussian curves) were calculated using the evaluation software of the FEI TECNAI F30 microscope, the *Tecnai Imaging & Analysis*, and displayed in the form of a map where each point has an intensity related to the number of counts extracted from the corresponding EDX spectrum. These elemental maps were saved in a bitmap-image format. It has to be pointed out that thereupon the number of counts can not be deduced anymore from the intensity; however, for a qualitative measurement of elemental distributions, this is also not necessary.

From these elemental maps, elemental distribution profiles were extracted using the *DigitalMicrograph* [75] software. The striking difference in accuracy between linear distribution profiles extracted from one line (i.e., a line scan) and profiles which are generated by averaging four elemental distribution profiles is apparent from Fig. 3.6. In this case, these four profiles were extracted from the white frames in the elemental maps shown in Fig. 3.5, indicated by arrows. All elemental distribution profiles shown in the present thesis were obtained by averaging four profiles.

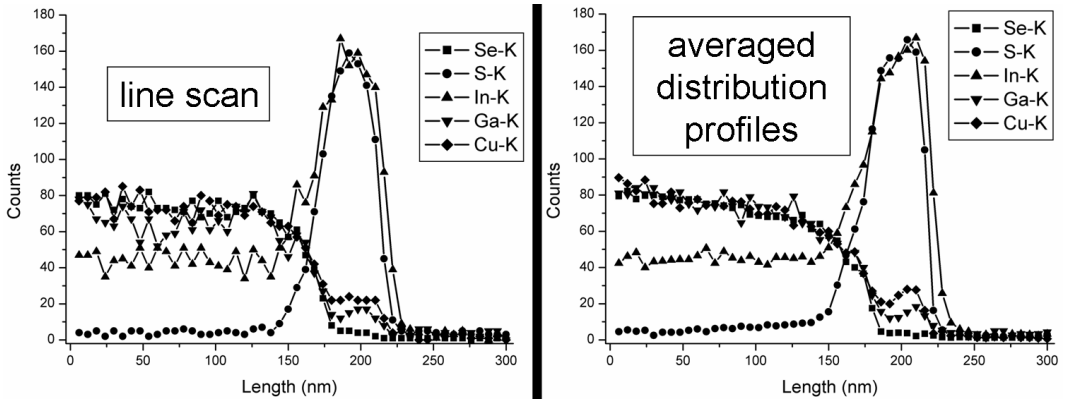

Figure 3.6: Elemental distribution profiles, both, extracted from elemental maps acquired on a CIGS/In_xS_y/epoxy glue interface, obtained from one line (left) and by averaging four profiles (right). The averaged profiles show clearly an enhanced accuracy compared with the line scan (left).

But how had those lines on the elemental maps been selected from where profiles were extracted and averaged? In all cases of buffer/CIGS interfaces reported in the present thesis, sulfide compounds have been used as buffer materials (CdS or In_xS_y). It turned out from various EDX measurements at interfaces between CIGS and these sulfide buffers that selenium and sulfur do not interdiffuse across the buffer/CIGS interface to a measurable extent. I.e., these signals were always taken as reference for those of the other elements. The buffer/CIGS interfaces in the profiles were always estimated by the cross-over of the selenium and sulfur signals. For a line where profiles were to be extracted, the selenium and sulfur signals had to decrease abruptly at the buffer/CIGS interface. At times, the selenium and sulfur signals also appeared diffuse at the buffer/CIGS interface in the elemental map (as to be seen at some positions in Fig. 3.5). There are several possible causes for such diffuse signal distributions: contamination on the specimen surface (produced during the sample preparation), which broadens the electron probe, thus deteriorates the spatial resolution considerably; an electron probe which is not optimized (note that the beam conditions may change during the course of an

elemental mapping, lasting 2-3 h); absorption of the emitted x-rays by thick specimen areas and subsequent fluorescence effects; and drift (although drift correction by cross-correlation of HAADF images was applied) during the acquisition of the elemental maps. It was always possible to relate diffuse selenium and sulfur signals to one of the causes mentioned above.

Another criterion for those lines where elemental distribution profiles were extracted and averaged was that there, the buffer/CIGS interface is oriented nearly perpendicular to these lines. Thus, the shift of the positions of the buffer/CIGS interfaces in the averaged profiles with respect to their positions in the non-averaged profiles was minimized. In all cases, this shift was estimated to be of the same order of magnitude as the point-to-point distance of the elemental maps, which was 6 nm in most cases.

Comments on the quantification of EDX measurements

It is very tempting to simply quantify the EDX data obtained on interfaces in CIGS solar cells. However, before quantifying any TEM-EDX measurement, several issues have to be considered:

1. Quantification of EDX data is always connected with the use of standards.
2. The higher the number of different elements present in an area of interest, the worse is the accuracy of the quantification.
3. In STEM mode using a probe of a few angstroms in diameter, EDX spectra are generally acquired by exciting a very small volume of the specimen. Thus, the statistics of the measurement are always very poor.
4. For EDX measurements, the number of counts should always be as large as possible to guarantee a favorable statistics.
5. For light elements, the error of their concentrations is generally larger than for those of heavier elements, since the probability of absorption is much larger for the x-rays emitted from light elements.
6. Absorption, fluorescence and channelling effects may influence the quantification considerably.
7. For automatic calculation of concentrations from EDX spectra, it is essential to know about the evaluation procedure applied (there are several methods possible, using experimental data or theoretical approaches, and the manufacturers of microscopes and detectors often give quite poor information about the software they provide).

In principle, it is possible to determine concentrations of elements with an accuracy of 1 at.%, according to the manufacturer of the FEI TECNAI F30 microscope. However, in the case of CIGS thin-film solar cells, no standards of CIGS layers are available. It seems impossible to produce a CIGS layer which might be used as a standard for EDX measurements in order to reach an accuracy of 1 at.% for each element in the sample (it has to be clarified that the accuracy varies strongly from element to element; e.g., the concentration of Se, a relatively heavy atom showing a rather homogeneous distribution over the CIGS layer, may be determined much more accurately than, e.g., that of oxygen - light element with low concentration in CIGS). This is because CIGS is a non-stoichiometric compound with an inhomogeneous distribution of elements (it is noteworthy that the distribution of elements are generally not comparable since each laboratory has its own CIGS recipe). Also, each interface on its own consists of compounds with at least 5-6 different elements altogether, i.e., the quantification is also complicated by the always large number of elements involved. Last but not least, CIGS and also other layers present in these solar cells are very sensitive to the electron beam, i.e., they may easily be destroyed. Thus, long acquisition times can not be chosen, and EDX measurements at interfaces in CIGS solar cells feature always a small number of counts per peak, i.e., they exhibit poor statistics (a larger number of counts may also be achieved by extending the area of acquisition, however, this would deteriorate the spatial resolution).

These are the reasons why EDX measurements obtained in the course of the present thesis were not quantified. However, at times, concentrations of certain elements were estimated from EDX data.
Since (as a consequence) the results from EDX measurements in the present thesis were evaluated with respect only to their qualitative information, the distribution profiles of Cu-K, Ga-K, In-K and Se-K signals were normalized to certain "counts" values in order to reveal differences between these profiles.

3.1.5 Electron energy-loss spectrometry

Electron energy-loss spectrometry also takes advantage of the interaction of incident electrons with inner-shell electrons. As shown in Fig. 3.4, an incident electron may collide with an inner-shell electron, which is then ejected from the atomic shell. Assuming that the incident electron has an energy E_0, the binding energy of the bound electron is E_B, and E_kin the kinetic energy of the electron ejected from the inner-shell, the energy loss of the incident electron, ΔE, after the interaction with the inner-shell electron may be written as

$$\Delta E = E_0 - (E_\mathrm{B} + E_\mathrm{kin}). \tag{3.1}$$

When all electrons transmitted by the specimen are detected as a function of energy, a spectrum is obtained (Fig. 3.7). It contains a large peak from all electrons which have not interacted at all while passing the specimen (zero-loss peak), lower energy-losses from interactions with plasmons (the collective oscillation of the free electrons in a material) and wedge-formed peaks from the ionization of atoms by the incident electrons. In the following, the description of the EELS technique is concentrated on the inner-core losses.

The ionization edges in the spectrum obtained by electron energy-loss spectrometry (EELS, Fig. 3.7) are related to all electron-electron interactions where $E_{\mathrm{kin}} = 0$ in equation 3.1, whereas the tails following up these edges result from electron-electron interactions with $E_{\mathrm{kin}} \neq 0$. There are always discrete ionization edges according to the discrete inner-shell electron states.

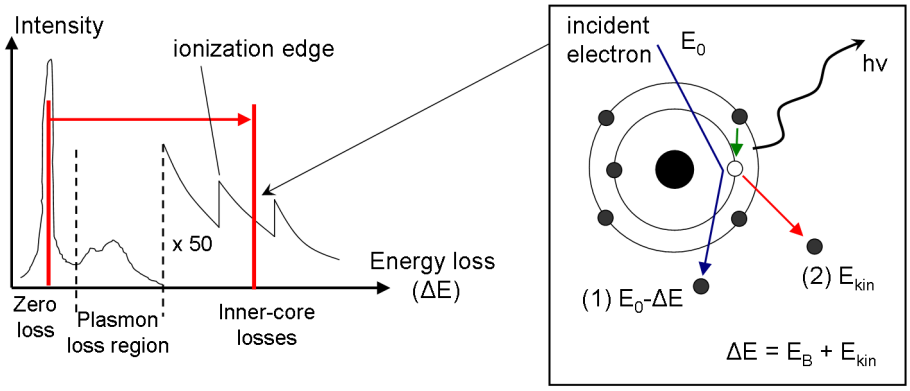

Figure 3.7: Principle of EELS. Left: example EELS spectrum with a zero-loss peak, signals resulting from interactions with plasmons, and those from inner-shell losses. Right: schematic of the interaction of an incident electron with inner-shell electrons.

Since multiple scattering of the incident electrons leads to large errors of measurement in the EELS spectrum, the area of acquisition should always show a very small thickness. Also, since scattering at light elements results in small energy losses, and since the intensity decreases gradually with increasing electron energy-loss, EELS is particularly well applicable for the chemical characterization of light elements.

3.1.6 Energy-filtered transmission electron microscopy

Since the binding energy E_{B} can be related to a specific element, EELS can be used to determine the composition on an area of interest by evaluating the ion-

ization edges in the EELS spectrum. When an area of interest is imaged with only those electrons which show certain energy losses near an ionization edge, it is possible to acquire elemental maps similar to those obtained by EDX. Therefore, an energy-filtering system is applied below the viewing screen of the microscope.

The slit of the energy filter (Fig. 3.8) may be positioned above a certain ionization edge. However, when all those electrons with appropriate energy losses in order to pass the energy-filter slit are used to image an area of interest, generally, the image will be of low quality owing to the background signals in the EELS spectrum. Thus, it is essential to reduce the influence of the background signals. One possibility is to apply the so-called *three-window method* (Fig. 3.8). In this method, two pre-edge images and one post-edge image are acquired on an area of interest. Subsequently, the background of the EELS spectrum is calculated based

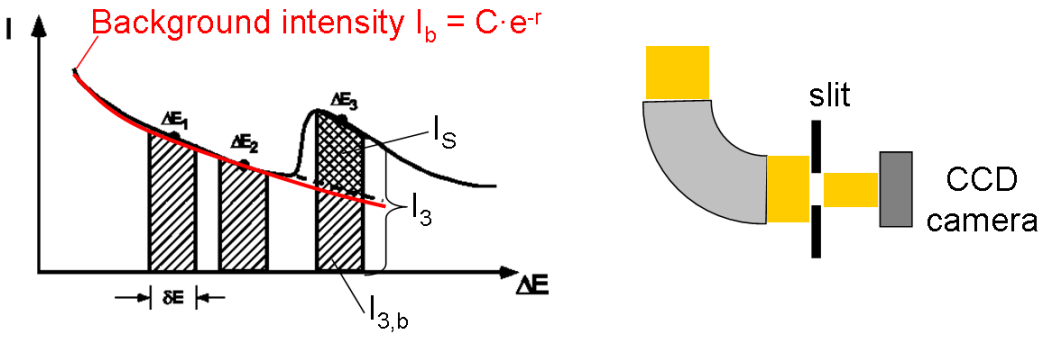

Figure 3.8: Principle of energy-filtered TEM (EF-TEM). Left: schematic of the *three-window method*. Right: the energy-filter system in a TEM, consisting of a series of magnetic prisms and a slit to shield electrons.

on the intensities of the electron energy-losses within the two pre-edge windows (ΔE_1 and ΔE_2). The exponential background-intensity function $I_\mathrm{b} = Ce^{-r}$ is adjusted by the variables C and r. By the use of this background function, the background integral $I_{3,\mathrm{b}}$ is calculated, which may be subtracted from the total integral I_3 to obtain the background-reduced amount of all electrons showing energy losses within ΔE_3, i.e., I_S.

3.2 Other characterization methods

3.2.1 Scanning electron microscopy

All plan-view scanning electron microscopy (SEM) images shown in the present thesis were obtained on a Zeiss Gemini 1530 equipped with a field-emission gun.

These SEM images are secondary-electron micrographs, and the microscope was operated by Peter Wägli, Electron Microscopy Center of the ETH Zurich, Switzerland.

3.2.2 X-ray diffraction

The x-ray diffraction (XRD) patterns shown in the present thesis were either acquired on SIEMENS D5000 diffractometers with Cu-K_α radiation, operated by Dr. David Sager (Nonmetallic Inorganic Materials, ETH Zurich, Switzerland) and Dr. Michael Wörle (Laboratory of Inorganic Chemistry, ETH Zurich, Switzerland), or on a laboratory rotating anode with Mo-K_α radiation, operated by Marije van der Klis and Prof. Dr. Bernd Schönfeld (both, Institute of Applied Physics, ETH Zurich, Switzerland).

3.2.3 Rutherford backscattering spectrometry and elastic recoil detection analysis

Both, Rutherford backscattering spectrometry (RBS) and elastic recoil detection analysis (ERDA) measurements, were performed using a 6 MV tandem accelerator at the PSI/ETH Laboratory for Ion Beam Physics, operated by Dr. Max Döbeli. RBS uses 2 MeV ^{4}He ions which are accelerated to the sample. These ions are elastically backscattered at atom cores in the sample. The incident ions lose energy mainly by the interaction with free or bound electrons, and the remaining energies of these ions after the backscattering are detected. The energy loss of the ions depends on the elements corresponding to these atom cores and on the position in the sample where the backscattering occurred. Thus, it is possible to obtain elemental depth profiles with a depth resolution of a few nm. Rutherford backscattering spectra were acquired using a silicon surface barrier detector under 165°. The collected data was simulated using the RUMP software [76].

A disadvantage of the RBS technique is that the profiles of detected elements may superimpose each other, i.e., signals from elements present in high concentration may conceal those from elements present in low concentration. Therefore, ERDA measurements were performed on some samples in addition to RBS. For the ERDA analysis, a 12 MeV ^{127}I beam was used under 18° incidence angle. The scattered recoils were identified by the combination of a time-of-flight spectrometer with a gas ionization chamber. In the spectra obtained and for the reduced number of elements present in the samples studied, a flight-time curve for a specific nucleus did not coincide with those of the other elements. The evaluation of these flight-time spectra was performed by Dr. Christian Kottler (Institute of Particle Physics, ETH Zurich, Switzerland).

3.2.4 Transmission and reflectance measurements

Transmission and reflectance spectra were measured using a Perkins Elmer UV-VIS Lambda 9 spectrometer, by the help of Paolo Losio (Institute for Quantum Electronics, ETH Zurich, Switzerland).

3.2.5 Current-voltage characteristics

Current-voltage (I-V) characteristics of solar cells have been recorded under standard AM1.5 illumination test conditions at ETH Zurich, at the ZSW or at the IPE by various colleagues. *AM1.5* is the abbreviation for "air mass 1.5" irradiation, denoting the solar insolation on the terrestrial surface when the sun stands at an angle of 42° to the normal, thus, the path of the sunlight through the atmosphere is $\frac{1}{cos(42°)} \approx 1.5$ times longer than for normal incidence. The irradiated power density for these standard illumination conditions is 100 W/cm^2, and the cell temperature is 25 °C.
Current density-voltage (j-V) characteristics were obtained from the I-V characteristics by dividing the current by the cell area. j-V characteristics feature several parameters which characterize the solar-cell performance. An example for such a characteristics is shown in Fig. 3.9. There, j_{mp} and V_{mp} correspond to the point of maximum power density, i.e., the largest area indicated by any (j, V) pair on

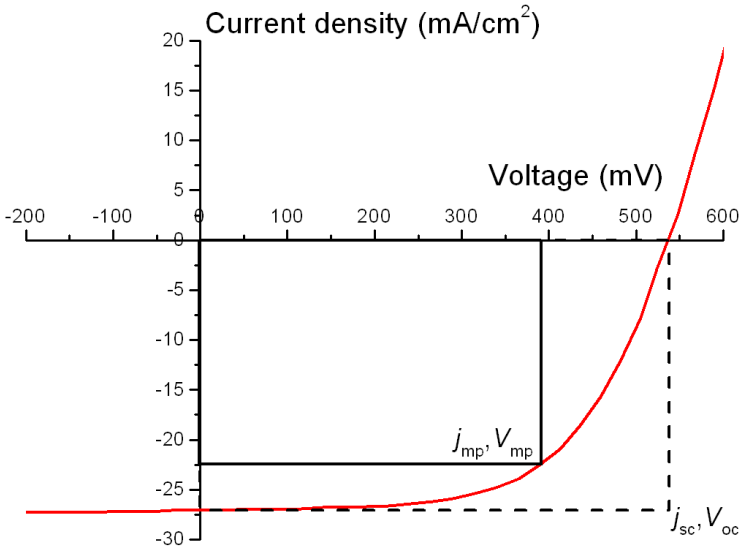

Figure 3.9: Example for j-V characteristics of a CIGS solar cell. j_{mp} and V_{mp} are current-density and voltage at the maximum power point. j_{sc} and V_{oc} are the short-circuit current density and the open-circuit voltage.

the curve. The value j for V=0 V is called *short-circuit current density* (j_{sc}), and the value V for j=0 mA/cm^2 is termed *open-circuit voltage* (V_{oc}). The *fill factor* (FF) of a solar cell is defined as

$$FF := \frac{j_{mp}\, V_{mp}}{j_{sc}\, V_{oc}}. \tag{3.2}$$

The maximum output power-density of the cell can be written as $P_{max} = j_{mp} V_{mp}$. When P_{in} is the incident power density of the illumination, the efficiency of the solar cell is defined as

$$\eta := \frac{P_{max}}{P_{in}} = \frac{j_{sc}\, V_{oc}\, FF}{P_{in}}. \tag{3.3}$$

3.2.6 Quantum efficiency measurements

Quantum efficiency (QE) is the ratio of the number of charge carriers collected by the solar cell to the number of incident photons at a specific wavelength. QE therefore relates to the response of a solar cell to the various wavelengths in the spectrum of light. If the quantum efficiency is integrated over the whole solar spectrum, that current may be obtained which a cell produces when exposed to white light. The QE can be considered as the collection probability due to the generation profile of a single wavelength, integrated over the device thickness and normalized to the number of incident photons.

Two types of QE are often considered in the case of solar cells:

- "External" QE includes the effect of optical losses such as not absorbed light and reflection at surfaces.
- "Internal" QE refers to the efficiency which has already been corrected with respect to optical losses. By measuring the transmission and reflection of a solar device, the external QE curve can be corrected to obtain the internal QE curve.

For the present thesis, external QE spectra were acquired with chopped light at a frequency of 23 Hz without background illumination at the ZSW, Stuttgart, Germany. An operational amplifier was used as current amplifier and to apply the bias voltage (operated by Stefanie Spiering, ZSW, Stuttgart, Germany).

Chapter 4

Differences between chemical-bath-deposited and physical-vapor-deposited CdS buffer layers

This chapter is based on the following publication:
Daniel Abou-Ras, G. Kostorz, A. Romeo, D. Rudmann, A.N. Tiwari, "Structural and chemical investigations of CBD- and PVD-CdS buffer layers and interfaces in $Cu(In,Ga)Se_2$-based thin film solar cells", Thin Solid Films **480-481** pp. 118-123 (2005).

4.1 Background

The highest efficiencies for thin film solar cells based on $Cu(In,Ga)Se_2$ (CIGS) and $CuInSe_2$ (CIS) absorber layers have been achieved using a CdS buffer layer deposited by a CBD process. A typical CBD solution consists of dissolved Cd^{2+} ions, thiourea ($CS(NH_2)$) and ammonia (NH_3). Ammonia has been shown to remove native oxides from the CIS surface [77]. Recently, Jiang et al. [62] studied CIGS surfaces and grain boundaries by means of scanning Kelvin probe microscopy and found that the chemical treatment involved in the CBD process modifies the electrical properties in the surface region of the CIGS layer. CBD was also reported to modify the surface of the CIS layer by forming an n-CdSe [77] or an n-$CuIn_xSe_y$ [78] intermediate layer, owing to strong reaction of the Cd with the CIS absorber. Schmid et al. [79] proposed a model that includes an n-type ordered vacancy chalcopyrite (OVC) layer between CIGS and CBD-CdS. These authors detected a

buried heterojunction between p-CIGS and n-OVC directly by means of electron-beam-induced current measurements. In contrast to these results, Kylner et al. [80] found no evidence of an intermediate compound between CIGS and CBD-CdS. The role of the CdS buffer in the p-n junction formation will be treated further below.

Although the CBD process for CdS deposition is very attractive owing to high solar conversion efficiencies, for industrial production, an in-line vacuum deposition as, e.g., physical vapor deposition (PVD), is preferred. However, the highest efficiencies achieved by PVD-CdS buffer layers hardly exceed 13%. Always (e.g., [40, 41]), a clearly poorer photovoltaic performance of as-grown solar cells with PVD-CdS buffer layers than of solar cells with CBD-CdS buffer layer has been found. Recently, Romeo et al. [40] published results on electrical investigations of solar cells with in-situ and ex-situ deposited PVD-CdS buffer layers and compared them with those of standard cells with CBD-CdS buffer layers.

In the present chapter, investigations of structural and chemical properties of CBD- and PVD-CdS buffer layers and their interfaces with CIGS are presented. These results help to understand the reasons for the difference in the photovoltaic performance of solar cells produced by these two methods.

4.2 Results and discussion

In Fig. 4.1, j-V characteristics of two CIGS solar cells are displayed, both, produced in the same run, however, one consisting of a CBD- and the other of a PVD-CdS buffer layer. The electrical properties, especially the open circuit voltage V_{oc}, differ significantly, probably owing to different interface and recombination properties.

In the plan-view SEM images in Fig. 4.2, small CdS grains are visible on top of large CIGS grains. PVD-CdS grains (b) are much larger than those of CBD-CdS (a). The size of the PVD-CdS grains is approximately 70-80 nm, whereas the size of the CBD-CdS grains is too small to be determined from the SEM images. In the BF-TEM images (Fig. 4.3), cross-sections of the interfaces between CIGS, CdS and ZnO are shown. By TEM as by means of SEM, the PVD-CdS grains (Fig. 4.3b) were found to be much larger than those of CBD-CdS (Fig. 4.3a). The PVD-CdS grain sizes from TEM agree well with the values obtained by means of SEM (about 70 nm). For the CBD-CdS layer, grain sizes of about 10-15 nm were determined. The CBD-CdS layer thickness was about 50 nm, whereas the PVD-CdS layer thickness was about 70 nm.

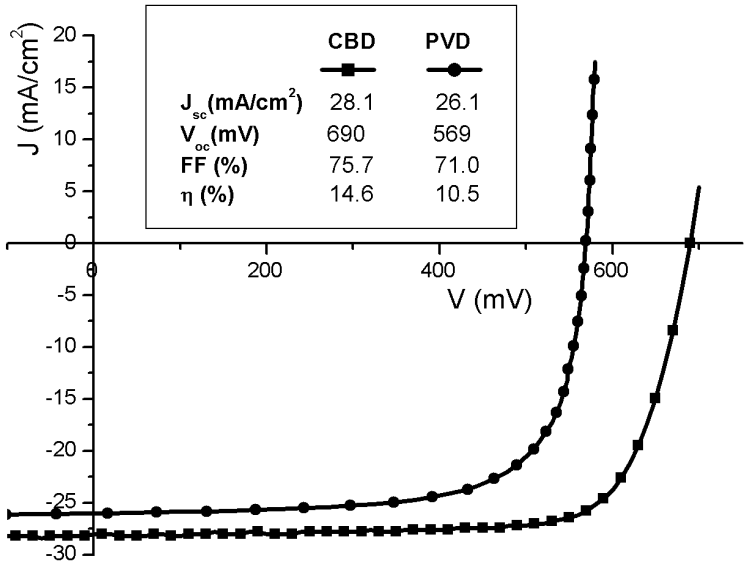

Figure 4.1: j-V characteristics under AM1.5 illumination of solar cells with CBD-CdS and PVD-CdS buffer layer. Solar cells with CBD-CdS buffer layer always show higher efficiencies.

Fig. 4.4 shows the Cd signal from the CIGS/PVD-CdS/ZnO interface, obtained by means of EF-TEM. In contrast to prevailing views, the PVD-CdS layer shows a continuous coverage of the CIGS surface over a range of several micrometers, similar to the CBD-CdS coverage.

In Fig. 4.5, SAED patterns for both the CIGS/CBD-CdS/ZnO interface (a) and the CIGS/PVD-CdS/CIGS interface (b) are shown. For the CBD-CdS layer (a), a hexagonal crystal structure was found. In general, CBD-CdS layers on CIGS, $CuInSe_2$ (CIS) or $CuGaSe_2$ (CGS) were reported to crystallize in both, hexagonal (wurtzite, $a = 0.414$ nm, $c = 0.671$ nm [81]) and cubic (zincblende, $a = 0.582$ nm [82]) crystal structures [78, 83, 84, 85, 86, 87]. Furlong et al. [85] showed that the crystal structure of the CBD-CdS layer depends on the CIS substrate orientation. Nadenau et al. [86] found that the formation of hexagonal and cubic crystal structures of CBD-CdS depends on the substrate temperature during CBD. Thus, different CIGS deposition parameters and CBD-CdS recipes may lead to different CdS growth and crystal structures, and caution is advised not to generalize the detected crystal structure. Although wurtzite is the most stable crystal structure of CdS, the energy difference between wurtzite and zincblende is rather small [88], thus, the transition may occur with high probability. CdS layers exhibiting both crystal structures may be deposited. Also, one has to take into account that the

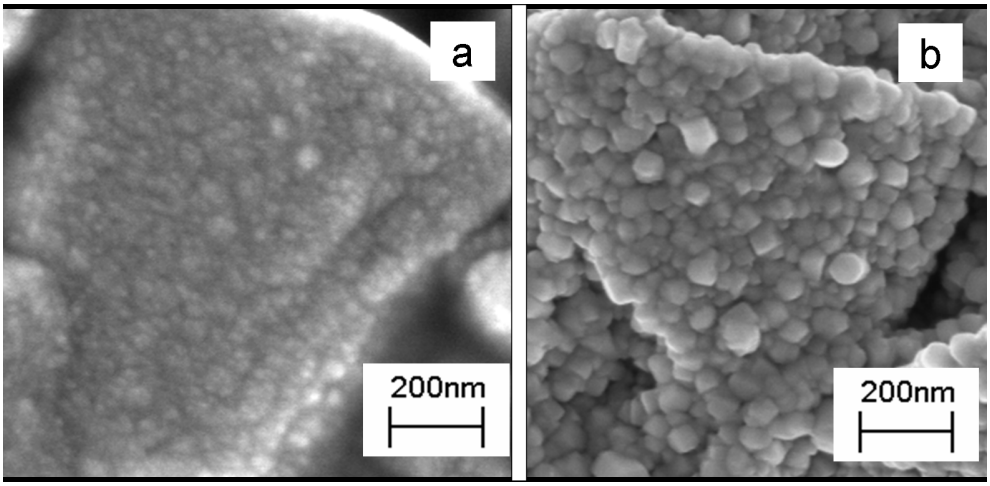

Figure 4.2: Plan-view scanning electron micrographs of CdS grains on large CIGS grains. PVD-CdS layers (b) show significantly larger grain sizes than CBD-CdS (a).

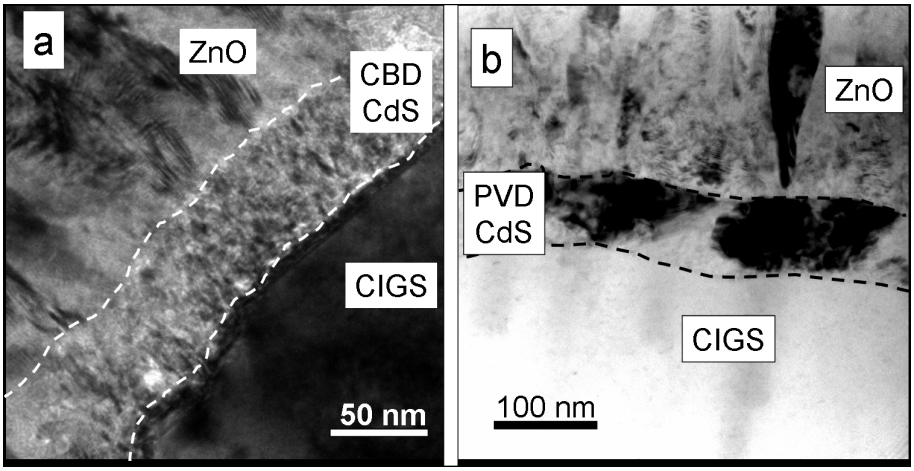

Figure 4.3: Bright-field transmission electron micrograph of the CIGS/CBD-CdS/ZnO (a) and CIGS/PVD-CdS/ZnO (b) interfaces. Grain sizes are clearly larger for PVD-CdS than for CBD-CdS layers.

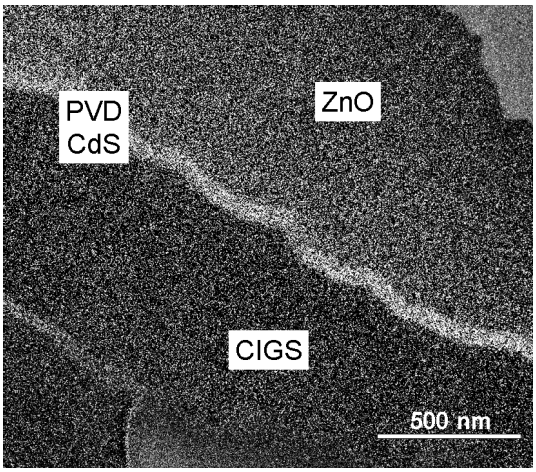

Figure 4.4: Cd signal of the CIGS/PVD-CdS/ZnO interface region, obtained by means of energy-filtered transmission electron microscopy. The PVD-CdS layer shows a uniform conformal coverage of the CIGS surface.

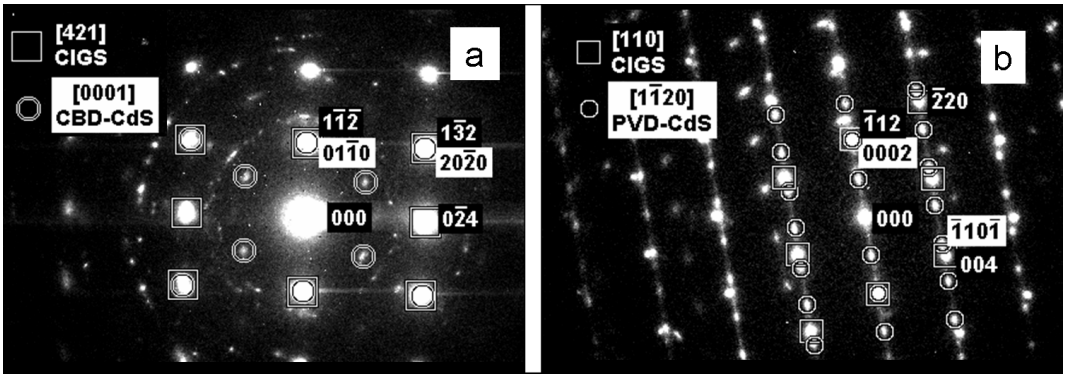

Figure 4.5: Electron diffraction pattern for the CIGS/CBD-CdS/ZnO (a) and the CIGS/PVD-CdS/ZnO (b) interfaces. The growth of CBD-CdS on CIGS (a) is nearly coherent, whereas the growth of PVD-CdS on CIGS (b) is clearly incoherent.

SAED patterns of, e.g., $[111]_{cub}$ and $[00.1]_{hex}$ CdS zone axes are difficult to distinguish, i.e., they might occasionally be misinterpreted.
A good lattice match of the CBD-CdS on the tetragonal CIGS layer is visible in Fig. 4.5a, since the reflections from CIGS-{112)[1] and CdS-{01.0) planes coincide, as well as the reflections from CIGS-{132) and CdS-{10.0) planes. For the PVD-CdS layer (Fig. 4.5b), a hexagonal crystal structure was also found. However, the lattice mismatch between PVD-CdS and CIGS is quite large; only CIGS-{112) and CdS-{00.1) reflections coincide in the diffraction pattern. The difference in lattice (mis)match between CBD- and PVD-CdS may be due to the fact that the CBD-CdS layer is a mixture of CdS, Cd-OH, and Cd-O [80], which offers a range of lattice constants that apparently leads to a better lattice match to CIGS than the lattice constants of PVD-CdS. In both SAED patterns (Fig. 4.5), reflections from the hexagonal ZnO layer are also visible. For the CBD-CdS sample, the ZnO grains show arbitrary orientations (diffraction rings), which can be expected from the small CBD-CdS grain size. For the PVD-CdS sample, a preferential growth orientation in [11.0] direction of the hexagonal ZnO on the PVD-CdS layer was found.

In Fig. 4.6a, a HR-TEM micrograph of the CIGS/CBD-CdS interface corresponding to the SAED pattern in Fig. 4.5a is shown. The marked lattice spacings in

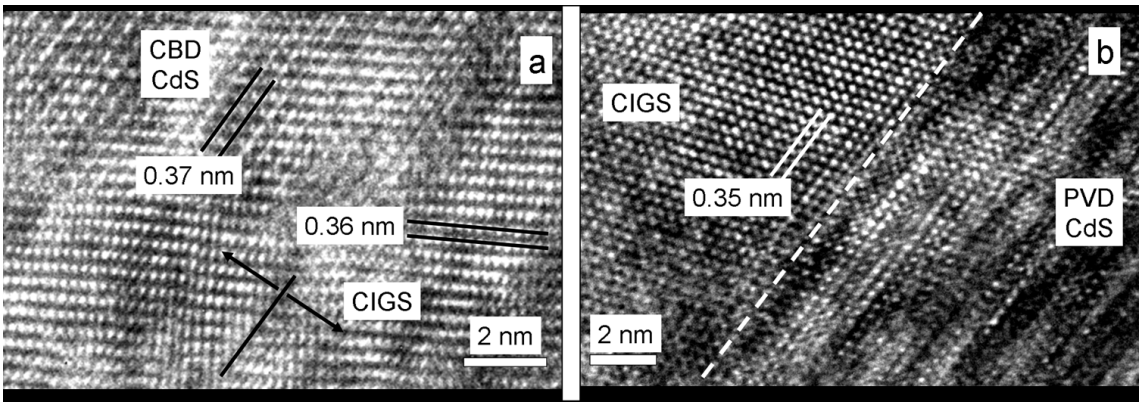

Figure 4.6: High-resolution transmission electron micrograph of the CIGS/CBD-CdS (a) and of the CIGS/PVD-CdS (b) interfaces. In (a), the interface (see arrows) runs from the right-bottom corner (CIGS) to the left-top corner (CdS). In (b), the approximate position of the interface is given by the dashed line.

the CBD-CdS layer (about 0.37 nm) and in the CIGS-layer (about 0.36 nm) agree well with the calculated values of hexagonal CdS-{10.0) planes, 0.359 nm, and of CIGS-{112) planes, 0.366 nm (calculated from a = 0.578 nm and c = 1.16 nm [90]).

[1]The mixed notations {*hkl*) introduced in Ref. [89] are used to differentiate the first two indices from the third one: for the first two indices, permutations (inclusive sign) are allowed.

As expected from the SAED patterns, the micrograph shows good lattice match of CBD-CdS on CIGS. The HR-TEM micrograph of the CIGS/PVD-CdS interface in Fig. 4.6b reveals planar strains in the PVD-CdS, visible by a high density of defects (probably stacking faults and twins), which arises from the compensation of the lattice mismatch. Defects generally contribute to recombination in the space charge region, which may lead to lower efficiencies.

Chemical properties of the CIGS/CBD-CdS (a) and CIGS/PVD-CdS (b) interfaces are shown by the linear composition profiles in Fig. 4.7. For reasons of clarity, the In and Ga signals were omitted, since they do not show any significant

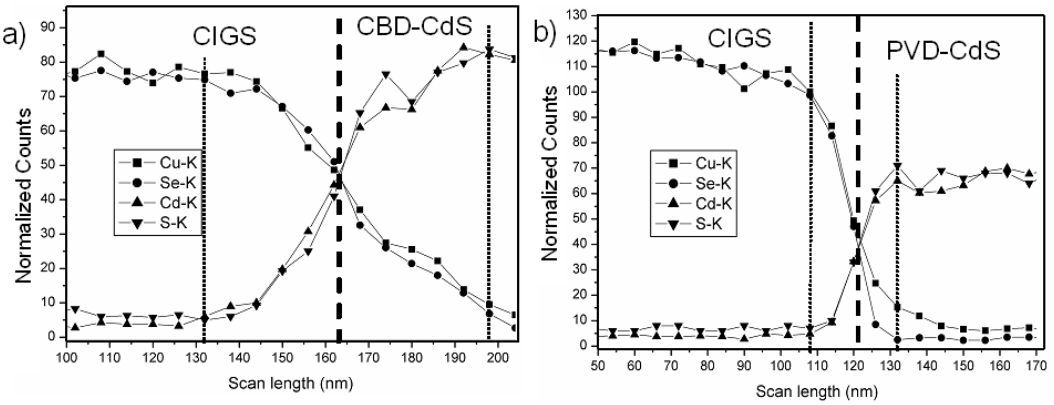

Figure 4.7: Linear elemental distribution profiles over the CIGS/CdS interface extracted from elemental mappings, obtained by energy-dispersive X-ray spectrometry. For the CBD-CdS sample (a), there is Cu depletion and an increase of the Cd signal visible on the CIGS side of the interface, whereas no such behavior was found for the PVD-CdS sample (b). The interface between CIGS and CdS is shown by the dashed-line whereas the dotted lines indicate an estimate of the transition interfacial region. The Cu-K signals were normalized to the Se-K level on the CIGS side in order to provide an easier comparison.

difference to the Se signal. Although the difference between the Cu and the Se signals, and also between the Cd and the S signals, is very small in Fig. 4.7a, the significance of these results can be assured by comparison of several linear profiles extracted from elemental mappings. In both diagrams (a and b), there is quite a clear cross-over of the Cu and Se signals with the Cd and S signals, and that is where the interface between CIGS and CdS was estimated (dashed lines). For both CIGS/CdS interfaces, Cu diffusion from the CIGS into the CdS layer is visible, since the Cu signal (■) decreases more slowly on the CdS side of the interface than the signal of Se. As mentioned by Bube [91], Cu doping of CdS increases its photoconductivity which may affect the electronic properties of the CIGS/CdS

heterojunction under illumination.
Only for the CBD-CdS sample (a), also a probable depletion of Cu and enrichment of Cd on the CIGS side of the interface is visible: the Cu signal is significantly lower than the Se signal, and the Cd signal (▲) decreases more slowly on the CIGS side of the interface than the S signal. Considering the probable Cu depletion in the case of the CBD-CdS/CIGS interface, one has to take into account that not all of the depleted Cu may diffuse from CIGS into CdS. Part of it will be dissolved in the CBD bath. Also, since CBD-CdS is not a stable compound, i.e., it consists of e.g. Cd-OH and Cd-O phases where Cd is not strongly bonded, Cd doping of the CIGS near-interface region is more likely in the case of CBD-CdS.
Compared with the CIGS/PVD-CdS interface (Fig. 4.7b), the CIGS/CBD-CdS (Fig. 4.7a) interface is not abrupt: it shows quite a large transition interfacial region (dotted lines). It appears that Cu from the CIGS layer is incorporated into the CBD-CdS layer, depleting at the CIGS side of the interface, and that Cd diffuses from CBD-CdS into CIGS, occupying Cu vacancies in the near-interface region. Nakada et al. [87] confirmed the Cu and Cd interdiffusion by means of EDX line scans. Ramanathan et al. [64] discussed the influence of Cd on CIGS during the CBD process: owing to the similar ion radii of Cd^{2+} (0.97 Å) and Cu^{+} (0.96 Å), Cd ions may act as substitutional donors on Cu sites. By means of x-ray photoelectron spectroscopy, these authors determined a Cd concentration of 20 at.% in the near-interface region on the CIGS side. Thus, this region may be inverted from *p*-type to *n*-type.
Jiang et al. [92] identified a buried junction at the CBD-CdS/CIGS interface directly by means of scanning Kelvin probe microscopy. In addition, Wada et al. [93] showed that the treatment of the CIGS surface with a Cd^{2+} aqueous solution prior to PVD-CdS deposition improves the photovoltaic performance of the appropriate solar cells significantly. The absence of Cd excess and Cu depletion on the CIGS side of the PVD-CdS/CIGS interface (Fig. 4.7b) and thus the probable absence of a type-inverted region (which would imply a buried junction) on the CIGS side of the interface may also lead to lower efficiencies in as-grown solar cells with PVD-CdS buffer layer.

4.3 Conclusion

Structural and chemical properties of CBD- and PVD-CdS/CIGS layers and interfaces were compared. PVD-CdS layers show much larger grain sizes than CBD-CdS layers, and also a higher structural defect density (probably stacking faults and twins) at the CIGS/PVD-CdS interface, owing to a larger lattice mismatch. These structural defects may affect the photovoltaic performance.
For the case of PVD-CdS, the interface to the CIGS is quite abrupt, whereas on the

CIGS side of the CBD-CdS/CIGS interface Cu depletion and Cd enrichment may have occurred. Cu in CdS increases its photoconductivity, and Cd can occupy Cu vacancies. The results of the Cu and Cd interdiffusion provide an indication of an inversion of the near-interface region from *p*-type CIGS to *n*-type. The probable absence of this inversion in solar cells with PVD-CdS buffer layers is a possible reason for their lower efficiencies compared with solar cells with CBD-CdS buffer layer.

It has to be pointed out that efficiencies similar to those of CIGS solar cells with CBD-CdS buffers have been shown to be achievable also in cells with PVD-CdS buffer layers after the complete cells had been annealed in air at 200 °C for several minutes [41, 94]. Probably, this increase in efficiency results from annealing-induced interdiffusion processes, which may change the electrochemical potential at the PVD-CdS/CIGS interfaces in such a way that the band-alignment between buffer and absorber improves, probably reducing recombination at this interface [41].

Chapter 5

Analyses of interfaces between In_xS_y buffers and $Cu(In,Ga)Se_2$ absorbers

This chapter is in part based on the following publications:

- D. Abou-Ras, D. Rudmann, G. Kostorz, S. Spiering, M. Powalla, and A.N. Tiwari, "Microstructural and chemical studies of interfaces between $Cu(In,Ga)Se_2$ and In_2S_3 layers", J. Appl. Phys. **97**(8) no. 084908 (2005).

- D. Abou-Ras, G. Kostorz, A. Strohm, H.W. Schock, and A.N. Tiwari, "Interfacial layer formations between $Cu(In,Ga)Se_2$ and In_xS_y layers", J. Appl. Phys. **98**(12) no. 123512 (2005).

5.1 Background

Thin-film solar cells based on CIGS yield highest efficiencies with CdS buffer layers deposited by chemical bath deposition (CBD). However, there are several reasons in favor of a substitution of CdS as material and CBD as deposition method (please refer to section 1.3). Therefore, alternative buffer layers and deposition methods have been investigated.

A promising candidate for the application as buffer-layer material in CIGS solar cells is In_2S_3. CIGS solar cells containing an In_2S_3 buffer layer deposited by ALD show efficiencies of up to 16.4 % [95]. This is the highest efficiency ever obtained using In_2S_3 buffers in CIGS solar cells. However, the disadvantages of the ALD technique are its low deposition rate and that its up-scaling from small

laboratory cells to modules with areas of 120x60 cm^2 is associated with high expenses and is thus uneconomical, owing to the absence of appropriate commercial ALD machines.
Apart from ALD-In_2S_3, also PVD is used to produce In_2S_3 buffer layers. CIGS solar cells with In_2S_3 buffer layers co-evaporated from In and S powder have shown efficiencies of up to 12.4 % [96]. With buffer layers evaporated from In_2S_3 powder, efficiencies of up to even 14.8 % without anti-reflection coating have been obtained [71]. Best efficiencies with powder-evaporated In-S buffer layers have been achieved at substrate temperatures of 23 °C and after additional air-annealing at 200 °C for several minutes [71]. For substrate temperatures ranging from 23 to 200 °C, as-grown solar cells with indium sulfide buffer layers have shown good photovoltaic performance which improved significantly after air-annealing. During the powder-evaporation process which is realized by heating the In_2S_3 powder to a crucible temperature of 725 °C, a substantial S-loss in the powder (due to decomposition and high vapor pressure of S) may change the In/S ratio. As a consequence, the evaporated layers are not pure In_2S_3, but consist of different indium sulfide compounds [71]. Thus, in the present chapter, the notation "In_xS_y" is used for the indium sulfide buffer layers deposited by physical vapor deposition.
In addition to ALD and powder evaporation, In_2S_3 buffer layers have also been deposited by magnetron sputtering, resulting in high efficiencies of up to 13.3% [73]. Sputtering of In_2S_3 provides a rapid deposition and is a process easy to be up-scaled. Thus, this technique meets important requirements for the industrial production of CIGS solar cells. As for powder-evaporated In_xS_y, different S concentrations (compared with the In_2S_3 stoichiometry of the targets) have been reported for various sputtered indium sulfide buffers [73]. Therefore, for these indium sulfide layers, the notation "In_xS_y" is also used.

Although a certain standard of performance has already been reached, research and development of cells with indium sulfide buffer layers is still in progress. Several parameters as, e.g., the substrate temperature during the In_2S_3 or In_xS_y deposition, are varied. Insight into internal processes influenced by these parameter variations represents essential information which helps to improve the photovoltaic performance of these solar cells.
In the present chapter, experimental results and possible explanations will be presented on how substrate temperature, the presence of Na and air-annealing influence the interface formation between CIGS and In_xS_y deposited by ALD, sputtering and powder-evaporation.

5.2 Interfaces between atomic-layer-deposited In_2S_3 and Cu(In,Ga)Se_2

At these interfaces, the influence of the substrate temperature and of Na on the In_2S_3/CIGS interface formation was studied.

5.2.1 Deposition temperature dependence

In Fig. 5.1, small In_xS_y grains are visible on large CIGS grains. At low temperature (140 °C), the grains do not appear clearly resolved and seem to be a mixture

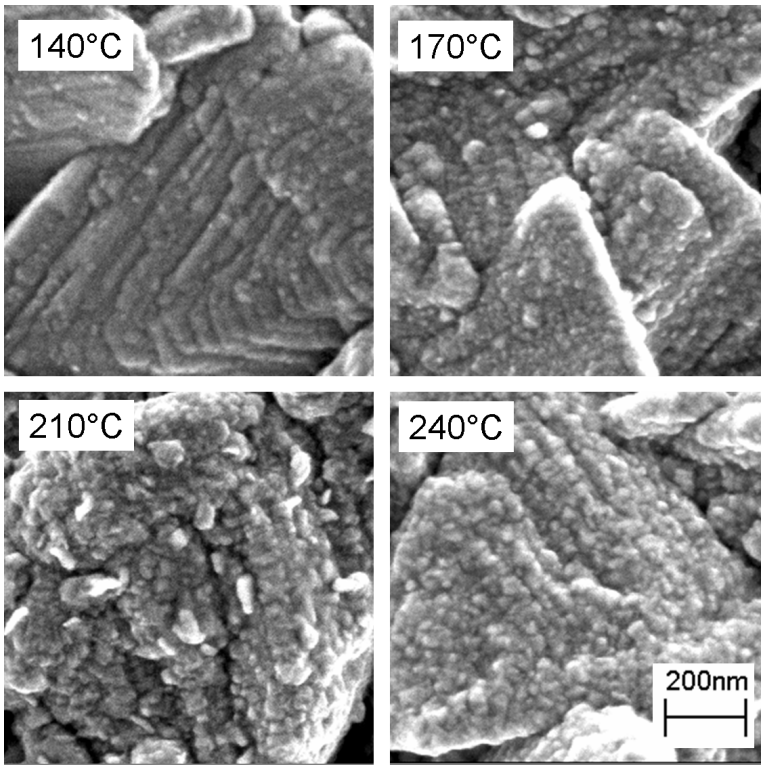

Figure 5.1: Plan-view scanning electron micrographs of small In_2S_3 grains on large CIGS grains (on SLG/Mo substrates). The In_2S_3 layers were grown at different temperatures.

of small and large grains. At higher temperature (240 °C), the grains are well resolved, and the variation of grain size becomes smaller, which has also been reported by Naghavi et al. [97]. As shown in Fig. 5.1, no significant increase in grain size with increasing temperature is visible. Fig. 5.2 shows BF-TEM images from interfaces of CIGS with In_2S_3 deposited at 210 °C and 240 °C. Grain sizes of approximately 20-25 nm were detected for both samples. The In_2S_3 layer

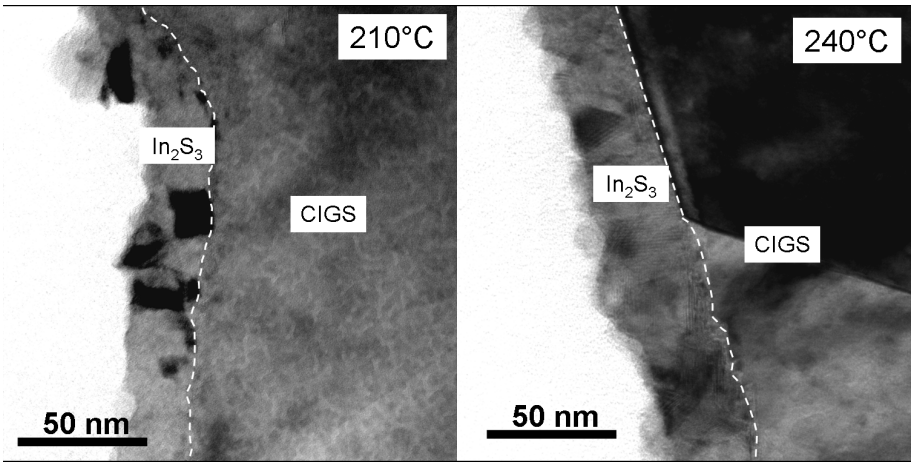

Figure 5.2: Bright-field transmission electron micrographs of the interface of CIGS with In_2S_3 layers grown at 210 °C and 240 °C. In both cases, the In_2S_3 layer thickness is about 30-35 nm, and the grain sizes about 20-25 nm.

thicknesses in both samples are about 30-35 nm. The interfaces between CIGS and In_2S_3 (dashed curves) were determined by comparison with other micrographs from the same area.

In the SAED pattern of the 210 °C sample (Fig. 5.3), orientation relationships between the tetragonal CIGS $\{1\bar{1}2\}$ and the tetragonal In_2S_3 $\{10\bar{3}\}$ planes and also between the CIGS $\{\bar{1}10\}$ and the In_2S_3 $\{11\bar{6}\}$ planes are visible. In contrast to the 210 °C sample, no orientation relationship was detected between CIGS and the In_2S_3 layer deposited at 240 °C. Apparently, this In_2S_3 layer has no preferred orientation, since faint, but continuous diffraction rings are visible in the SAED pattern (the rings have been outlined by drawn rings as a guide to the eye, also, the reflections attributed to the In_2S_3 layer have been marked by squares).
The HR-TEM images from the CIGS/In_2S_3 interface of both, the 210 °C and the 240 °C samples (Fig. 5.4), show an abrupt interface. Also for both samples, twice of the detected lattice spacing of CIGS {112) planes (0.34 nm) agrees well with the spacing of In_2S_3 {103) planes (0.68 and 0.66 nm) [90, 98]. In contrast to the 210 °C In_xS_y/CIGS interface, at 240 °C, the In_xS_y/CIGS interface is extended by an additional layer of about 10 nm thickness. Probably, this layer is responsible for the fact that the 240 °C In_2S_3 layer does not show a preferred orientation. At an In_2S_3 deposition temperature of 240 °C, at some positions, an intermediate layer was not found. It is assumed that for deposition temperatures higher than 240 °C, the thickness of the layer may increase and become continuous. The nature of this layer will be further addressed in chapter 6.

Linear elemental distribution profiles, extracted from EDX elemental mappings

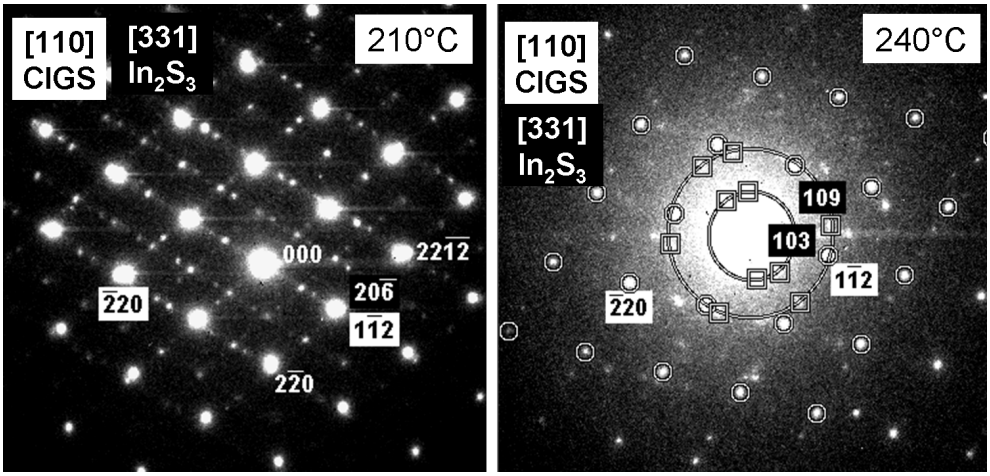

Figure 5.3: Selected-area electron diffraction patterns from the interface of CIGS with In_2S_3 layers grown at 210 °C and 240 °C. While there is a clear orientation relationship visible between In_2S_3 {103) and CIGS {112) planes in the 210 °C sample, such an orientation relationship is not visible for the 240 °C sample. Circles: CIGS, squares: In_2S_3. The diffraction rings from the In_2S_3 layer are barely visible in the original image, thus, they were outlined by drawn circles.

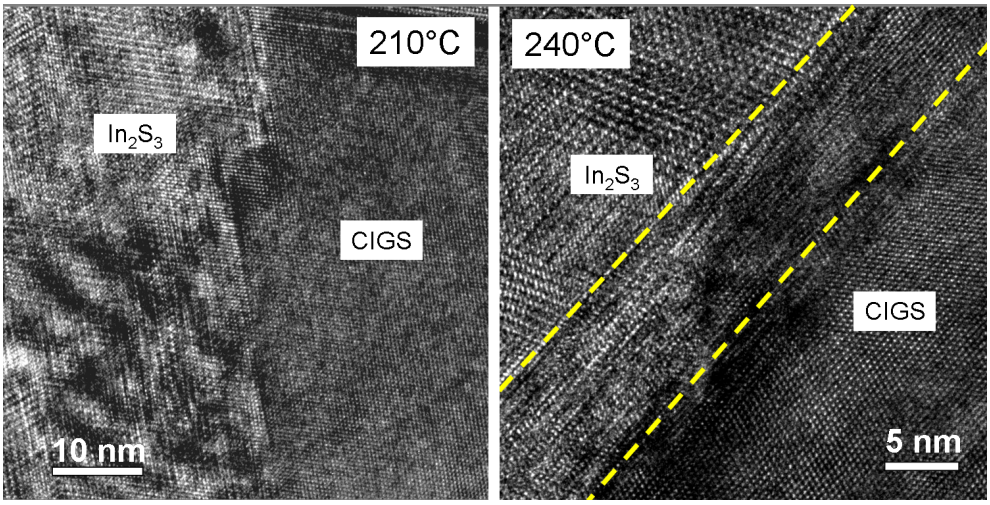

Figure 5.4: High-resolution transmission electron micrograph from the interface of CIGS with In_2S_3 layers grown at 210 °C and 240 °C. While there is a good lattice match between In_2S_3 and CIGS for the 210 °C sample, a new phase appears between CIGS and In_2S_3 in the 240 °C sample.

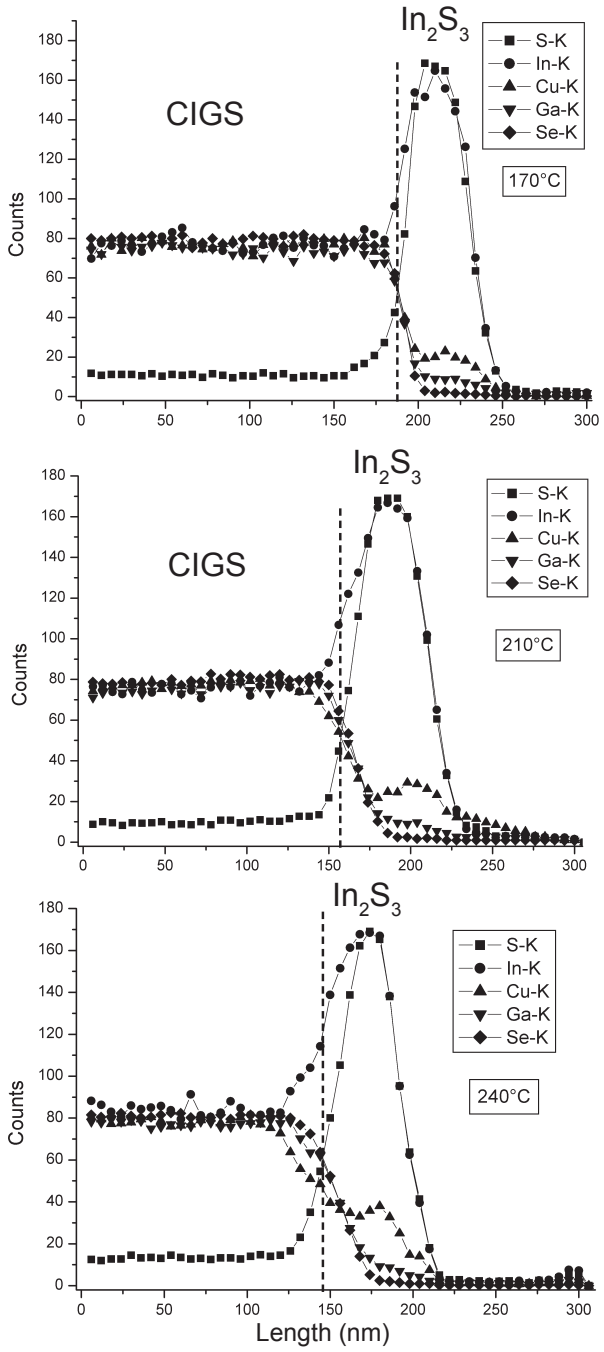

Figure 5.5: Linear elemental distribution profiles across CIGS/In_2S_3 interfaces, extracted from EDX elemental mappings. Cu and Ga diffusion from CIGS into In_2S_3, Cu depletion and In enrichment on the CIGS side of the interface. All effects increase with increasing In_2S_3 deposition temperature.

on CIGS/In_2S_3 interfaces, are shown in Fig. 5.5 for the 170 °C, the 210 °C and the 240 °C samples. The dashed lines indicate the positions of the CIGS/In_2S_3 interfaces, given by the crossover of the Se and the S signals; these two elements did not show any significant change in any of the samples investigated, thus Se and S are considered to interdiffuse only to a negligible extent. The linear profiles reveal a strong Cu and a slight Ga diffusion from CIGS into In_xS_y. On the In_2S_3 side in the very vicinity of the CIGS/In_2S_3 interfaces, the Cu and Ga signals decrease much more gradually than the Se signal. The extent of their diffusion increases with increasing deposition temperature.
In addition to the Cu and Ga diffusion, an obvious depletion of Cu and an enrichment of In are visible on the CIGS side of the interface, especially in the case of the 240 °C sample. Apparently, depletion and enrichment of the elements are also enhanced with increasing deposition temperature of the In_2S_3 layer. Py et al. [99] investigated the interdiffusion in the CuS-Cu_2S-In_2S_3 system and suggested that Cu diffuses into the In_2S_3 spinel phase, occupying both vacancies and In sites. Such a Cu diffusion and occupation process may also occur on the In_2S_3 side of the interface, in addition to the Cu depletion and In enrichment on the CIGS side of the interface, which indicates that In might occupy Cu vacancies. Cu ions in the In_2S_3 buffer layer may change its electrical properties strongly. The *p*-*n* junction formation between CIGS and In_2S_3 may be deteriorated, if excess Cu is present in the In_2S_3 buffer layer. At a sufficiently high temperature, an interface layer may form, as it is the case for the 240 °C sample.
For easier comparison, Cu-K linear elemental distribution profiles for samples with In_2S_3 layers deposited at 170 °C, 210 °C and 240 °C are shown in Fig. 5.6. It was found that the integrals under the Cu-K profiles are approximately the same for all samples investigated, i.e., it is always the same amount of Cu that shows a different distribution across the CIGS/In_2S_3 interface for different In_2S_3 deposition temperatures. Assuming a Cu concentration of 25 at.% on the CIGS side of the interface and an In_2S_3 buffer, the Cu concentration in the In_xS_y layer can be estimated to be about 5, 8 and 10 at.% for the 170 °C, 210 °C and 240 °C samples.

In order to verify that the Cu distribution profiles shown in Fig. 5.6 can be traced back to Cu diffusion from CIGS into In_2S_3, these Cu-K signals (in number of counts) in dependence of the position x across the CIGS/In_2S_3 interface were simulated using the thin-film solution of Fick's second law $\frac{\partial}{\partial t}\, c(x,t) = D\, \frac{\partial^2}{\partial x^2}\, c(x,t)$

$$c_{\mathrm{Cu}}(x,t) = \frac{Q_{\mathrm{Cu}}}{2\sqrt{\pi\, D_{\mathrm{Cu}}\, t}} \exp\left(-\frac{x^2}{4\, D_{\mathrm{Cu}}\, t}\right) \tag{5.1}$$

Here, c_{Cu} is the concentration of Cu (in counts), Q_{Cu} is the total amount of diffused Cu (in signals/nm if "counts" is considered to be signals/nm^2; since the distribution profiles of the Cu-K, In-K, Ga-K and Se-K signals are normalized to a certain

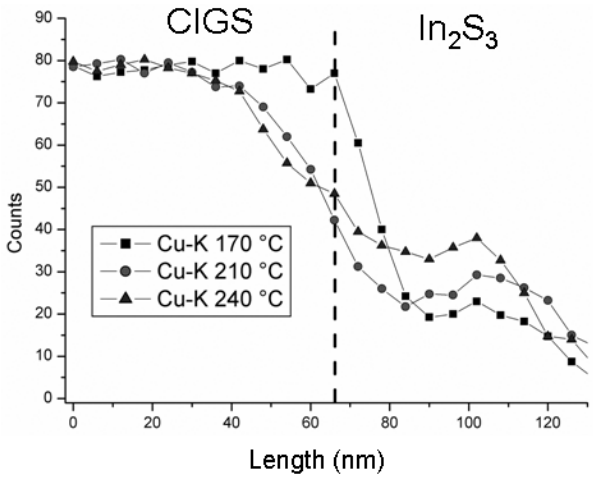

Figure 5.6: Linear Cu-K elemental distribution profiles across CIGS/In_2S_3 interfaces, for different deposition temperatures. The integrals under the Cu-K profiles are the same for all samples investigated. Local maxima of the Cu-K profiles appear inside the In_2S_3 layer.

"counts" value, this unit can be considered arbitrary, anyway), and D_{Cu} is the diffusion constant of Cu in In_2S_3. For these simulations, D_{Cu} is considered independent of the position x. The time of diffusion, t, was equated with the deposition duration of the ALD-In_2S_3 layers of about 2 h.
The Cu distribution profiles and their simulations are shown in Fig. 5.7. As it appears, the measured profiles can be well approximated by the simulations based on eq. 5.1, with the exception of the local maxima. The parameters Q_{Cu} and D_{Cu} used for these simulations are summarized in Table 5.1. The amount of diffused Cu, Q_{Cu}, and the diffusion constant of Cu in In_2S_3, D_{Cu}, both increase with increasing temperature, as expected.
Although these simulations are only a rough approach, the diffusion constant D_{Cu} may be estimated to be in the order of 1x10^{-16}-1x10^{-15} $\frac{cm^2}{s}$.

Table 5.1: The parameters Q_{Cu} and D_{Cu} used for the simulation of Cu-K elemental distribution profiles across CIGS/In_2S_3 interfaces for various substrate temperatures.

Temperature	Q_{Cu} (signals/nm)	D_{Cu} ($\frac{cm^2}{s}$)
170 °C	2700	1x10^{-16}
210 °C	5500	6x10^{-16}
240 °C	7700	1x10^{-15}

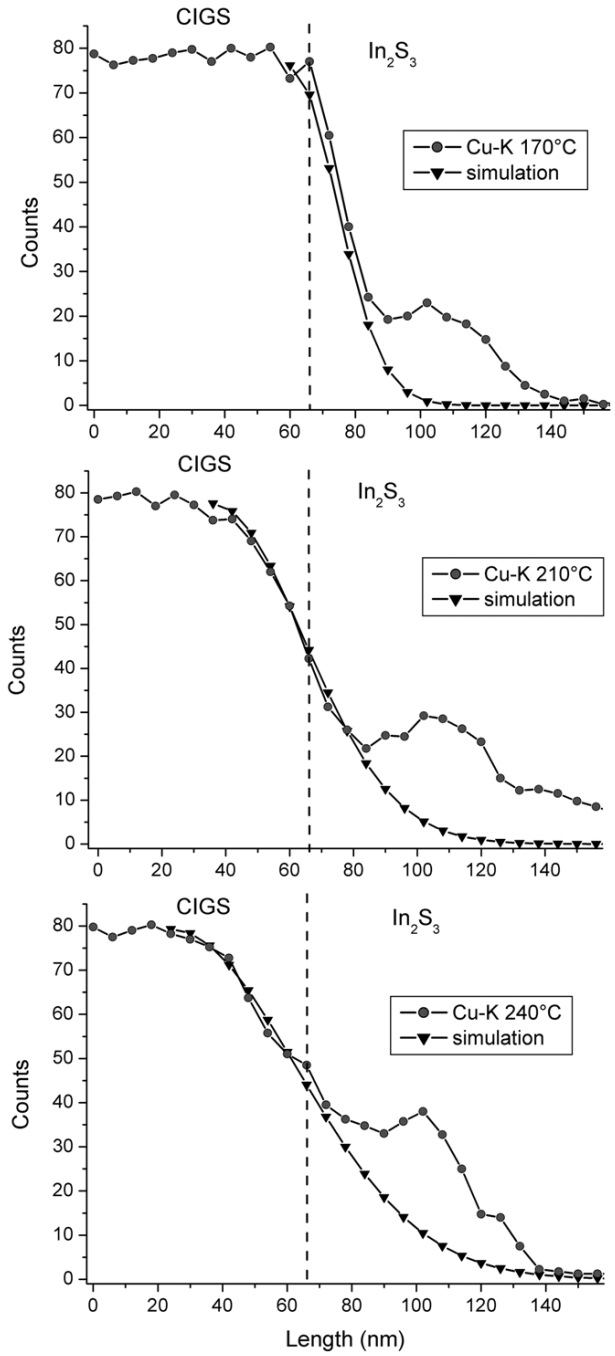

Figure 5.7: Linear Cu-K elemental distribution profiles across CIGS/In_2S_3 interfaces, for different deposition temperatures, and their simulations using the thin-film solution of Fick's second law. The measured profiles can be well approximated by the simulations based on eq. 5.1, with the exception of the local maxima.

Local maxima of the Cu-K linear elemental distribution profiles inside the In_2S_3 layer are visible in all samples studied (Figs. 5.6 and 5.7). These maxima are not artifacts of the measurements, but can be interpreted in the following way: Cu diffuses from the CIGS into the In_2S_3 layer, occupying vacancies and In sites, and In diffuses into the CIGS layer, occupying Cu vacancies. Generally, Cu ions show a much higher mobility than In ions, thus, it can be assumed that Cu diffuses more rapidly into In_2S_3 than In into CIGS, which would lead to a Cu depletion on the CIGS side of the interface and to an enrichment of Cu on the In_2S_3 side of the interface, forming a local maximum. Considering also the occupation of Cu vacancies by In ions, these assumptions would imply the inversion of the near-interface region of CIGS from *p*-type to *n*-type.

From the present results, the following interpretation of CIGS/ALD-In_2S_3 interfaces with respect to the In_2S_3 deposition temperature was developed. With increasing deposition temperature, Cu, Ga and In interdiffusion becomes more enhanced, which leads to an inversion of the near-interface region of CIGS from *p*-type to *n*-type. The inverted region becomes broader with increasing deposition temperature, which seems to have a beneficial effect on the junction formation. Thus, the cell performance improves. At deposition temperatures above approximately 210-220 °C, in addition, an intermediate phase is forming between CIGS and In_xS_y, probably a Cu-In-S compound. Also Ga may be involved in small amounts. This intermediate phase may have a detrimental effect on the cell performance, since it changes the junction formation. It is assumed that with further increasing deposition temperature, the intermediate layer becomes broader and continuous, thus further deteriorating the cell performance.

5.2.2 Influence of Na

In order to investigate the influence of Na on the In_2S_3 buffer layer growth, also a solar cell with Al_2O_3 layer between SLG and Mo was produced. Al_2O_3 was shown to impede Na diffusion from the SLG substrate effectively [67]. In addition, reference cells with CdS buffer layer were produced with and without Na. For both, the In_2S_3 and the CdS samples, the solar-cell efficiencies were found to be significantly lower for cells without Na (Table 5.2). The CIGS absorber growth is strongly affected by the Na available in the system, as already reported by several authors [55, 67, 100, 101, 102]. These authors found a decrease in open-circuit voltage and fill factor for cells without Na, which is consistent with the present results shown in Table 5.2.
External QE spectra of CIGS solar cells with CdS and In_2S_3 buffer layers, with and without Na are shown in Fig. 5.8. The QE for solar cells with In_2S_3 buffer layer is significantly higher in the blue wavelength range than for solar cells with CdS

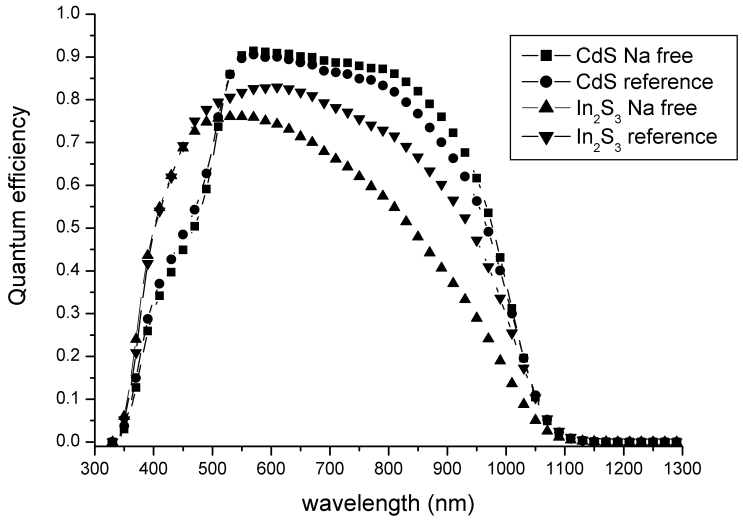

Figure 5.8: External quantum efficiency curves of solar cells with CdS and In_2S_3 buffer layers, with and without Na. The difference between the cells with CdS buffer is not significant, which is consistent with the j_{sc} values (Table 5.2). The difference between the In_2S_3 cells is significant, though, in a broad interval between 500 and 1000 nm.

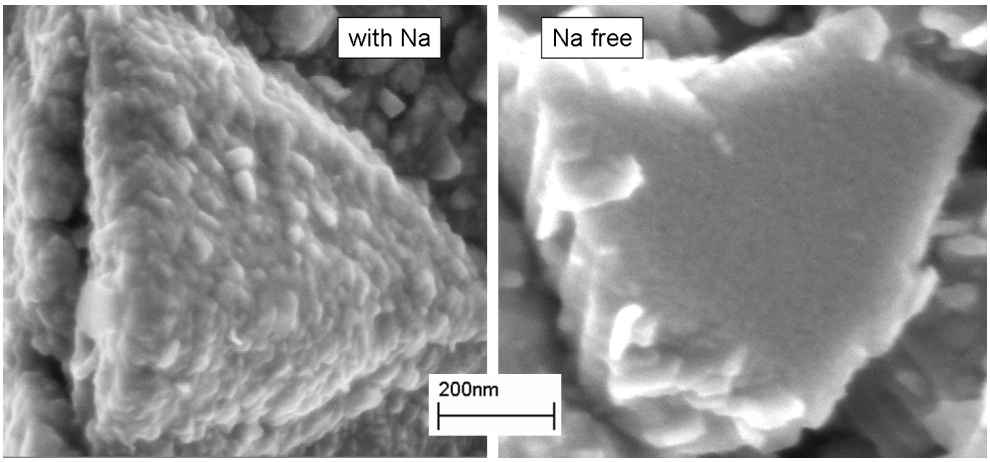

Figure 5.9: Plan-view scanning electron micrographs of small In_2S_3 grains on large CIGS grains. The In_2S_3 grain sizes are significantly larger for cells containing Na.

buffer layer. This is expected owing to the larger band gap energy of In_2S_3 (2.7-2.8 eV) [97], than that of CdS (2.4-2.5 eV) [30]. However, only in the case of In_2S_3 buffer layers, the QE at wavelengths between approximately 500 and 1000 nm is significantly larger for cells containing Na than for Na-free cells. This is consistent with the larger short-circuit current density for cells containing Na (Table 5.2). In the case of CdS buffer layers, the QE of solar cells with and without Na barrier for the interval between 500 and 1000 nm do not differ significantly, which again agrees with the short-circuit current densities of the respective solar cells (Table 5.2) and also with earlier reports [55, 67, 100, 101, 102]. Further measurements are necessary in order to explain the enhanced carrier collection in cells with In_2S_3 buffer layer containing Na. In Fig. 5.8, there is no significant difference between the Na free and Na containing In_2S_3 sample at a wavelength of approximately 370-400 nm (which corresponds qualitatively to the band-gap energy). Maybe, the resolution of the QE measurements is not sufficient to measure the changes in the In_2S_3 band-gap energy due to Na incorporation.
In Fig. 5.9, plan-view SEM images of small ALD-In_2S_3 grains on top of large CIGS grains are shown. The sample without Na consists of much smaller In_2S_3 grains than the sample with Na.

The cross-section BF-TEM image from a Na free sample with an In_2S_3 buffer layer deposited at 210 °C (Fig. 5.10) shows significantly smaller In_2S_3 grain sizes (10-15 nm), than those of the sample containing Na. The layer thickness (about 40 nm) is approximately the same (compare with Fig. 5.2).
No differences are visible in the SAED pattern (Fig. 5.11) and the HR-TEM image (Fig. 5.12): also for the sample without Na, the interface shows the same orientation relationships and good lattice match of In_2S_3 on CIGS (compare with Figs. 5.3 and 5.4). There is also no intermediate phase visible between CIGS and In_xS_y. The linear elemental profiles extracted from the elemental mappings of the Na free CIGS/ALD-In_2S_3 interface are shown in Fig. 5.13. There is a difference between cells with and without Na in the diffusion of Cu and Ga from CIGS into In_xS_y:

Table 5.2: The photovoltaic properties of cells, with CdS and In_2S_3 buffer, with and without Na. The values are averages obtained from three to five cells.

Buffer, with/without Na	η (%)	V_{oc} (mV)	FF (%)	J_{sc} ($\frac{mA}{cm^2}$)
CdS, without Na	7.9 ± 0.2	544 ± 2	58 ± 2	25.2 ± 0.5
CdS, with Na	12.6 ± 0.2	649 ± 1	76 ± 2	25.7 ± 0.4
210 °C In_xS_y, without Na	8.7 ± 0.1	603 ± 7	69 ± 1	20.9 ± 0.5
210 °C In_xS_y, with Na	12.6 ± 0.3	686 ± 3	74 ± 2	24.8 ± 0.3

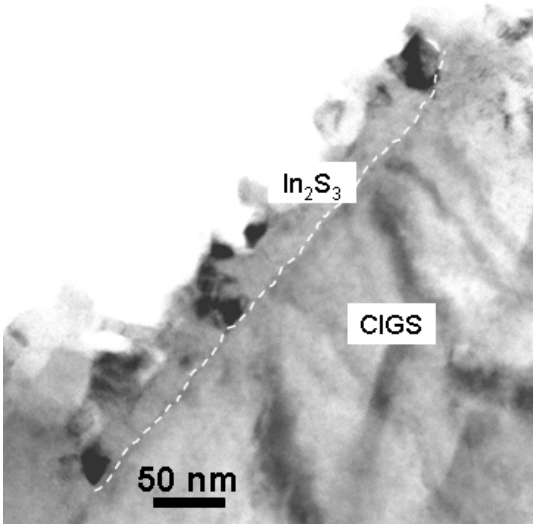

Figure 5.10: Bright-field transmission electron micrographs of the interface between CIGS and In_2S_3 (grown at 210 °C, Na free). Grain sizes are significantly smaller than in the 210 °C sample without Al_2O_3 layer between SLG and Mo (Fig. 5.2).

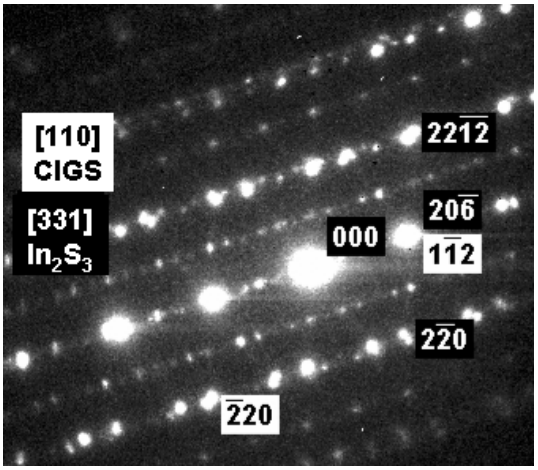

Figure 5.11: Selected-area electron diffraction pattern from the interface between CIGS and In_2S_3 (grown at 210 °C, Na free). There is no difference in comparison with the sample containing Na (Fig. 5.3).

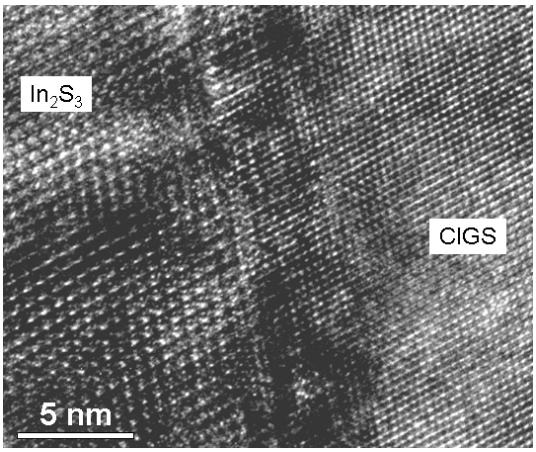

Figure 5.12: High-resolution transmission electron micrograph from the interface between CIGS and In_2S_3 (grown at 210 °C, Na free). There is no difference in comparison with the sample containing Na (Fig. 5.4).

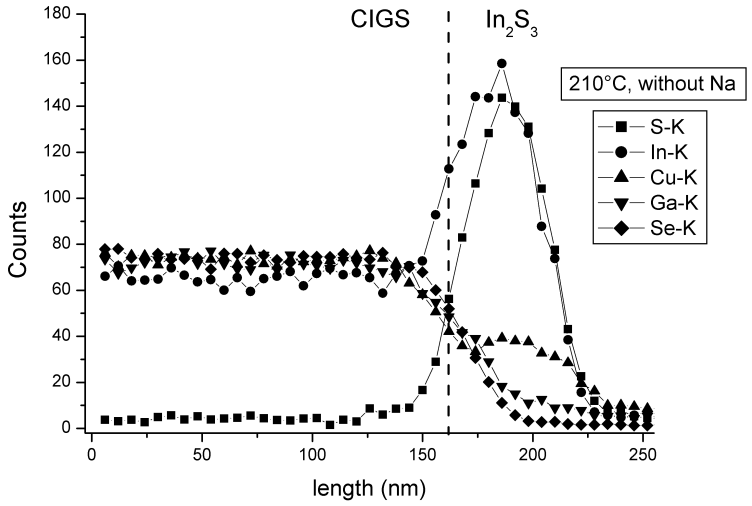

Figure 5.13: Linear elemental distribution profiles across interfaces between CIGS and In_2S_3 (grown at 210 °C, Na free), extracted from EDX elemental mappings. Cu and Ga diffusion from CIGS into In_2S_3 as well as Cu depletion and In enrichment on the CIGS side of the interface are visible.

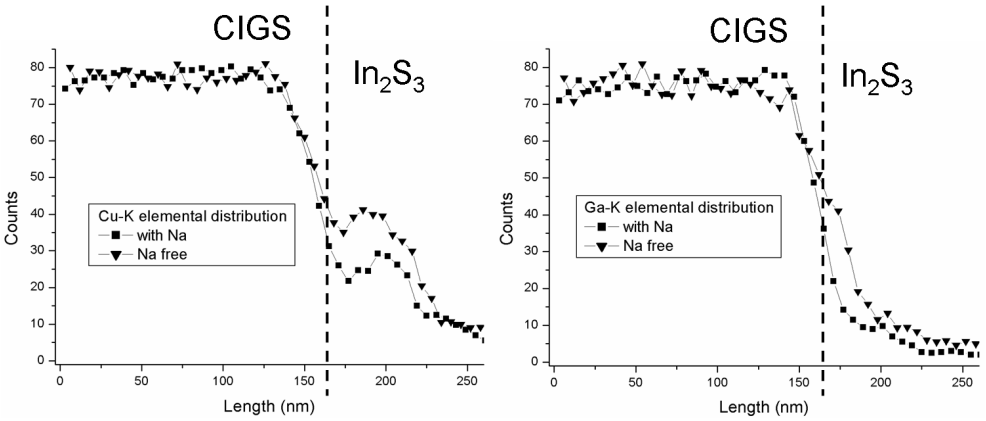

Figure 5.14: Linear elemental distribution profiles across interfaces between CIGS and In_2S_3 (grown at 210 °C). Cu and Ga diffusion from CIGS into In_2S_3 are significantly enhanced in the sample without Na.

Fig. 5.14 shows that the diffusion is clearly enhanced in cells without Na. No difference was detected between the In-K linear elemental distribution profiles.
The present results show that the amount of Cu diffusing from CIGS into In_2S_3 is enhanced in a sample without Na. This implies that Na (if present) may occupy those sites in the In_2S_3 layer, which can also be occupied by Cu atoms. Barreau et al. [103] for PVD-In_2S_3 and Naghavi et al. [95, 104] for ALD-In_2S_3 suggested as well that Na occupies both In sites and vacancies in the In_2S_3 spinel phase.

From the present results, the following interpretation of the effects of Na on the CIGS/ALD-In_2S_3 heterojunction can be drawn. There is an interdiffusion of Cu, Ga and In between CIGS and In_2S_3 during the buffer layer growth (see also results on the temperature dependence, p. 58f). In addition, also Na diffuses into In_2S_3. Na and Cu both occupy In sites and vacancies in the defective In_2S_3 tetragonal spinel structure. Cu-In-S, In-Na-S and Na-S phases might form in case of excessive diffusion. Also Ga-containing compounds may be formed, however, only to a small extent since from the EDX measurements, the Ga concentration appears to be considerably smaller than the Cu concentration. If Na is not available, more Cu can diffuse from CIGS into In_xS_y. Depending on the Cu content, different Cu-In-S phases may be formed, which are n-type (e.g., $CuIn_5S_8$ for low Cu concentrations) or p-type (e.g., $CuInS_2$ for large Cu concentrations). A similar consideration has been published by Barreau et al. [103]. A large Cu concentration in the In_2S_3 layer may deteriorate the n-type conductivity and the optical properties of the In_2S_3 buffer layer, and thus the short-circuit current density of the solar cell.

It is assumed that the diffusion of Cu, Ga and Na into CdS is not as strong as the corresponding diffusion into In_2S_3 (since there is not such a large density of vacancies as in In_2S_3), thus, the charge-carrier concentration of the buffer layer is not largely changed.

5.3 Sputtered In_xS_y layers and their interfaces with $Cu(In,Ga)Se_2$

In this section, photovoltaic parameters of cells with sputtered In_xS_y buffers will be presented, followed by compositional, structural and optical characterization of sputtered In_xS_y layers on Si and Suprasil substrates. At In_xS_y/CIGS interfaces, the effects of the substrate temperature on the In_xS_y/CIGS interface formation was studied.

5.3.1 Photovoltaic properties of the solar cells

The photovoltaic properties of all solar cells studied are summarized in Table 5.3. The efficiencies in dependence of the substrate temperature show a maximum at

Table 5.3: The photovoltaic properties of cells with sputtered In_xS_y buffers deposited at 60, 230 and 340 °C. The values are averages obtained from three cells.

Substrate temperature	η (%)	V_{oc} (mV)	FF (%)	J_{sc} ($\frac{mA}{cm^2}$)
60 °C	6.9 ± 0.6	473 ± 38	55.4 ± 0.4	26.3 ± 0.5
230 °C	11 ± 1	615 ± 41	68 ± 2	26.4 ± 0.3
340 °C	1.9 ± 0.6	412 ± 31	25 ± 7	18 ± 4

Table 5.4: Compositions of sputtered In_xS_y buffers deposited at 60, 230 and 340 °C, as obtained by EDX. Since no standards were used, these values are comparable only relatively. The statistical error for each of these measurements was approximately ± 1 at.%.

Sample	[In] (at.%)	[S] (at.%)
60 °C	49	51
230 °C	49	51
340 °C	44	56

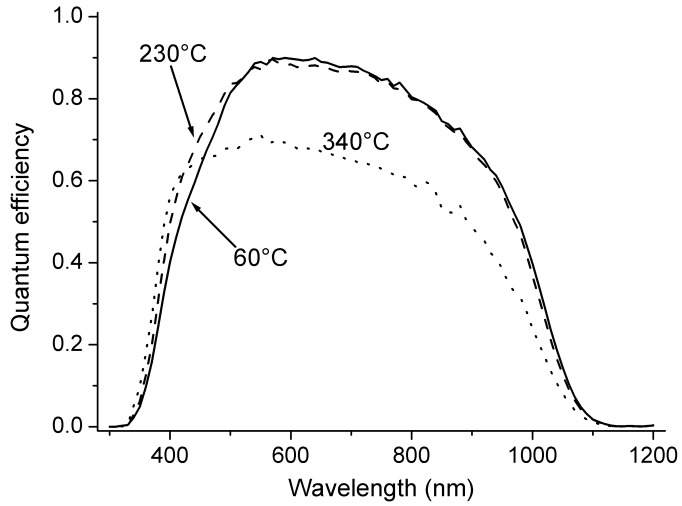

Figure 5.15: External quantum efficiencies of the 60 °C, the 220 °C and the 340 °C samples.

about 230 °C and a very low efficiency for the 340 °C sample (as also revealed by earlier optimization experiments [73]). In addition, the quantum-efficiency curves (Fig. 5.15) indicate a reduced carrier collection for the 340 °C sample, compared with those of the 60 °C and 230 °C samples. These results resemble those for solar cells with In_2S_3 buffer layers deposited by ALD [105, 106]. There, the solar-cell performance improves with increasing substrate temperature, up to a value of about 230 °C; from this temperature on, the efficiencies decrease with increasing substrate temperature.
Since cells with both, sputtered In_xS_y and ALD-In_2S_3 buffer layers show very similar properties, in the present section, the structural and chemical properties of sputtered In_xS_y layers and their interfaces to CIGS absorbers will now be compared with corresponding results obtained from ALD-In_2S_3 samples (see previous section).

5.3.2 Studies of sputtered In_xS_y layers

In order to determine the composition of In_xS_y films deposited at various temperatures, In_xS_y layers were sputtered on Si substrates at 60 °C, 230 °C and 340 °C and then studied by means of EDX. These temperatures are similar to the deposition temperatures of the In_xS_y layers on CIGS/Mo/SLG stacks studied by means of plan-view SEM and cross-section TEM (pp. 74ff). As shown by Table 5.4, the S concentration in the In_xS_y layers increases with increasing substrate temperature. It has to be pointed out that these values are comparable only on a relative basis,

because no standards were used for the EDX measurements. Since the partial pressure of sulfur increases with increasing temperature, it is probable that the reactivity of sulfur also increases, and that for this reason, the sulfur concentration in the film deposited is higher at elevated temperatures. Thus, it may be that the 60 and 230 °C layers rather consist of InS, whereas the 340 °C sample exhibits mainly an In_2S_3 stoichiometry.

The XRD patterns shown in Fig. 5.16 were acquired on those In_xS_y layers measured by EDX. The use of Si as substrate material provided a possibility to calibrate in-

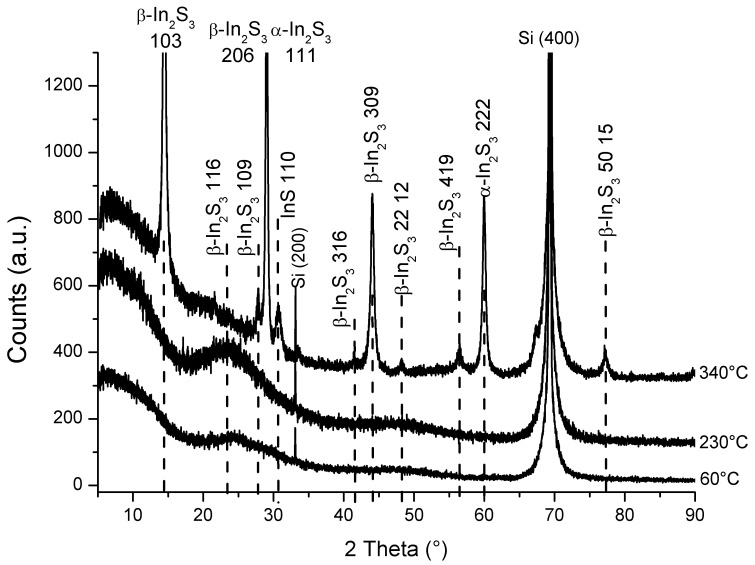

Figure 5.16: X-ray diffraction patterns of sputtered In_xS_y layers deposited at 60, 230 and 340 °C.

tensities and angles. For the 60 °C and the 230 °C layers, the XRD patterns show broad peaks, which may be related to atomic planes of the tetragonal β-In_2S_3, but also to those of the orthorhombic InS crystal structure. These broad peaks indicate very small grains of the In_xS_y layers. In contrast, the XRD pattern of the 340 °C layer shows various narrow peaks, which can be related to tetragonal β-In_2S_3 [107], cubic α-In_2S_3 [98]), and orthorhombic InS [108].
The β-In_2S_3 and α-In_2S_3 phases exhibit preferred growth along [103] and [111] directions. According to the In-S phase diagram [72], the cubic α-In_2S_3 phase forms at temperatures between about 414 °C and 750 °C, whereas β-In_2S_3 is the low-temperature phase. The β-In_2S_3 structure is reported to be of spinel-type with statistically distributed In vacancies on tetrahedral interstices of the S sublattice [72, 98]. The presence of the InS phase can be traced back to a partial S loss during the sputtering process.

Naturally, preferential orientations and crystal structures of In_xS_y layers on Si can not directly be compared with those on CIGS substrates. However, the more pronounced peaks for elevated substrate temperatures (shown in Fig. 5.16) can be explained by a higher surface energy for the sputtered In_xS_y, resulting in more perfect crystallization. These results obtained by XRD will be compared with optical, SEM and TEM measurements further below.

Transmission and reflectance measurements were performed on In_xS_y films on Suprasil substrates deposited in the same run as the In_xS_y layers on Si substrates (measured by EDX and XRD). The absorption coefficients in dependence of the wavelength were estimated using the relationship

$$\alpha(\lambda) = -\frac{1}{d} \ln\left(\frac{T(\lambda)}{1 - R(\lambda)}\right) \tag{5.2}$$

which can be derived from Lambeer-Beer's Law

$$I = I_0 \exp\left(-\alpha\, d\right) \tag{5.3}$$

by putting $I := T$ and $I_0 := (1 - R)$, neglecting reflections at the substrate/In_xS_y interfaces. Here, α is the absorption coefficient and λ the wavelength of the incident radiation, d the thickness of the In_xS_y film, T the transmission, R the reflectance, I the measured intensity after transmission and I_0 the intensity prior to the transmission.
Furthermore, according to Pankove et al. [109], the following relationship is valid for semiconductors with direct or indirect band gap:

$$\alpha(E) = A\, \frac{(E - E_\mathrm{g})^m}{E} \tag{5.4}$$

where E is the energy of the transmitted light, A and m are constants and E_g is the band-gap energy. The value of the constant m depends on whether the optical transition is a direct (m=0.5) or an indirect (m=2) one.
But which value of m is the most appropriate one for these In_xS_y layers studied? In the literature, various authors found In_2S_3 thin films to show direct [59, 110, 111, 112] as well as indirect [60, 113] optical transitions (the transition type does not depend on the deposition technique). The scarce results on optical measurements of InS suggest an indirect optical transition [114]. It seems as if both, direct and indirect optical transitions, can be found in In_xS_y thin-films, but the nature of these transitions can not be unambiguously revealed.

For the present results, the absorption coefficients of all In_xS_y layers were well described by the model for an indirect band gap (m=2). The E_g values for the

three In_xS_y layers were graphically estimated from plots of $(\alpha E)^{1/2}$ in dependence of E, according to eq. 5.4. These graphs are shown in Fig. 5.17. The extracted values of E_g for the 60 °C, 230 °C and 340 °C In_xS_y layers were 1.9 eV, 2.0 eV and

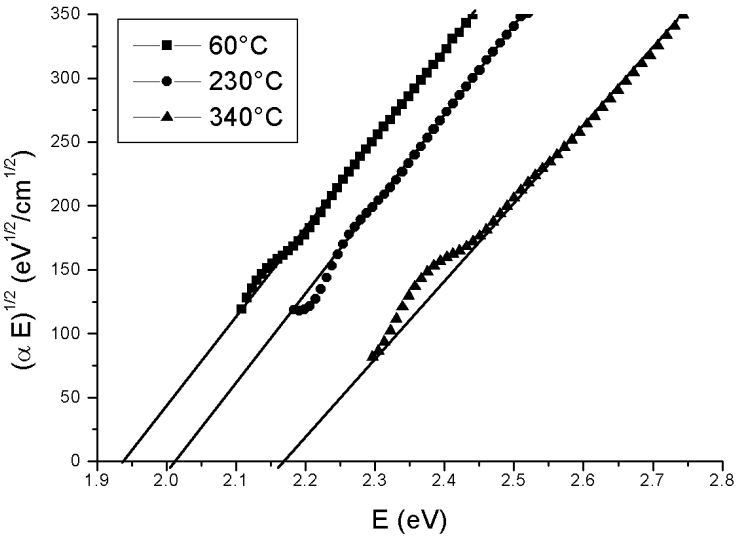

Figure 5.17: Plots of $(\alpha E)^{1/2}$ in dependence of the photon energy E for the 60 °C, 230 °C and 340 °C samples, assuming m=2 in equation 5.4. From these plots, E_g can be estimated with an uncertainty of about ± 0.05 eV.

2.2 eV (with an error of about ± 0.05 eV). In case of a direct transition model (m=0.5), these values would give 2.3 eV, 2.4 eV and 2.6 eV. Apparently, the band-gap energy increases with increasing substrate temperature. This behavior may be related to the change in the crystal structure indicated by the XRD measurements. Also, Kim et al. [113] found the band-gap energy of In_2S_3 layers to increase with increasing sulfur concentration. The same behavior was revealed for the sputtered In_xS_y layers studied here (Table 5.4), probably also due to the changes in the crystal structure.

The differences in grain sizes indicated by the XRD patterns are confirmed by the plan-view SEM images of the In_xS_y/CIGS/Mo/SLG samples (Fig. 5.18). Small In_xS_y grains are visible on large CIGS grains. For the 340 °C sample, In_xS_y grain sizes of about 20-80 nm were found, whereas for the 60 °C (not shown here) and the 230 °C samples, the In_xS_y grains were too small to be resolved in the SEM image.

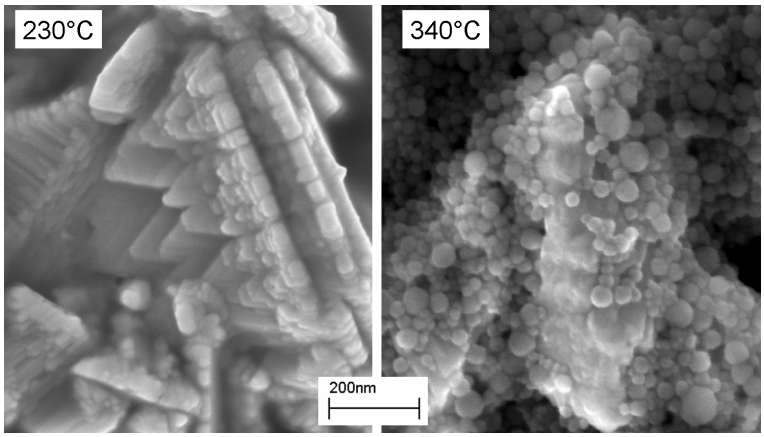

Figure 5.18: Plan-view scanning electron micrographs of In_xS_y/CIGS/Mo/SLG stacks deposited at 230 °C and 340 °C. For 340 °C, In_xS_y grain sizes were about 20-80 nm, whereas for 60 °C (not shown here) and the 230 °C, the In_xS_y grains were too small to be resolved.

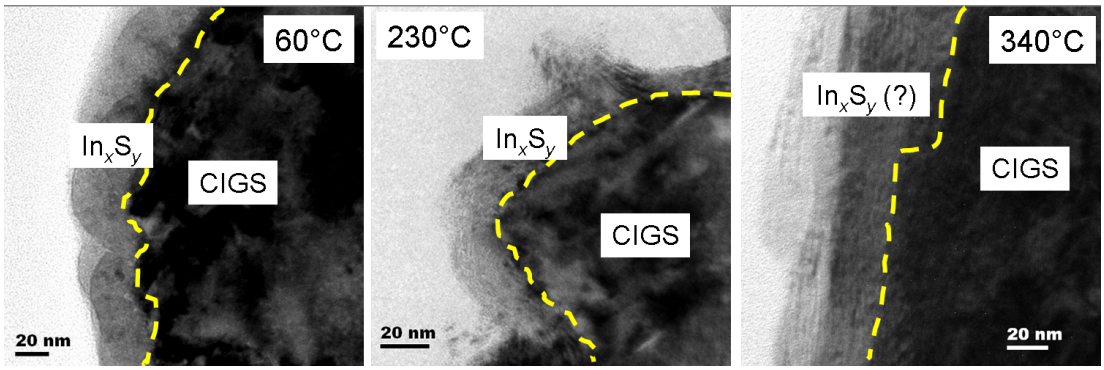

Figure 5.19: Bright-field transmission electron micrographs of the interfaces of CIGS with In_xS_y layers grown at 60, 230 and 340 °C. All three samples show inhomogeneous In_xS_y layer thicknesses, varying between 25 and 100 nm. For the 340 °C sample, a layered structure is found in the buffer.

5.3.3 Studies of In_xS_y/CIGS interfaces

As revealed by the BF-TEM images in Fig. 5.19, the In_xS_y layers of the samples investigated all seem to cover the CIGS contiguously. However, all three samples show inhomogeneous In_xS_y layer thicknesses, varying between 25 and 100 nm. For the 340 °C sample, a layered structure is found in the buffer (Fig. 5.19). This structure is formed by a high density of planar defects in the buffer layer, directly at the interface to CIGS, as shown by the HR-TEM image in Fig. 5.20. The interplanar distances in this buffer do not correspond to the crystal structures of any In_xS_y phase, thus, a question mark was added behind the notation "In_xS_y". Such a defect-containing layer was also found at an interface between ALD-In_2S_3 deposited at 240 °C and CIGS (see previous section), however, appearing only

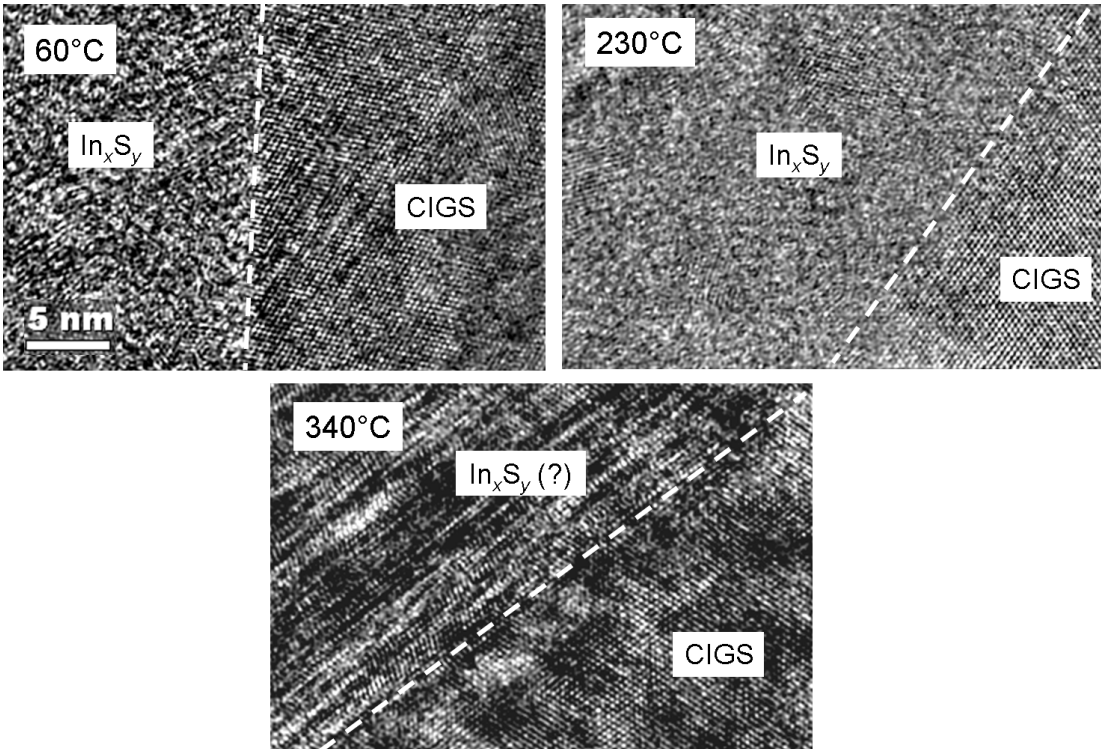

Figure 5.20: High-resolution transmission electron micrographs of the interfaces of CIGS with In_xS_y layers grown at 60, 230 and 340 °C. A high density of planar defects are visible in the buffer layer of 340 °C sample, directly at the interface to CIGS.

as intermediate layer between the tetragonal CIGS and β-In_2S_3 structures. For further details on these interfacial phases forming at sputtered In_2S_3/CIGS and ALD-In_2S_3/CIGS interfaces, please refer to chapter 6.

For the 60 °C and the 230 °C samples, such defects were not found in the buffer

layers (Fig. 5.20). In contrast to the 340 °C sample, very small grain sizes of about 5 nm can be estimated from the HR-TEM images of the 60 °C and 230 °C samples (Fig. 5.20). This result was already suggested by the XRD and SEM measurements (Figs. 5.16 and 5.18). While the In_xS_y/CIGS interfaces of the 60

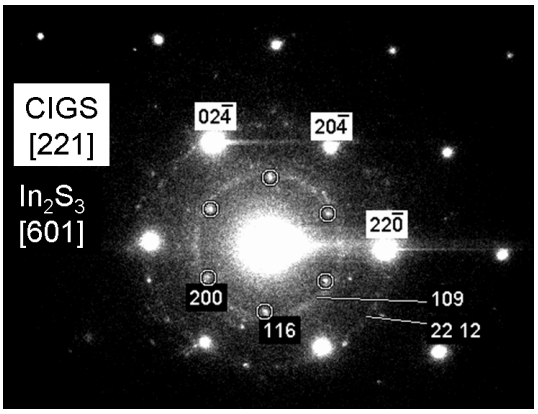

Figure 5.21: Selected-area electron diffraction pattern from the interface of CIGS with an In_xS_y layer grown at 230 °C. A tetragonal β-In_2S_3 crystal structure is revealed for this sample.

°C and the 340 °C samples appear abrupt, the according interface of the 230 °C sample seems to be rather diffuse. By means of SAED acquired on the In_xS_y/CIGS interfaces (Fig. 5.21), a tetragonal β-In_2S_3 crystal structure was revealed for the 230 °C sample (the pattern of the 60 °C sample, not shown here, is very similar to that of the 230 °C sample).

Linear elemental distribution profiles, extracted from EDX elemental mappings on CIGS/In_xS_y interfaces, are shown in Fig. 5.22 for the 60 °C, 230 °C and 340 °C samples. The dashed lines indicate the positions of the CIGS/buffer interfaces, given by the crossover of the Se and the S signals; these two elements did not show any significant change in any of the samples investigated, thus Se and S are considered to interdiffuse only to a negligible extent. For the 60 °C and the 230 °C samples, the linear profiles reveal a Cu and a Ga diffusion from CIGS into In_xS_y. On the In_xS_y side of the CIGS/In_xS_y interfaces, the Cu and Ga signals decrease much more gradually than the Se signal. The extent of their diffusion increases with increasing deposition temperature. In addition to the Cu and Ga diffusion, an obvious depletion of Cu and an enrichment of In are visible on the CIGS side of the interface, especially in the case of the 230 °C sample. Apparently, depletion and enrichment of the elements are also enhanced with increasing deposition temperature of the In_xS_y layer. A similar result has been obtained at ALD-In_2S_3/CIGS interfaces (see previous section 5.2.1).

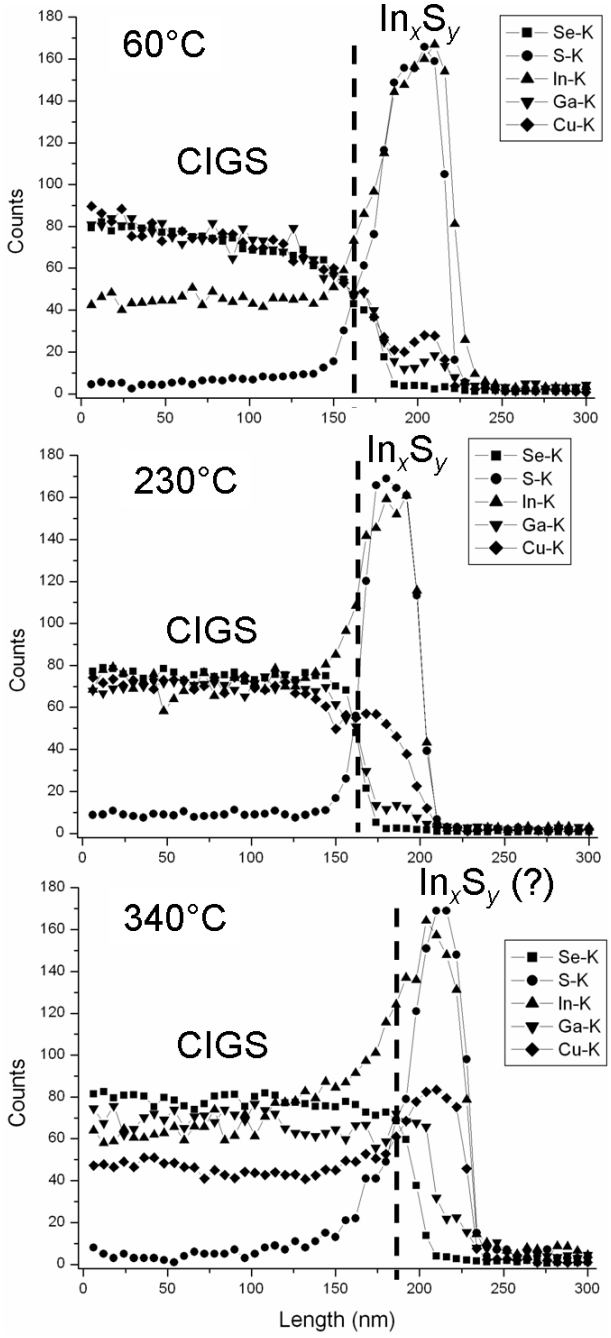

Figure 5.22: Linear elemental distribution profiles, extracted from EDX elemental mappings on In_xS_y/CIGS interfaces. Cu and Ga diffusion from CIGS into $In_xS_y$and Cu depletion on the CIGS side of the interface are revealed. Only for the 340 °C sample, also enhanced In enrichment on the CIGS side of the interface was found. All effects increase with increasing In_xS_y deposition temperature.

Assuming a Cu:In ratio of 1 on the (not depleted) CIGS side of the interface and a In:S ratio of 2:3 on the buffer side of the interface, the Cu concentration in the buffer can be estimated to about 7 at.% for the 60 °C and to about 13 at.% for the 230 °C sample, neglecting Ga diffusion. For the 340 °C sample, a much larger Cu depletion than for the 60 °C and 230 °C samples was found (Fig. 5.22). Unfortunately, it is not clear how thick the Cu-depleted layer on the CIGS side of the interface is. Apparently, the width of this depleted layer is larger than about 200 nm.
It has to be taken into account that Cu may not only diffuse from CIGS into the buffer layer; in addition, Cu may also diffuse from the CIGS side of the CIGS/buffer interface to the Mo back contact. This conclusion is supported by the fact that the number of depleted Cu atoms on the CIGS side of the interface (as far as can be estimated from Fig. 5.22) is much larger than the number of Cu atoms diffused into the buffer layer. It is also remarkable that for the 340 °C sample, the Cu concentration in the buffer layer seems to be larger than on the CIGS side of the interface (Fig. 5.22). Probably, such a strong Cu diffusion is not only driven by the substrate temperature; furthermore, also gradients of chemical potentials or strains indicated by the planar defects shown by Fig. 5.20 are possible causes.
Local maxima of the Cu-K linear elemental distribution profiles inside the In_2S_3 layer are visible in all samples studied (Fig. 5.22). These maxima are again not artifacts of the measurements, but can be interpreted in a similar way as the local maxima of the ALD-In_2S_3 samples (see previous section).

From the present results, the following interpretation of sputtered In_xS_y/CIGS interfaces with respect to the In_xS_y deposition temperature was developed. With increasing deposition temperature, Cu, Ga, and In interdiffusion becomes more enhanced, which leads to a Cu-depleted and In-enriched near-interface region of CIGS. There, an inversion from *p*-type to *n*-type is probable. This region becomes broader with increasing deposition temperature, which seems to have a beneficial effect on the junction formation. Thus, the cell performance improves up to temperatures of about 230 °C. This behavior is similar to that assumed for ALD-In_2S_3/CIGS interfaces.
The considerable deterioration of the solar-cell performance for the 340 °C sample compared with the 230 °C sample can be related to the formation of $CuIn_5S_8$. Please refer to chapter 6 for details.

5.4 Interfaces between In_xS_y evaporated from In_2S_3 powder and Cu(In,Ga)Se_2

The CIGS solar cells with In_xS_y buffers evaporated from In_2S_3 powder were air-annealed at a temperature of 200 °C and for durations ranging from 15 to 50 min. Prior to and after the air-annealing step, the completed solar cells were analyzed by current-voltage (j-V) characterizations under standard AM1.5 illumination test conditions.
At these In_xS_y/CIGS interfaces, the influence of air-annealing at 200 °C for several minutes was studied.

Photovoltaic parameters of the cells investigated are summarized in Table 5.5. For the two cells with In_xS_y layers deposited at 23 °C, air-annealing at 200 °C for 15 min increased the efficiency significantly, from 7.7 to 11.8 %. These two

Table 5.5: The photovoltaic properties of the cells investigated.

Sample	η (%)	V_{oc} (mV)	j_{sc} ($\frac{mA}{cm^2}$)	FF (%)	buffer thickness (nm)	annealing time (min)
23 °C, as-grown	7.7	420	28.0	65	70	
23 °C, annealed	11.8	593	28.9	69	70	15
200 °C, as-grown	6.1	605	20.7	48	30	
200 °C, annealed	3.7	309	26.4	46	90	50
300 °C, annealed	0.01	20	1.4	27	70	30

samples consist of identical CIGS substrates produced in the same run; therefore, the influence of air-annealing on the In_xS_y/CIGS interface could be directly studied. The effect of annealing may be attributed to the reduction of the number of anion defects, i.e., the occupation of Se or S vacancies by oxygen [115]. Change of the pinning position of the Fermi level at the heterojunction interface significantly affects junction properties and hence the photovoltaic parameters.
The two cells with In_xS_y layers deposited at 200 °C substrate temperature are not directly comparable, since the CIGS and Mo layers of these cells were deposited in different runs, and the buffer layers show different thicknesses (Table 5.5). These cells were analyzed to image features of the CIGS/In_xS_y interface and measure effects of annealing also at elevated substrate temperatures higher than 23°C. The solar cell with an In_xS_y buffer layer deposited at a substrate temperature of 300 °C showed an efficiency of practically 0 %. Air-annealing of this cell for 30 min did not change this value.

For all solar cells investigated, continuous In_xS_y layers and good coverage of the CIGS layer was found. The grain sizes of the In_xS_y layers are very small, approximately 5-15 nm, depending on the In_xS_y layer thicknesses and substrate temperatures.
BF-TEM images of the 23 °C In_xS_y layers in the as-grown (a) and annealed (b) state and their interfaces with CIGS and ZnO are shown in Fig. 5.23. The In_xS_y layers are about 70 nm thick. For the annealed sample, on the In_xS_y side of the

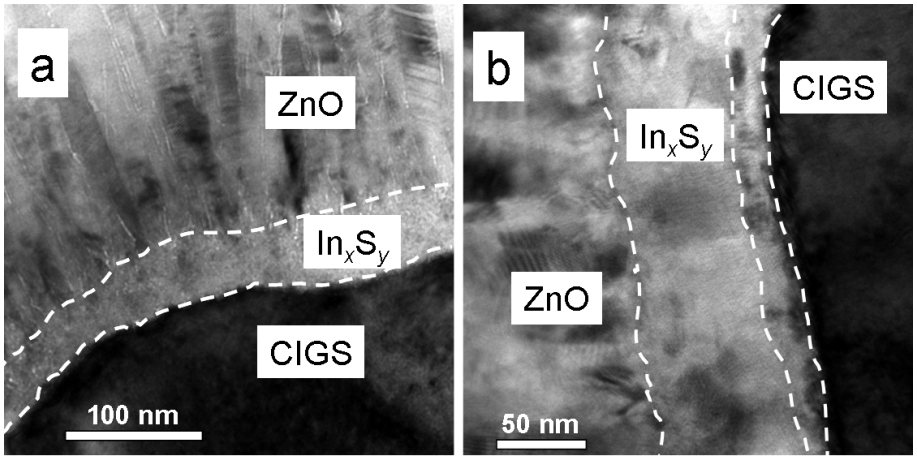

Figure 5.23: Bright-field transmission electron micrographs of (a) as-grown and (b) air-annealed (200 °C, 15 min) ZnO/In_xS_y/CIGS interfaces. These In_xS_y layers were deposited at 23 °C. For the air-annealed sample, an interfacial layer is found (indicated by dashed lines).

CIGS/In_xS_y interface, an interfacial layer appears (indicated by dashed lines).
This interfacial layer is also visible in the HR-TEM image of the interface between CIGS and 23 °C In_xS_y of the annealed solar cell (Fig. 5.24). However, it was not possible to determine the structure of this interfacial layer by SAED, since it was too thin (approximately 10-20 nm), and thus the excitation volume was too small.

It was also impossible to determine the crystallographic structures of the as-grown and annealed In_xS_y layers by SAED; the reflections and diffraction rings of the SAED pattern (not shown) can be related to tetragonal In_2S_3 [98], orthorhombic InS, and monoclinic In_6S_7 [108]. This is an indication that the powder-evaporated In_xS_y layers may consist of several indium sulfide compounds. Based on measurements of interplanar distances of the resolved lattices in Fig. 5.24, possible In_xS_y phases are In_2S_3, InS, and In_6S_7 as well. No orientation relationship can be identified between the {112) planes of the tetragonal CIGS and planes of the In_xS_y layer. A possible mixture of several indium sulfide compounds was also found for In_xS_y

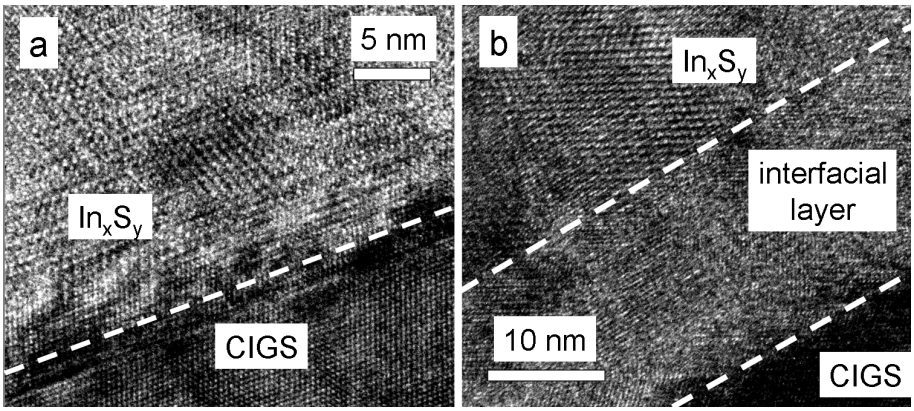

Figure 5.24: High-resolution transmission electron micrographs of (a) as-grown and (b) air-annealed (200 °C, 15 min) In_xS_y/CIGS interfaces. These In_xS_y layers were deposited at 23 °C. As in the bright-field transmission electron micrograph in Fig. 5.23b, an interfacial layer can be identified.

buffer layers deposited at 200 °C (see Fig. 5.25 for a typical HR-TEM image of these layers). This air-annealed solar cell showed an efficiency of 3.7 %. Planar

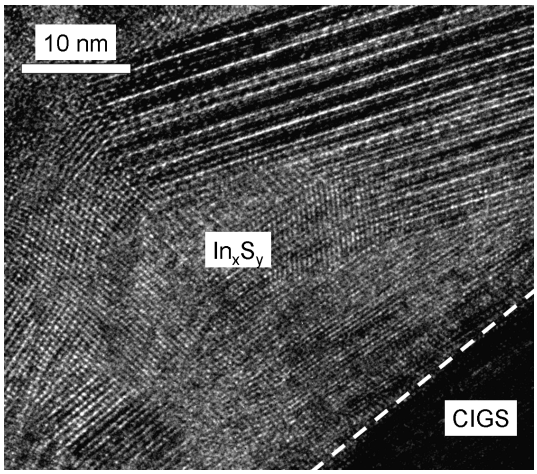

Figure 5.25: High-resolution transmission electron micrograph of an In_xS_y layer deposited at 200 °C (annealed at 200 °C for 50 min). The planar defects visible in this micrograph may be related to twinning in InS crystals.

defects (e.g., twins), such as those visible in Fig. 5.25, have been reported by Fitzgerald et al. [116] for InS crystals. Interplanar distances of the resolved lattices may again be related to In_2S_3, InS, and In_6S_7.
However, for one solar cell with an In_xS_y buffer layer deposited at 200 °C (as-grown), a homogeneous In_2S_3 phase and a tetragonal crystal structure were found

(Fig. 5.26). The CIGS grain shown is oriented in [110], the In_2S_3 grain in [331] direction. There is a clear orientation relationship between the {112) planes of the

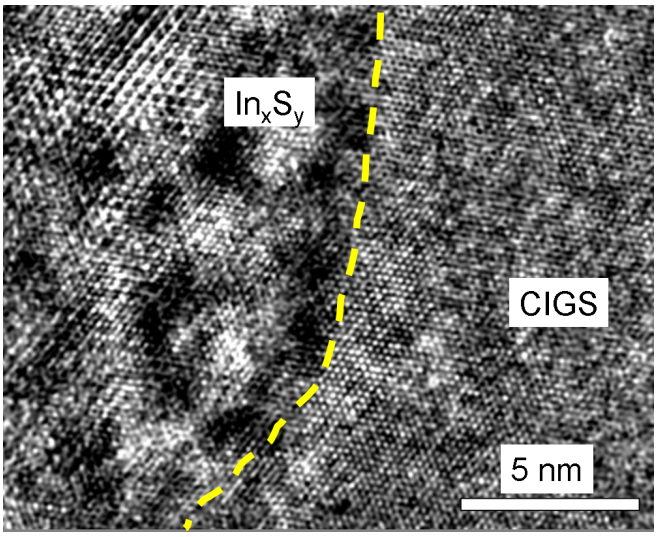

Figure 5.26: High-resolution transmission electron micrograph of an interface between CIGS and an In_xS_y layer deposited at 200 °C (as-grown). In contrast to Fig. 5.25, for the In_xS_y layer, a homogeneous In_2S_3 phase with a tetragonal crystal structure was found.

tetragonal CIGS and {103) planes of the In_2S_3 layer, a result that is found also at 210 °C-ALD-In_2S_3/CIGS interfaces (section 5.2.1 on ALD-In_2S_3 buffers, p. 58). Probably, the S-loss in the In_2S_3 powder during the evaporation and thus the In/S ratio of different In_xS_y layers varies considerably, leading to a variation in the In_xS_y composition and crystal structure.

Elemental distribution profiles of the as-grown (a) and annealed (b) CIGS/23 °C-In_xS_y interfaces are shown in Fig. 5.27. The Ga-K and the O-K signals were omitted since they do not show any significant difference from the Se-K and the Zn-K signals. The positions of the ZnO/In_xS_y and In_xS_y/CIGS interfaces (dashed lines) are given by the crossovers of the Zn and S as well as the S and Se signals. Zn and S as well as S and Se profiles did not show any significant change in any of the samples, thus they are considered to interdiffuse only to a negligible extent. The elemental distribution profiles (Fig. 5.27) reveal a substantial Cu diffusion from CIGS into In_xS_y. Such a diffusion behavior (with various amounts of diffusing Cu) has also been reported for interfaces between co-evaporated In_xS_y and CIGS [117], and for ALD-In_2S_3/CIGS interfaces (Ref. [95] and section 5.2.1 on ALD-In_2S_3 buffers). It is remarkable that already for a substrate temperature of 23 °C, a considerable amount of Cu diffuses from CIGS into In_xS_y. Assuming a Cu concentration of 25 at.% on the CIGS side of the interface and an InS stoi-

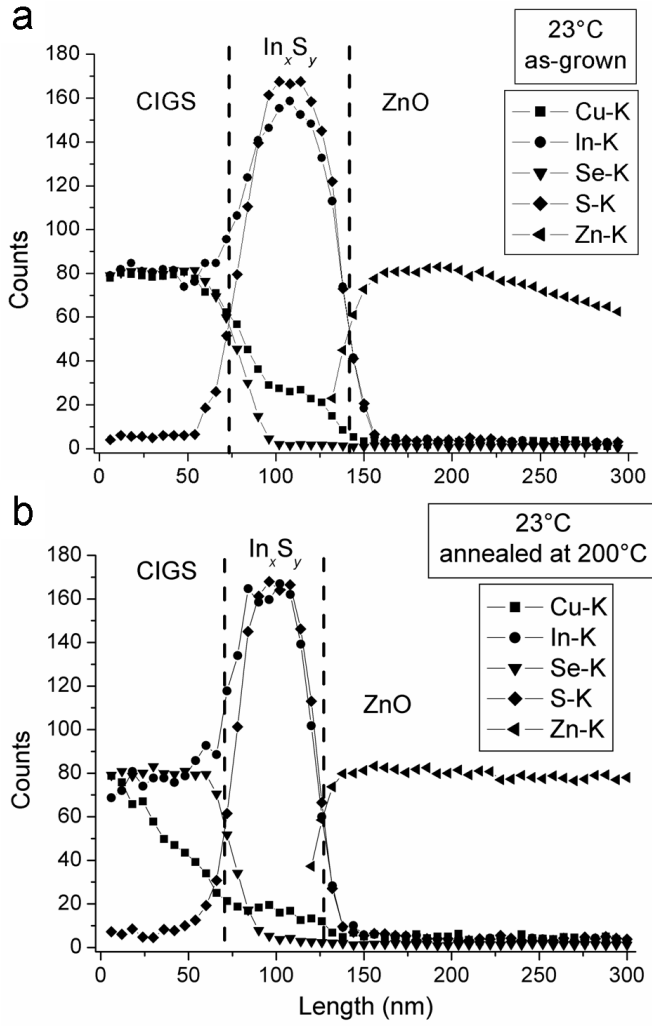

Figure 5.27: Elemental distribution profiles across (a) as-grown and (b) air-annealed (200 °C, 15 min) ZnO/In_xS_y/CIGS interfaces. These In_xS_y layers were deposited at 23 °C. The air-annealed sample shows a significant Cu depletion on the CIGS side of the interface.

chiometry, the Cu concentration in the In_xS_y layer can be estimated to be about 8 at.%. Probably, this Cu diffusion is not driven by temperature, but induced by a gradient of the chemical potential between the CIGS and the In_xS_y layers.
It is known that tetragonal In_2S_3 has a spinel-type crystal structure and contains a large density of vacancies which may be occupied by diffusing Cu atoms. Apart from vacancies, Cu may also replace In on the In sites in In_2S_3 [99].
Based on studies of phase changes by electron microscopy, Fitzgerald et al. [116] suggested that crystals of InS and In_6S_7 may often be non-stoichiometric; probably, these crystals tend to be sulfur-rich. Nishino et al. [114] also mentioned point defects in InS. Thus, other In_xS_y phases apart from In_2S_3 probably also allow for extensive Cu diffusion owing to their crystal structures.

Compared with the as-grown 23 °C sample (Fig. 5.27a), the 23 °C sample air-annealed at 200 °C for 15 min shows a significant Cu depletion on the CIGS side of the interface (Fig. 5.27b). Here, the Cu depletion is assumed to be induced by air-annealing; therefore, the Cu distribution profile is different from that shown in Fig. 5.27a. Also, the concentration of Cu in In_xS_y seems to be larger for the as-grown 23 °C sample (Fig. 5.27a) than for the 23 °C sample air-annealed at 200 °C (Fig. 5.27b). Apparently, Cu may not only diffuse from CIGS into In_xS_y but also from the near interface region in the CIGS layer to the CIGS/Mo interface, including some of the Cu already diffused into In_xS_y during the In_xS_y growth.
Since the BF-TEM and HR-TEM images in Figs. 5.23b and 5.24b indicate an interfacial layer between CIGS and In_xS_y, it is assumed that a Cu-depleted layer was formed, similar to the one postulated by Schmid et al. [79]. Probably, air-annealing induces the formation of a compositionally graded interface between the buffer and CIGS, improving the photovoltaic performance of the solar cell.
Copious Cu diffusion from CIGS into In_xS_y and a significant Cu depletion on the CIGS side of the interface were also found for the sample with an In_xS_y buffer deposited at 200 °C, air-annealed at 200 °C for 50 min (Fig. 5.28). These results reveal Cu distribution profiles across the In_xS_y/CIGS interface similar to those shown in Fig. 5.27b and thus, the effect of annealing is also present after deposition at an elevated substrate temperature.

5.5 Conclusions

Structural and chemical properties of interfaces between CIGS and In_xS_y layers deposited by ALD, sputtering and powder-evaporation were investigated by means of BF-TEM, HR-TEM, SAED, and EDX.

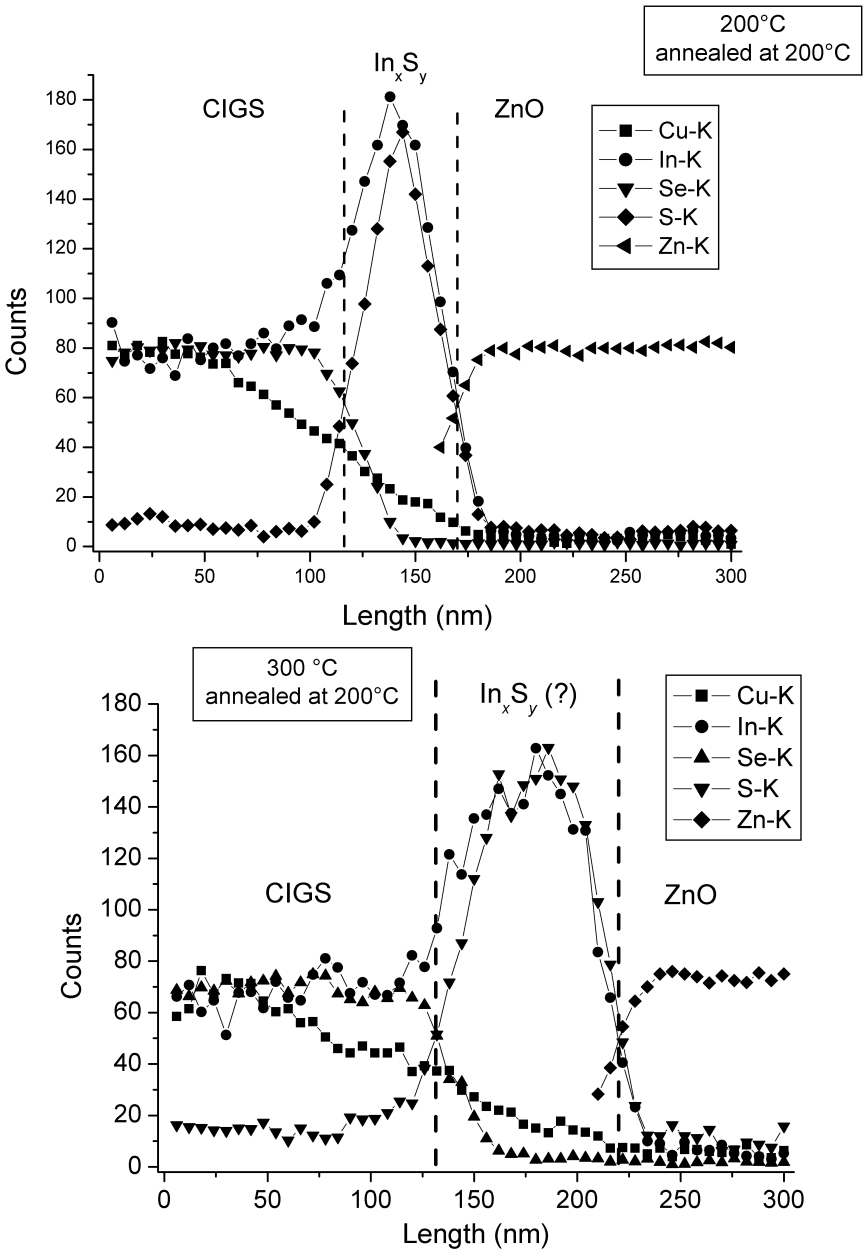

Figure 5.28: Elemental distribution profiles across ZnO/In_xS_y/CIGS interfaces. The In_xS_y layers were deposited at 200 and 300 °C, and the cells were air-annealed at 200 °C for 50 and 30 min. For both samples, again, a significant Cu depletion on the CIGS side of the interface is revealed.

Influence of Na on the interface formation between ALD-In_2S_3 and CIGS

QE spectra revealed smaller carrier collection and short-circuit current densities for Na free cells. No microstructural differences for cells with and without Na were found. However, there is a significant difference in the interdiffusion between CIGS and In_2S_3. Cu and Ga diffusion from CIGS into In_2S_3 are clearly enhanced in the Na free solar cells. These results indicate that both Cu and Na diffuse into the In_2S_3 layer, occupying In sites and vacancies. Probably, the enhanced Cu diffusion from CIGS into In_2S_3 for Na free solar cells deteriorates the electrical and optical properties of the CIGS/In_2S_3 interface and the In_2S_3 buffer layer, which lowers the overall performance of the solar cells.

Temperature dependence of the interface formation between In_xS_y and CIGS

For ALD-In_2S_3 and sputtered In_xS_y samples, the best cell efficiencies were obtained for a deposition temperature of about 210-230 °C. At these temperatures, orientation relationships between atomic planes of CIGS and In_xS_y indicate reduced strains at these In_xS_y/CIGS interfaces and therefore probably also reduced recombination. Results from EDX measurements suggest interdiffusion of Cu, Ga and In across In_xS_y/CIGS interfaces of the ALD-In_2S_3 and sputtered In_xS_y samples. Cu depletion and In enrichment are visible on the CIGS side of these interfaces, and these effects seem to be enhanced with increasing substrate temperature. Local maxima of the Cu signal on the In_xS_y side are induced probably not only by the substrate temperature but mainly by gradients of chemical potentials at ALD and sputtered In_xS_y/CIGS interfaces.
The Cu depletion and In enrichment may indicate the presence of a Cu-depleted (In-rich) Cu-(In,Ga)-Se_2 layer on the CIGS side of the interface. A similar Cu-depleted layer, also referred to as *ordered-defect chalcopyrite* layer, has been postulated by Schmid et al. [79] for CBD-CdS buffered CIGS cells. The presence of such a layer at the In_xS_y/CIGS interfaces of ALD-In_2S_3 and sputtered In_xS_y samples suggests a buried *p*-*n* junction in the CIGS absorber, which may considerably improve the band alignment between CIGS and In_xS_y and thus the solar-cell performance. Probably, the width of this Cu-depleted layer increases with increasing temperature, as the Cu depletion and In enrichment are more enhanced at elevated temperature. This may explain why the efficiencies for both, ALD-In_2S_3 and sputtered In_xS_y samples, increase with increasing deposition temperature until about 210-230 °C. Reasons for the deteriorated solar-cell performance at temperatures above about 250 °C will be given in chapter 6.

In contrast to the ALD-In_2S_3 and sputtered In_xS_y samples, for solar cells with powder-evaporated In_xS_y buffers, the highest efficiencies have been achieved at room temperature. It has to be taken into account that both, the ALD-In_2S_3 and sputtered In_xS_y samples, were produced by the ZSW on Würth Solar CIGS absorbers, whereas the powder-evaporated samples were provided by the IPE. Thus, it is possible that varying compositional properties of these different CIGS absorbers affect the *p*-*n* junction formation between In_xS_y and CIGS considerably, which may at least partly explain these different optimum deposition temperatures.

Similarly as for the ALD-In_2S_3 and sputtered In_xS_y samples, also for the powder-evaporated In_xS_y samples, extended Cu diffusion from CIGS into In_xS_y was found. This is also the case for the as-grown 23 °C sample where such extended Cu diffusion seems to be unlikely owing to the low substrate temperature (this is the case even considering an effectively higher substrate temperature of about 60 °C due to influences from the In_2S_3 source in the vacuum chamber). Apparently, this Cu diffusion is not driven mainly by temperature, but induced by a gradient of the chemical potential between CIGS and In_xS_y. It seems as if, owing to the large number of vacancies in In_xS_y, a substantial amount of Cu always diffuses from CIGS into In_xS_y during the In_xS_y deposition process, independent of the deposition temperature or the deposition technique.

Influence of air-annealing on powder-evaporated In_xS_y/CIGS interfaces

For complete solar-cells with powder-evaporated In_xS_y buffers deposited at substrate temperatures of 23 °C, 200 °C and 300 °, air-annealing at 200 °C for several minutes leads to a strong Cu diffusion from CIGS into In_xS_y and a significant Cu depletion on the CIGS side of the interface. Air-annealing may reduce the number of anion defects and induces the formation of a compositionally graded In_xS_y/CIGS interface. Similarly to ALD-In_2S_3 and sputtered In_xS_y samples, a Cu-depleted and In-rich Cu-(In,Ga)-Se layer on the CIGS side of the interface may form, induced by the air-annealing, improving the band alignment between CIGS and In_xS_y and thus the solar-cell performance.

Chapter 6

Interfacial phase formation between In_xS_y buffers and $Cu(In,Ga)Se_2$

This chapter is in part based on the following publications:

- D. Abou-Ras, D. Rudmann, G. Kostorz, S. Spiering, M. Powalla, and A.N. Tiwari, "Microstructural and chemical studies of interfaces between $Cu(In,Ga)Se_2$ and In_2S_3 layers", J. Appl. Phys. **97**(8) no. 084908 (2005).

- D. Abou-Ras, G. Kostorz, A. Strohm, H.W. Schock, and A.N. Tiwari, "Interfacial layer formations between $Cu(In,Ga)Se_2$ and In_xS_y layers", J. Appl. Phys. **98**(12) no. 123512 (2005).

For various In_xS_y-buffered CIGS thin-film solar cells, their efficiencies decrease gradually when the deposition temperature is above about 250 °C (Refs. [95, 106, 73, 118], and also Tables 5.3 and 5.5). This behavior is apparently independent of the deposition technique. In the following, beginning with In_xS_y evaporated from In_2S_3 powder at 300 °C, possible reasons for this behavior will be given.

6.1 Phase identification

In contrast to the In_xS_y layers deposited by powder evaporation at 23 °C (shown in Fig. 5.23), for a corresponding film deposited at 300 °C, a layered structure is revealed (Fig. 6.1). The In_xS_y layer thickness is approximately 70 nm. The HR-TEM image of the In_xS_y/CIGS interface (Fig. 6.2) shows a large density of planar defects in the buffer layer. Since this layered structure is present everywhere in the buffer layer, the crystal structure seems to be completely different from the In_xS_y

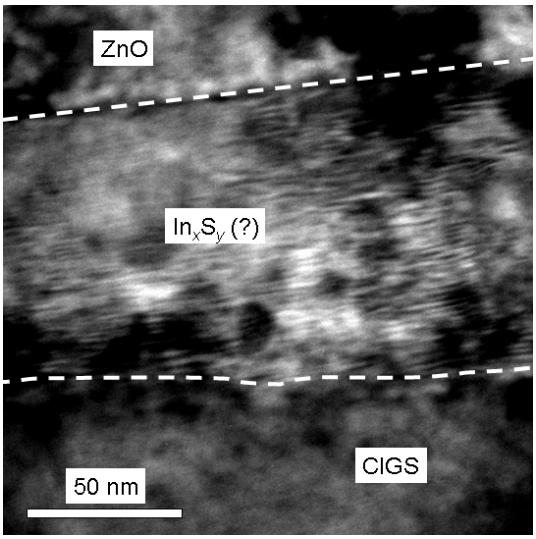

Figure 6.1: Bright-field transmission electron micrograph of a ZnO/In_xS_y/CIGS interface. This In_xS_y layer was deposited at 300 °C by powder evaporation, and the completed cell was air-annealed at 200 °C for 30 min. The buffer has a layered structure.

crystal structures found in the 23 °C and 200 °C samples (Figs. 5.24, 5.25 and 5.26). Apparently, there is an orientation relationship between the CIGS {112) planes and the layered structure in the buffer (Fig. 6.2).
By means of SAED (Fig. 6.2), the phase of the buffer layer deposited at 300 °C was identified as $CuIn_5S_8$, which is an *n*-type semiconductor with a direct band-gap energy of 1.5 eV [119]. Its spinel-type cubic crystal structure contains a large number of vacancies. The role of the band alignment between CIGS and $CuIn_5S_8$ is not yet clear; however, these vacancies and the defects of the $CuIn_5S_8$ layer mentioned above may both act as recombination centers at the *p*-*n* junction of the solar cell. It is already known from studies on $CuInS_2$-based solar cells [120] that the electronic properties of the heterojunction deteriorate as soon as the $CuIn_5S_8$ phase segregates in the films. Thus, it may be assumed that a $CuIn_5S_8$ interfacial layer could be the reason for a severe deterioration of the photovoltaic properties (Table 5.5).

As for the powder-evaporated In_xS_y layer deposited at 300 °C, a layered structure is visible in sputtered In_xS_y deposited at 340 °C in the BF-TEM image of the ZnO/In_xS_y/CIGS cross-section (Fig. 5.19). The HR-TEM image of the In_xS_y/CIGS interface (Fig. 6.3) also shows a large density of planar defects in the buffer layer as well as an orientation relationship between the CIGS {112) planes and the layered structure in the buffer. And just as for the powder-evaporated sample, the phase of the sputtered In_xS_y buffer deposited at 340 °C was identified

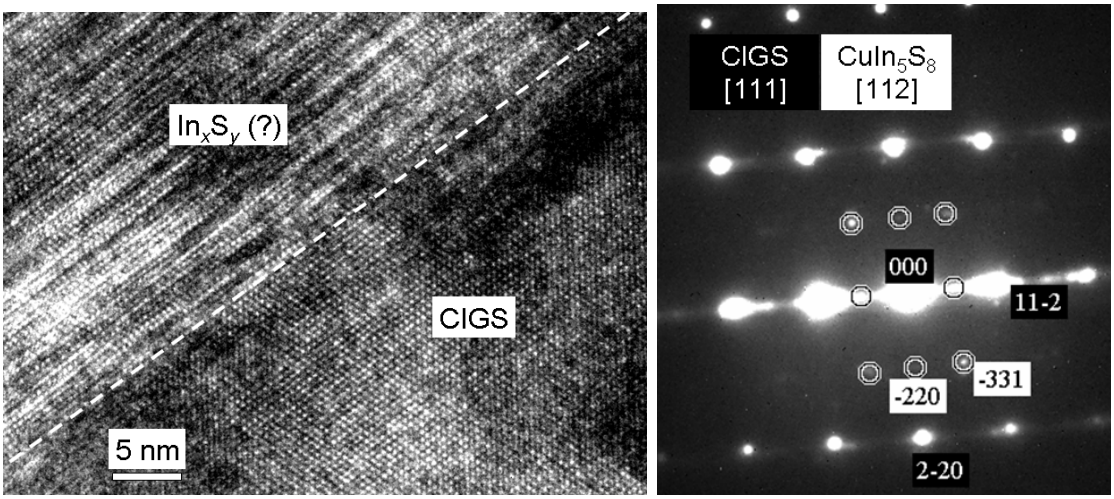

Figure 6.2: Left: High-resolution transmission electron micrograph of a powder-evaporated In_xS_y/CIGS interface. This In_xS_y layer was deposited at 300 °C by powder evaporation, and the completed cell was air-annealed at 200 °C for 30 min. A large density of planar defects is revealed in the buffer layer. Right: Selected-area electron diffraction pattern from the interface shown in the high-resolution transmission electron micrograph. The structure of the buffer layer deposited at 300 °C was identified as that of $CuIn_5S_8$. The reflections related to $CuIn_5S_8$ are outlined by circles.

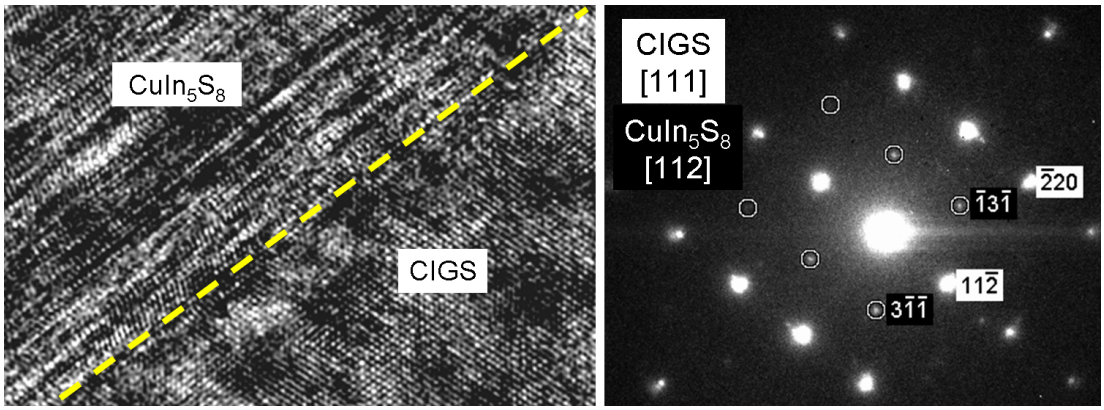

Figure 6.3: Left: High-resolution transmission electron micrograph of an In_xS_y/CIGS interface. This In_xS_y layer was deposited at 340 °C by sputtering. A large density of planar defects is revealed in the buffer layer. Right: Selected-area electron diffraction pattern from the interface shown in the high-resolution transmission electron micrograph. The phase of the buffer layer deposited at 340 °C was identified as $CuIn_5S_8$. The reflections related to $CuIn_5S_8$ are outlined by circles.

by means of SAED as $CuIn_5S_8$ (Fig. 6.3).

Planarly strained layers similar to the $CuIn_5S_8$ layers shown in Figs. 6.2 and 6.3 have also been found at interfaces between CIGS and ALD-In_2S_3 deposited at a substrate temperature of 240 °C and between CIGS and In_xS_y deposited by co-evaporation at 280 °(Fig. 6.4). It is probable that also at these interfaces, $CuIn_5S_8$ formed, since the atomic planes in the intermediate layer for the ALD

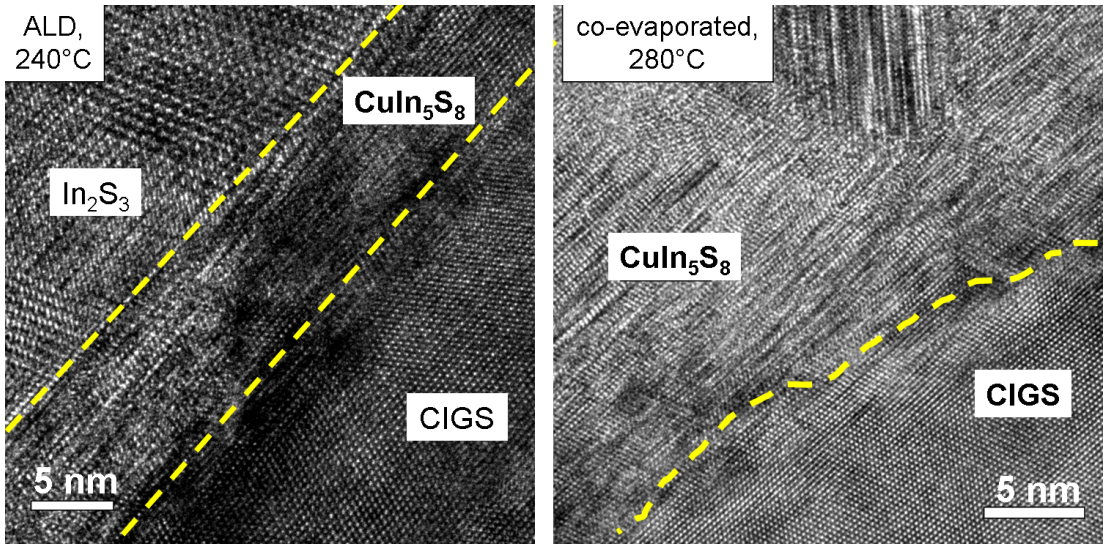

Figure 6.4: Left: High-resolution transmission electron micrographs of In_xS_y/CIGS interfaces. The In_xS_y layers were deposited at 240 °C by ALD (left) and at 280 °C by co-evaporation. Planarly strained layers similar to the $CuIn_5S_8$ layers shown in Figs. 6.2 and 6.3 appear on the buffer sides of these ALD-In_2S_3/CIGS and co-evaporated In_xS_y/CIGS interfaces.

sample and those for the buffer layer in the co-evaporated sample (Fig. 6.4) exhibit similar interplanar distances as the $CuIn_5S_8$ layers identified in Figs. 6.2 and 6.3. Also, elemental distribution profiles across the ALD-In_2S_3/CIGS and co-evaporated In_xS_y/CIGS interfaces (Figs. 5.5 and 6.5) reveal similarities with those for $CuIn_5S_8$/CIGS interfaces (Figs. 5.22 and 5.28). Assuming a Cu:In ratio of 1 on the (not depleted) CIGS side of the interface and a In:S ratio of 5:8 on the buffer side of the interface, the Cu concentration in the co-evaporated In_xS_y buffer can be estimated to about 11 at.% (Fig. 6.5).

Thus, it may be assumed that a $CuIn_5S_8$ layer forms at interfaces between CIGS and In_xS_y deposited by any technique at substrate temperatures higher than about 250 °C. A possible, simple model for the $CuIn_5S_8$ formation will be given in the following section. It has to be pointed out that all measurements have been per-

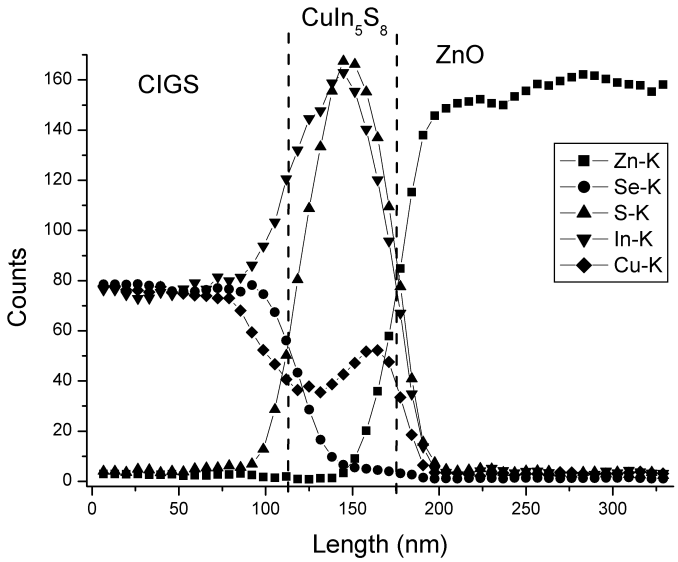

Figure 6.5: Elemental distribution profiles across ZnO/$CuIn_5S_8$/CIGS interfaces. The buffer layer was deposited by co-evaporation from In and S powders at 280 °C. Cu depletion on the CIGS side of the interface and a local maximum of the Cu signal in the buffer layer are revealed, both effects similar to ALD-In_2S_3 and sputtered In_xS_y samples.

formed on samples with already grown $CuIn_5S_8$; no information can be obtained about the growth kinetics from the results obtained by TEM and related techniques. Thus, the model presented in the following section relies considerably on data from the literature, apart from own results.

6.2 Model for the $CuIn_5S_8$ formation

What is needed for the formation of $CuIn_5S_8$ during the deposition of In_xS_y on CIGS? Obviously, Cu diffusion from CIGS into the buffer is one of these requirements. Cu diffusion is found for all In_xS_y/CIGS interfaces studied here, probably induced by a gradient of the chemical potential between In_xS_y and CIGS, and intensified by the substrate temperature. The vacancies present in the various In_xS_y phases may be partially responsible for this gradient of the chemical potential. Generally, Cu shows a high mobility and tends to diffuse from CIGS into divers buffer materials, also, e.g., into CdS as shown in chapter 4.
The ternary Cu-In-S system with the existing binary and ternary phases, as well as a tentative quasi-binary phase diagram of Cu_2S-In_2S_3 (from Ref. [121]) are shown in Fig. 6.6. According to this phase diagram, $CuIn_5S_8$ may form already for very low Cu concentrations, in co-existence with the In_2S_3 phase. For samples with In_xS_y buffers deposited by ALD, sputtering and powder evaporation, the Cu

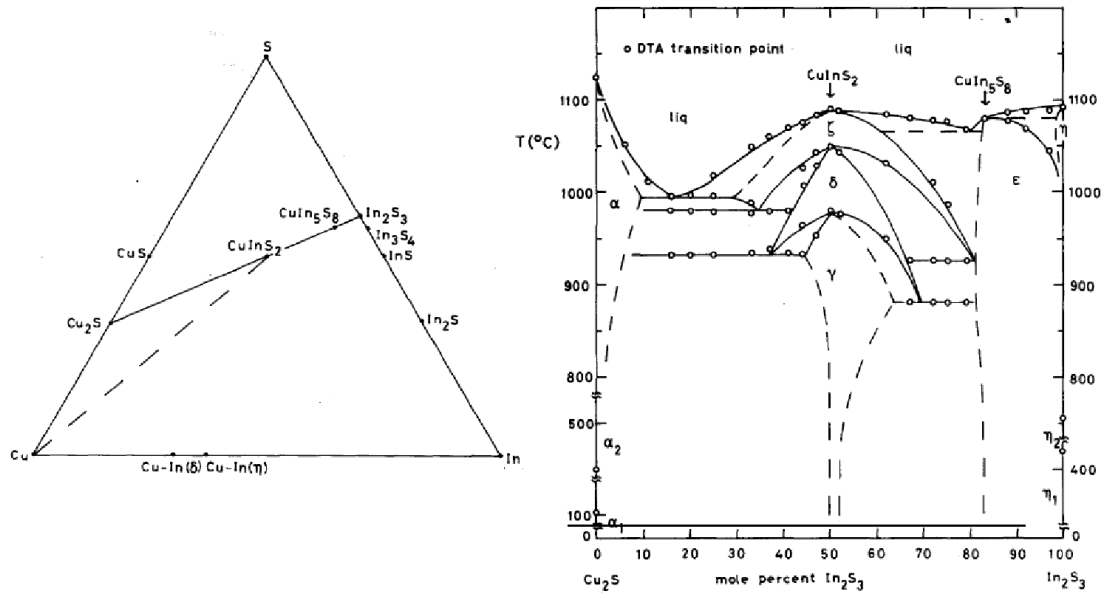

Figure 6.6: Left: The ternary Cu-In-S system with the existing binary and ternary phases, showing the binary join Cu_2S-In_2S_3 and the triangle Cu-Cu_2S-$CuInSe_2$. Right: Tentative diagram of the temperature-concentration relations along the join Cu_2S-In_2S_3 at moderate pressure(s) (from Ref. [121]).

concentration in In_xS_y was always estimated to be quite large, about 5 - 11 at.% depending on the deposition temperature.
However, a large Cu concentration in In_xS_y does not seem to be sufficient for the formation of $CuIn_5S_8$. This phase could not be revealed by SAED or HR-TEM in any sample with an In_xS_y buffer produced at temperatures up to about 230 °C (it has to be pointed out that the temperatures given here were measured by different methods in different laboratories, thus, these values have to be considered with care). Obviously, substrate temperatures above about 230 °C are another requirement for the formation of $CuIn_5S_8$, besides the Cu diffusion. From the results obtained in the present work, a temperature threshold of about 250 °C can be estimated which has to be overcome in order to form $CuIn_5S_8$. This value agrees well with results obtained by Adurodija et al. [122], who sulfurized Cu-In at various temperatures and found $CuIn_5S_8$ to form predominantly between 250 °C and 400 °C. Above 400 °C, $CuInS_2$ was revealed as principal phase by these authors.

As mentioned above, $CuIn_5S_8$ exhibits a spinel-type cubic crystal structure, showing a large density of vacancies on the tetrahedral and octahedral cation sites [123]. The crystal structure of the mineral *spinel*, $MgAl_2O_4$, is shown in Fig. 6.7. The tetrahedral sites, occupied by Mg, and the octahedral sites, occupied by Al, are

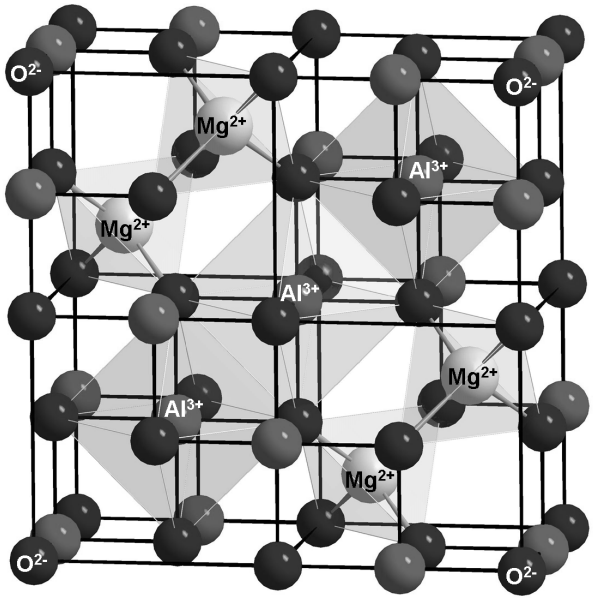

Figure 6.7: The crystal structure of the mineral spinel, $MgAl_2O_4$. Mg atoms reside on tetrahedral, Al atoms on octahedral sites. Oxygen atoms occupy the edges of the cubic crystal structure (by courtesy of I. Hartenbach, Institut für Anorganische Chemie, Universität Stuttgart, Germany).

highlighted. The lattice constant a of the $CuIn_5S_8$ cubic structure is $a = 10.69$ Å [124], almost identical to that of the cubic, vacancy-defective spinel-type $In_{2.8}S_4$ ($a = 10.73$ Å [125] [1]), an In_xS_y phase stable at room temperature [72]. According to Ohmuro et al. [126], the $In_{2.8}S_4$ (or In_2S_3, as called by these authors) crystal structure exhibits in average $\frac{8}{3}$ vacancies per unit cell on the tetrahedral sites of the lattice, which may be occupied by Cu in order to form the stoichiometric spinel-type $CuIn_5S_8$. Phase transformation between $CuIn_5S_8$ and $In_{2.8}S_4$ is facilitated by the similarity of the crystal structures. In addition, the crystal structures of all known In_2S_3 modifications as well as those of monoclinic In_6S_7 and orthorhombic InS (summarized in Table 6.1) show similarities since phase transformations between these structures are simply based on ordering or disordering in the defective spinel structures [72]; i.e., the crystal structures of these In_xS_y phases are all similar to the cubic $CuIn_5S_8$ structure, even though not as plainly as for cubic $In_{2.8}S_4$. As revealed by the XRD measurements of sputtered In_xS_y layers (Fig. 5.16), a layer deposited at 340 °C exhibited tetragonal β-In_2S_3, cubic α-In_2S_3 and orthorhombic InS crystal structures. β-In_2S_3 and cubic α-In_2S_3 show preferential growth in [103] and [111] directions. It is interesting to note that the interplanar distances d_{206} of β-In_2S_3 (3.11 Å), d_{111} of α-In_2S_3 (3.10 Å) and d_{222} of $CuIn_5S_8$ (3.08 Å) are similar

[1] $In_{2.8}S_4$ is sometimes (e.g., [98]) also referred to as α-In_2S_3

Table 6.1: The crystal structures of $CuIn_5S_8$ and various In_xS_y phases existing according to the equilibrium In-S phase diagram [72] for sulfur concentrations ranging from 49 to 70 at.% and temperatures up to 450 °C. The In_xS_y phases are listed with decreasing sulfur concentration.

Phase	Crystal structure	lattice constants	Comments	References
$CuIn_5S_8$	cubic	$a = 10.69$ Å	-	[124]
$In_{2.8}S_4$	cubic	$a = 10.73$ Å	at temperatures above 414 °C also named α-In_2S_3	[125]
α-In_2S_3	cubic	$a = 5.37$ Å	stable between 414 and 750 °C	[72, 98]
β-In_2S_3	tetragonal	$a = 7.62$ Å, $c = 32.4$ Å	-	[98]
In_6S_7	monoclinic	$a = 9.08$ Å, $b = 3.89$ Å, $c = 17.2$ Å, $\alpha = 90°$, β=101.9°, $\gamma = 90°$	-	[108]
InS	orthorhombic	$a = 3.93$ Å, $b = 4.43$ Å, $c = 10.6$	-	[108]

to each other. Also, d_{206} of β-In_2S_3 is again similar to both, d_{112} of $CuGaSe_2$ (3.21 Å [127]) and d_{112} of $CuInSe_2$ (3.34 Å [90]). As shown by the results presented in Figs. 5.3 and 5.4, orientation relationships between CIGS {112) and β-In_2S_3{103) planes were found for ALD-In_2S_3 samples, and between CIGS {112) and $CuIn_5S_8$ {111) planes for powder-evaporated and sputtered In_xS_y samples (Figs. 6.2 and 6.3). These similarities in crystal structure may facilitate $CuIn_5S_8$ formation when sputtered In_xS_y is deposited on CIGS at 340 °C.

At least partial texture in [103] for the β-phase or in [111] orientation for the α-phase at temperatures above 250 °C have been reported for In_2S_3 thin-films deposited by various techniques other than sputtering, e.g., evaporation from In and S powders [128], ALD [111], and spray pyrolysis [129]. Thus, it may be concluded that for In_xS_y layers deposited by any technique, the In_xS_y phases present in these layers exhibit crystal structures which may be easily transformed into cubic $CuIn_5S_8$, provided Cu is present to a sufficient extent and the energy introduced by the substrate temperature is larger than the activation energy of the $CuIn_5S_8$ formation.

Based on the considerations above, the following model for the $CuIn_5S_8$ formation during the In_xS_y deposition on CIGS absorbers at temperatures above 250 °C can be drawn. In the early stages of the In_xS_y buffer deposition, In and S atoms or molecules arrive on the CIGS surface. Ordering of these atoms or molecules occurs according to the surface energy available. Na, oxygen and hydroxides may be present on the CIGS surface prior to the In_xS_y deposition [130]. These impurities may be present in In_xS_y to small extents. After several monolayers of In_xS_y have formed, a gradient of the chemical potential between CIGS and In_xS_y develops which induces the diffusion of Cu (and Ga to a small extent) from CIGS into In_xS_y. Probably, Cu (and Ga) vacancies in the CIGS lattice can be occupied by In diffusing from In_xS_y into CIGS. A Cu-depleted and In-enriched layer forms on the CIGS side of the interface. In the In_xS_y layer, Cu occupies In sites and vacancies [99]. Various In_xS_y phases may be present in this layer, and their crystal structures are not changed by the incorporation of Cu as long as the substrate temperature during the In_xS_y deposition does not exceed a certain threshold (which is assumed to be about 250 °C). If sufficient thermal energy is provided, a phase transformation from Cu-doped In_xS_y to $CuIn_5S_8$ occurs. This phase transformation is facilitated by the fact that the crystal structures of various In_xS_y phases are similar to that of the cubic $CuIn_5S_8$ phase, and probably most easily induced for Cu-doped $In_{2.8}S_4$, owing to the almost identical crystal structure. Apparently, there is a large lattice mismatch between CIGS and $CuIn_5S_8$ atomic planes. E.g., the difference between $d_{222} = 3.08$ Å for $CuIn_5S_8$ and $d_{112} = 3.34$ Å for $CuInSe_2$ indicates a mismatch of about 8%. As a consequence, planar strains are revealed in the $CuIn_5S_8$ layer, visible by a high density of defects (Figs. 6.2, 6.3 and 6.4), which arises from the compensation of the lattice mismatch. Similar planar defects were found at a PVD-CdS/CIGS interface (Fig. 4.6); these planar defects probably also arise from a substantial lattice mismatch between CIGS and PVD-CdS atomic planes. However, in contrast to PVD-CdS, the crystal structure of $CuIn_5S_8$ was reported to exhibit a large number of vacancies. These vacancies and planar defects at the interface to CIGS may enhance recombination of the generated charges. For substrate temperatures slightly above the threshold temperature of the $CuIn_5S_8$ formation, the amount of Cu diffused from CIGS into the growing In_xS_y layer may not be sufficient for the transformation of the complete Cu-doped In_xS_y layer into $CuIn_5S_8$. This seems to be the case for the ALD-In_2S_3 layer grown at 240 °C (Fig. 5.4). As revealed by comparison of the linear distribution profiles across the CIGS/In_2S_3 interface of this sample (Fig. 5.5) with those of samples where In_xS_y was deposited at temperatures higher than 240 °C (by sputtering at 340 °C, Fig. 5.22 and by co-evaporation at 280 °C, Fig. 6.5), the concentration of Cu in the buffer is considerably lower for the ALD sample produced at 240 °C. Therefore, $CuIn_5S_8$ may form only as intermediate layer between CIGS and In_2S_3

(or more generally In_xS_y) for substrate temperatures slightly above the threshold temperature of the $CuIn_5S_8$ formation. Only for still higher temperatures, sufficient amounts of Cu are provided in order to transform the complete Cu-doped In_xS_y layer into $CuIn_5S_8$.

This model presented above is summarized in Fig. 6.8.

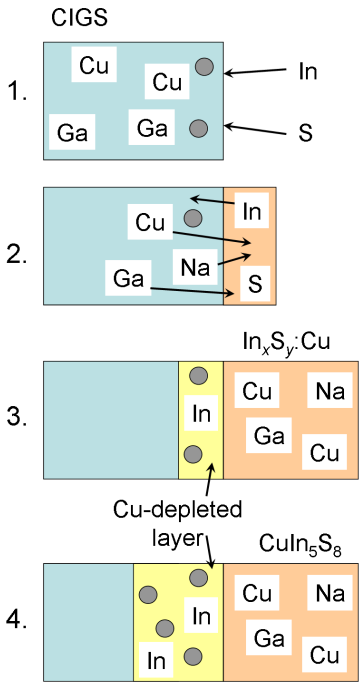

Figure 6.8: Schematics of the formation of Cu-doped In_xS_y and $CuIn_5S_8$ during the deposition of In_xS_y by any technique on CIGS. 1. During the initial stage of the In_xS_y deposition, Na as well as oxide and hydroxide phases are present on the Cu-depleted CIGS surface (vacancies are indicated by filled circles). 2. When In_xS_y has formed with a certain layer thickness, Cu, Ga and Na diffuse from CIGS into In_xS_y, occupying In sites and vacancies. From In_xS_y, In diffuses into CIGS, occupying Cu and Ga vacancies. 3. A Cu-depleted, In-enriched layer forms between CIGS and Cu-doped In_xS_y (which is also Na- and Ga-doped to a smaller extent). The thickness of this intermediate layer increases with increasing substrate temperature. 4. Above a certain temperature threshold, $CuIn_5S_8$ forms from In_xS_y:Cu, first as intermediate layer between the Cu-depleted CIGS and the remaining In_xS_y:Cu, with further increasing temperature completely replacing In_xS_y:Cu.

Chapter 7

$MoSe_2$ as buffer-layer material in $Cu(In,Ga)Se_2$ solar cells

This chapter is based on the following publications:

- D. Abou-Ras, G. Kostorz, D. Brémaud, M. Kaelin, F.V. Kurdesau, A.N. Tiwari, and M. Döbeli, "Formation and characterisation of $MoSe_2$ in $Cu(In,Ga)Se_2$-based solar cells", Thin Solid Films **480-481**, pp. 433-438 (2005).

- D. Abou-Ras, D. Mukherji, G. Kostorz, D. Brémaud, M. Kaelin, D. Rudmann, M. Döbeli, and A.N. Tiwari, "Dependence of the $MoSe_2$ formation on the Mo orientation and the Na concentration for $Cu(In, Ga)Se_2$ thin-film solar cells", in "Thin-Film Compound Semiconductor Photovoltaics", edited by W. Shafarman, T. Gessert, S. Niki, and S. Siebentritt (Mater. Res. Soc. Symp. Proc. **865**, Warrendale, PA, 2005), pp. F8.1.1-F8.1.6.

7.1 Background

As introduced in section 1.4, a profound understanding of the reaction kinetics of the $MoSe_2$ formation is vital for the development of low resistance electrical back contacts for high efficiency CIGS solar cells. The possible application of $MoSe_2$ as a buffer layer may be demonstrated by considering as an example the interface between the CIGS absorber and a transparent conductive oxide (TCO) as back contact.
TCO may be applied as back-contact material in order to develop multi-junction tandem solar cells which require suitable semi-transparent "bi-facial" cells. Haug et al. [131] assessed various TCOs and suggested that indium tin oxide (ITO) and SnO_x:F can be used to form a quasi-ohmic contact with CIGS, since the CIGS

layers grown on these TCOs showed somewhat non-rectifying I-V characteristics. One approach is to apply a TCO layer as a back contact directly to the CIGS absorber. Efficiencies of up to 14.9% have been reported for solar cells with ITO back contact [132]. However, it was shown that the efficiency depends crucially on the CIGS deposition recipe [132], and also that Ga_2O_3 formation between CIGS and ITO deteriorates the current transport [133]. In addition, Terheggen et al. [134] identified the formation of Ga_2O_3 between ZnO:Al and CIGS.

A second, more convenient approach in order to obtain the flexibility to use any CIGS growth recipe is to find a suitable buffer layer between CIGS and TCO. To achieve this, the capability of the $MoSe_2$ layer of providing low resistance quasi-ohmic contact on alternative back contact materials can be exploited. A very thin $MoSe_2$ layer may be grown on the TCO back contact, e.g., on an ITO layer, acting as a tunnelling quasi-ohmic contact. Thus, the ohmic contact formation is independent of the CIGS deposition recipe, and in addition, the $MoSe_2$ layer acts as a buffer between ITO and CIGS, preventing gallium oxide formation at the ITO/CIGS interface.

In this chapter, an investigation of the reaction kinetics of the $MoSe_2$ formation as well as chemical and structural properties of $MoSe_2$ layers obtained by direct selenization of Mo with Se vapor under various conditions will be presented, in order to define optimum parameters for the growth of a $MoSe_2$ buffer on any metal/semimetal back contact.

7.2 The $MoSe_2$ growth

In the present section, all $MoSe_2$ layers were obtained by selenizing Mo/Si substrates using method (i) (section 2.2.5). This selenization method with high Se source temperature was chosen, since it resulted in sufficiently large $MoSe_2$ thicknesses in order to obtain reduced errors of their measurements.

7.2.1 Identification of the Mo-Se phase

Since separate XRD, SAED, HRTEM or EDX measurements delivered ambiguous results on the identification of the Mo-Se compound as $MoSe_2$ all of the measurements presented in this subsection were performed on the same Mo layer selenized at 580 °C and a non-selenized Mo layer as a reference. Therefore, a Mo layer about 175 nm thick was deposited on a Si wafer. Samples were cut from this wafer and selenized for various durations at 580 °C. The thicknesses of the $MoSe_2$ layers formed on Mo were determined by means of RBS.

Fig. 7.1a shows the RBS pattern obtained for a Mo/Si substrate selenized for 60 min at 580 °C. The simulated Mo layer thickness of 115 nm and the $MoSe_2$ layer thickness of 300 nm are confirmed by the BF-TEM image (Fig. 7.1b). The original Mo layer thickness was approximately 175 nm. The thickness of 300 nm for $MoSe_2$ formed from about 60 nm Mo corresponds to the change in molar density (see Fig. 7.2). The hexagonal structure of $MoSe_2$ with $a = 0.328$ nm and $c = 1.29$ nm [135] consists of Se-Mo-Se sheaths perpendicular to the c-axis (Fig. 7.3).

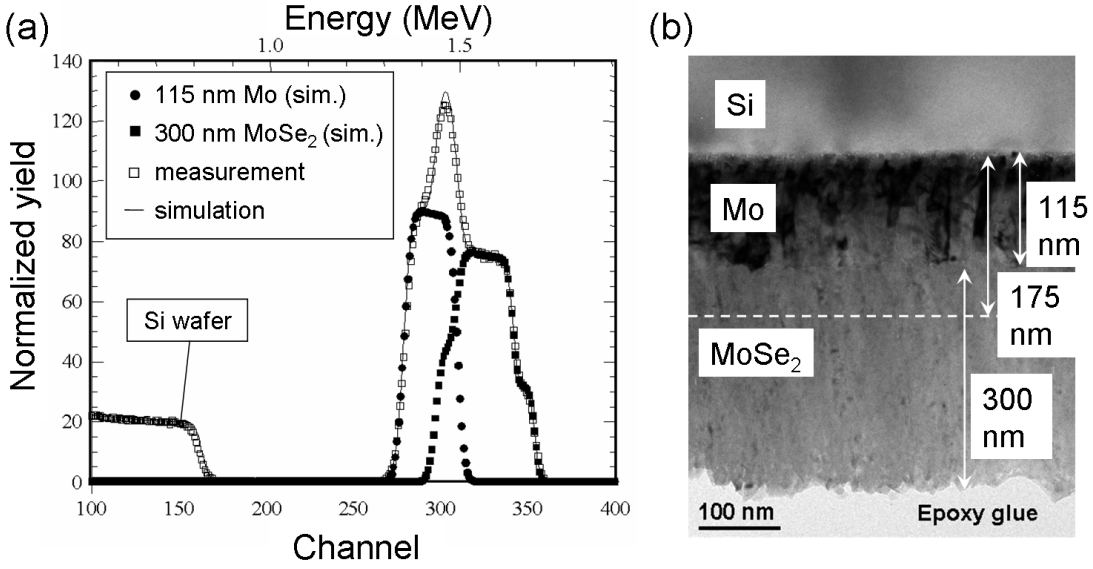

Figure 7.1: (a) Rutherford backscattering spectrum of a selenized Mo layer on Si, and its simulation obtained by the RUMP software. (b) Bright-field transmission electron micrograph of the Si/Mo/$MoSe_2$ interface; the dashed line gives the position of the Mo surface prior to the selenization process.

The XRD measurements (Fig. 7.4a) indicate that the sputtered Mo layer shows a cubic crystal structure with a preferential growth orientation in [110]. From the selenized Mo substrate, two peaks were obtained, 10.0 and 11.0, which correspond to hexagonal $MoSe_2$ and to no other Mo-Se compound (powder XRD patterns of several Mo-Se compounds were simulated and compared with the measurement). The fact that there are only two peaks in the XRD pattern indicates also that the Mo-Se compound has a preferential orientation with respect to the Mo substrate, and in the case of $MoSe_2$ that the average orientation of the c-axis would be parallel to the Mo surface.

The SAED pattern in Fig. 7.4b was obtained from the sample shown in Fig.

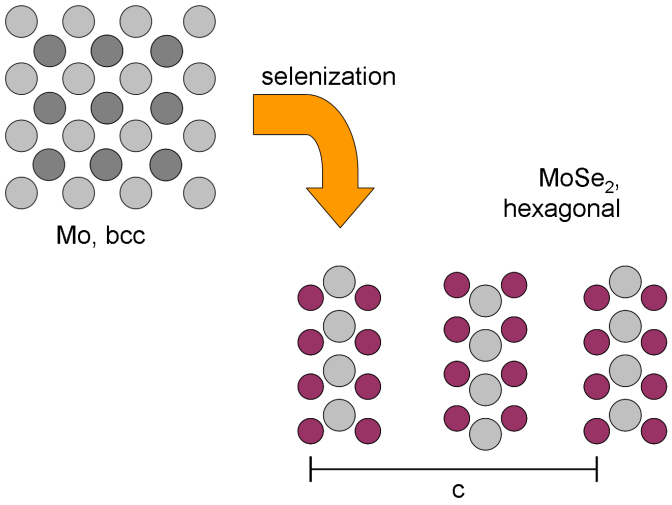

Figure 7.2: The molar density of Mo is much larger in the bcc crystal structure of elemental Mo than in the hexagonal $MoSe_2$ crystal structure.

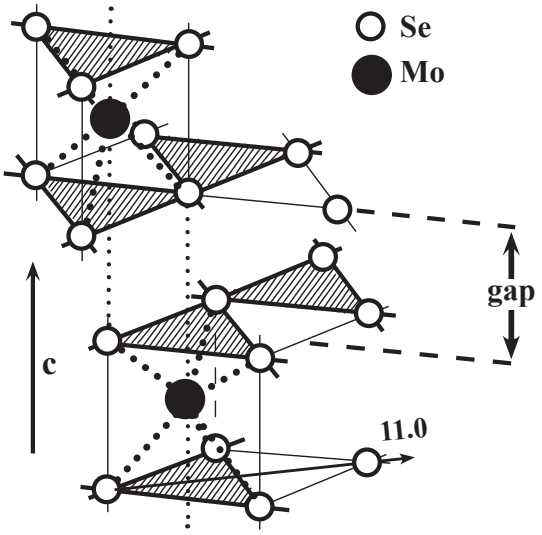

Figure 7.3: The hexagonal crystal structure of the 2H-$MoSe_2$ phase. Its Se-Mo-Se sheaths are oriented perpendicular to the c-axis. The Mo atoms exhibit tetrahedral coordinations (the tetrahedra are indicated by dotted lines).

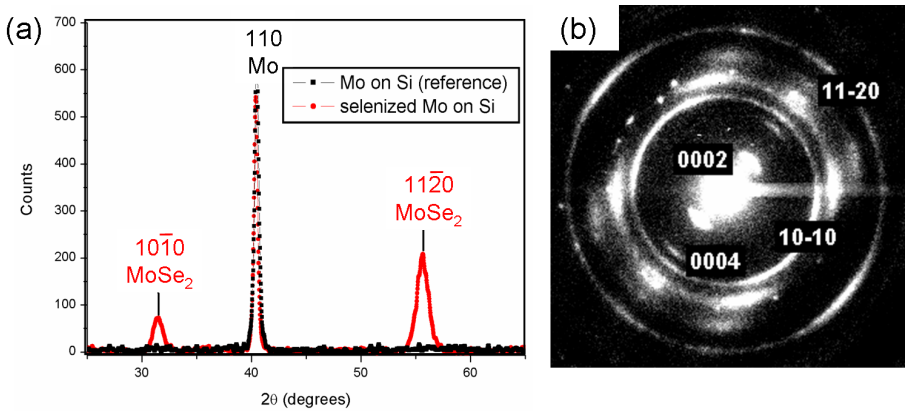

Figure 7.4: (a) X-ray diffraction pattern of a Mo layer on Si and a selenized sample; the 110 peak of Mo and the 10.0 and 11.0 peaks of $MoSe_2$ are visible. (b) Electron diffraction pattern of the cross-section sample shown in Fig. 7.1b; 00.2 and 00.4 reflections as well as 10.0 and 11.0 rings of $MoSe_2$ are visible.

7.1b, i.e., a cross-section sample of the Mo/Mo-Se compound interface. Since only planes parallel to the incident electron beam produce reflections on the SAED pattern, the fact that 00.2 and 00.4 reflections of $MoSe_2$ are visible and that there are 10.0 and 11.0 rings, indicates again that the Mo-Se compound is most probably $MoSe_2$, and that in this case the average orientation of the c-axis is parallel to the Mo surface.
Finally, the Mo/Mo-Se interface was investigated by HR-TEM (Fig. 7.5a). The Mo-Se compound in this figure can be identified as $MoSe_2$ since the measured distance between every second layer in the magnified section, 1.35 nm, compares well with the lattice constant $c = 1.29$ nm of the $MoSe_2$ hexagonal structure [135]. The $MoSe_2$ layer shows the c-axis parallel to the Mo surface, as suggested by the XRD and the SAED measurements. By means of an EDX line scan across the Mo/Mo-Se compound interface (Fig. 7.5b), the Mo-Se compound was also identified as $MoSe_2$ in the Mo-Se region: the Se signal is twice as large as the Mo signal. It is possible to relate the signal ratio of the two elements to their concentration ratio, since the interaction cross-sections of the electrons with both elements are quite similar.

7.2.2 Reaction kinetics of the $MoSe_2$ formation

For Mo substrates selenized at a temperature of 580 °C, which provided sufficient $MoSe_2$ layer thicknesses, and in the case where the c-axis of the $MoSe_2$ layer is parallel to the Mo surface, the diffusion length of the Se through the already formed $MoSe_2$ layer can be deduced from the $MoSe_2$ thickness (d) dependence on

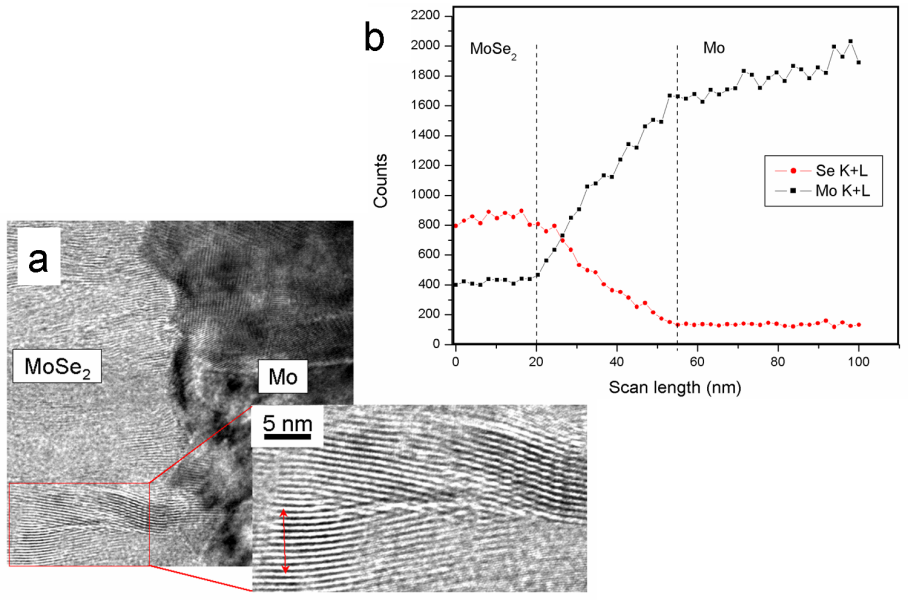

Figure 7.5: (a) High-resolution transmission electron micrograph of the Mo/$MoSe_2$ interface; in the magnified part, the distance of the layers corresponds to the c-value of the hexagonal $MoSe_2$ crystal structure. (b) Line scan obtained by energy-dispersive x-ray spectrometry applied on the cross-section sample shown in Fig. 7.1; on the $MoSe_2$ side of the interface, the Se signal is twice as large as the Mo signal.

the selenization duration (t_{sel}), assuming always equilibrium Se concentration at the surface. According to the results from RBS, BF-TEM and EDX, a $MoSe_2$ layer with homogeneous composition and uniform layer thickness is formed. This implies that there is a stable reaction front between the $MoSe_2$ and the Mo layer, moving at a speed controlled by the diffusion of Se in $MoSe_2$. The diffusion constant D of Se in $MoSe_2$ may thus be estimated from

$$< d^2 >= 2\,D\,t_{sel} \tag{7.1}$$

where $<d^2>$ is the mean value of the square of diffusion length given by the $MoSe_2$ layer thickness and t_{sel} is the selenization duration. In Fig. 7.6, the $MoSe_2$ thickness (d) is plotted versus the selenization duration (t_{sel}) for a substrate temperature of 580 °C. The measured values agree well with the dashed curve which gives the $d(t_{sel})$ square root dependence with $D = 5\text{x}10^{-14}$ cm^2/s. Such a parabolic behavior for the $MoSe_2$ growth by selenization of Mo precursors was also found by other authors (e.g., [136, 137]).

Unfortunately, the selenization duration is not precisely known owing to low heating and cooling rates, and also the error of the temperature measurement is ap-

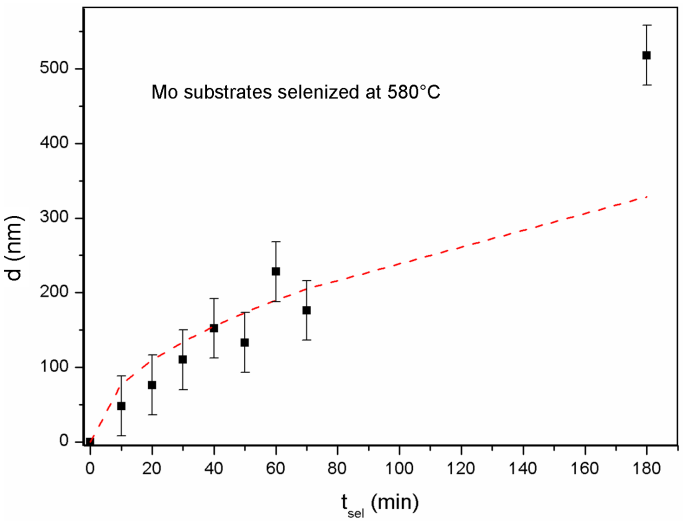

Figure 7.6: The $MoSe_2$ layer thickness x versus the selenization duration t_{sel}, obtained at a substrate temperature of 580 °C; the dashed curve gives the $d(t_{sel})$ square root dependence with $D = 5x10^{-14}$ cm^2/s. Owing to the uncertainty of the temperature measurement, only an estimate of the diffusion constant was possible.

proximately ±10 K. These sources of error contribute to an error of the $MoSe_2$ layer thickness of about 40 nm for a substrate temperature of about 580 °C (see section 7.3.1). Nevertheless, the diffusion constant of Se in $MoSe_2$ at 580 °C can be estimated to be in the range of 10^{-14}-10^{-13} cm^2/s.

7.2.3 Influence of the *c*-axis orientation on the $MoSe_2$ growth kinetics and on its mechanical and electrical properties

For further considerations of the $MoSe_2$ growth and influences thereon by various parameters, the procedure of the $MoSe_2$ formation by selenization of Mo precursors will be described. When Se atoms or molecules arrive on the Mo surface they react with Mo to form a Mo-Se compound. In polycrystalline Mo layers, Se reacts with Mo not only on the Mo surface but diffuses also into grain boundaries, forming $MoSe_2$ there (Fig. 7.7). It is important to note that the deposition of Se on Mo implies a reaction of both elements, thus, the growth rate of the Mo-Se compound may at least partly be determined by the reaction kinetics. According to the equilibrium phase diagram of the Mo-Se system [138], only two stable Mo-Se compounds exist: $MoSe_2$ and Mo_3Se_4. If excess supply of Se is given during the selenization, generally, only $MoSe_2$ as reaction product is found, as, e.g., by Dutrizac et al. [136] who studied the reaction of Se vapor with molybdenum metal

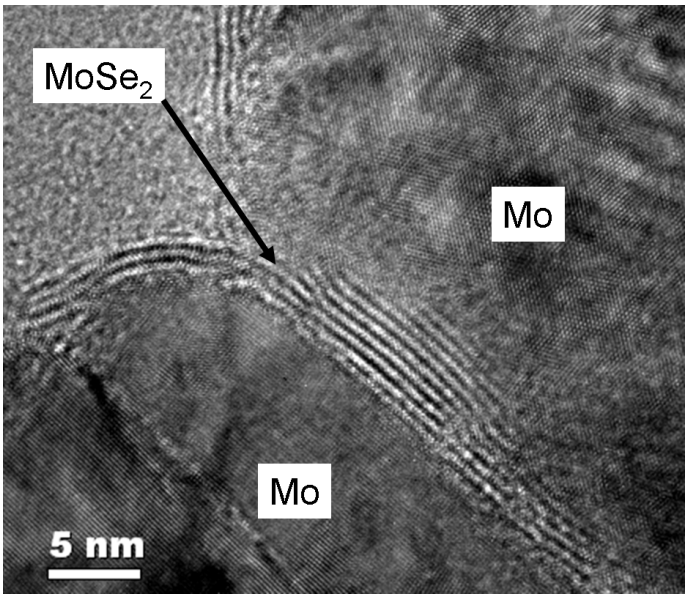

Figure 7.7: Polycrystalline Mo layer, selenized at 580 °C for 60 min. $MoSe_2$ formed not only on the Mo surface, but also at grain boundaries.

at temperatures ranging from 430 to 562 °C. When Se is available only at limited concentrations, predominantly Mo_3Se_4 forms [139].
An important issue for the $MoSe_2$ growth is the $MoSe_2$ *c*-axis orientation (i.e., the orientation of the Se-Mo-Se sheaths, Fig. 7.3) with respect to the Mo surface. Several authors have reported different *c*-axis orientations for different growth conditions (e.g., [140]). I.e., the *c*-axis may be oriented in average parallel (as shown in Fig 7.5a) or perpendicular to the Mo surface. When a $MoSe_2$ layer with a certain thickness has already formed on Mo, Se atoms or molecules have to diffuse through this $MoSe_2$ layer to the $MoSe_2$/Mo interface in order to contribute to further $MoSe_2$ growth. In case of $MoSe_2$, its crystal structure has a strong influence on the diffusion of Se; obviously, its diffusion is facilitated when the Se-Mo-Se sheaths are oriented perpendicular, i.e., when the $MoSe_2$ *c*-axis is oriented parallel to the Mo surface (as already mentioned in section 7.2.2), since Se atoms or molecules may diffuse through the channels of the $MoSe_2$ crystal structure to the $MoSe_2$/Mo interface. For a *c*-axis orientation perpendicular (i.e., the Se-Mo-Se sheaths are oriented parallel) to the Mo surface, the Se diffusion through $MoSe_2$ is impeded (see Fig. 7.8). Depending on the substrate temperature during selenization, Se atoms or molecules may be re-evaporated from the surface before they are able to diffuse into the $MoSe_2$ layer. As will be shown further below, this behavior leads to a self-limiting process where the $MoSe_2$ thickness achievable under certain growth conditions is limited by the diffusion rate of Se through the $MoSe_2$ layer.

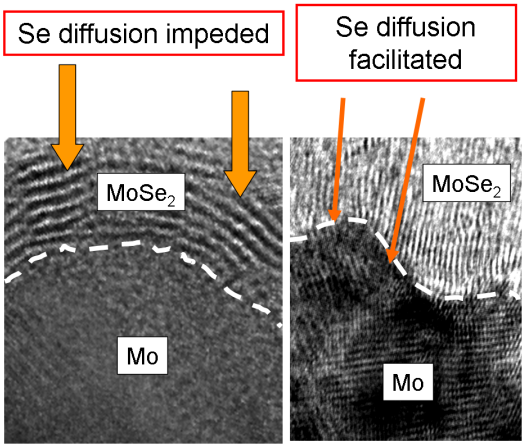

Figure 7.8: The c-axis orientation of the 2H-$MoSe_2$ crystal structure with respect to the Mo surface affects the growth rate of $MoSe_2$.

Apart from the $MoSe_2$ growth kinetics, the c-axis orientation affects also mechanical and electrical properties of the $MoSe_2$, e.g., when this layer is applied as buffer between CIGS and any back contact. Along the c-axis, van-der-Waals bonding is found between the Se-Mo-Se sheaths (Fig. 7.2), whereas perpendicular to the c-axis, parallel to the basal planes of the hexagonal $MoSe_2$ structure, the bonding is of covalent type. I.e., the adhesion is deteriorated when $MoSe_2$ forms with a c-axis in average perpendicular to the Mo surface. This may lead to delamination between Mo/$MoSe_2$ and CIGS, as it often occurs when mechanical stress is applied on a SLG/Mo/$MoSe_2$/CIGS stack. Mechanical stress is unavoidable, e.g., in the frame of specimen preparation for TEM (see section 3.1.1).
For hexagonal MoS_2 single crystals, Evans et al. [141] found that the conductivity perpendicular to the c-axis is larger by two orders of magnitude than parallel to the c-axis. El-Mahalawy et al. [142] suggested that a similar electrical property can be assumed for $MoSe_2$, since the 2H-MoS_2 crystal structure is similar to that of hexagonal $MoSe_2$. Thus, the conductivity across a $MoSe_2$ layer is considerably affected by its average c-axis orientation.
As an example, an interface between CIGS deposited at 580 °C and Mo is shown in Fig. 7.9. A $MoSe_2$ intermediate layer is revealed (formed during the deposition of CIGS) with its Se-Mo-Se sheaths oriented preferentially parallel to the Mo surface. In the example shown, the preferential orientation of the $MoSe_2$ layer to the Mo surface does not provide a good adhesion and electrical contact of the CIGS/$MoSe_2$/Mo interface. However, the role of a $MoSe_2$ buffer layer between CIGS and any back contact is to act as a quasi-ohmic tunnel junction (see section 1.4). Therefore, the $MoSe_2$ layer should exhibit a thickness sufficiently small for tunnelling. In order to achieve an optimum electronic junction between CIGS

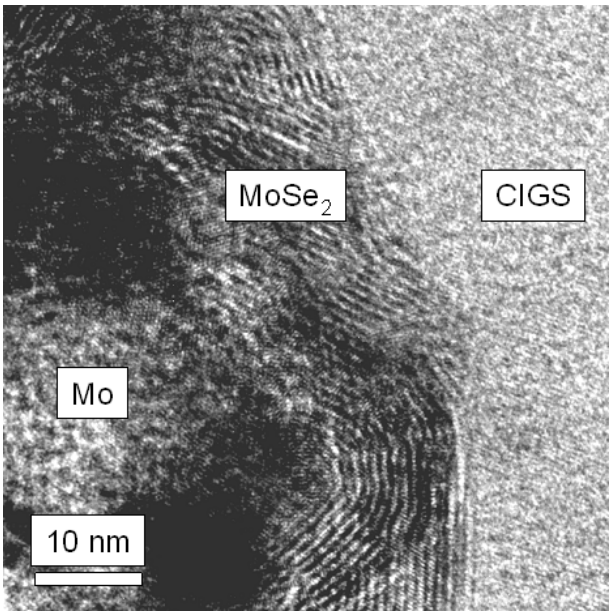

Figure 7.9: Bright-field transmission electron micrograph of the Mo/$MoSe_2$/CIGS interface, showing that the sheets of the layered $MoSe_2$ structure are oriented preferentially parallel to the Mo surface.

an the back contact, and hence a good solar-cell performance, an intermediate $MoSe_2$ layer with as *c*-axis oriented perpendicular to the Mo surface and a thickness limited by the reduced Se diffusion through $MoSe_2$ may be more desirable than a $MoSe_2$ layer with a *c*-axis oriented parallel to the Mo surface leading to a considerably large $MoSe_2$ thickness.

7.3 Influences of various parameters on the $MoSe_2$ formation

As outlined in the previous section, it is important to identify and control those parameters which are responsible for a $MoSe_2$ growth with the *c*-axis oriented parallel to the Mo surface. It was reported that various parameters may affect the $MoSe_2$ growth. Nishiwaki et al. [140] showed that the $MoSe_2$ formation and *c*-axis orientation depend on the state of Mo prior to selenization and on the medium of selenization - pure Se vapor or Se mixed with In- and Cu-species can make a difference. Palm et al. [68] pointed out that the oxygen concentration in Mo prior to selenization has a considerable impact on the $MoSe_2$ formation. In the present section, the effects of the Se source temperature, the substrate temperature, the Mo orientation and the Na concentration will be reported. Fundamental experiments

were conducted where Mo-coated Si wafers were selenized under these various conditions. Compared with glass substrates, Si provides an easier evaluation of the $MoSe_2$ layer properties and avoids substrate related ambiguities. The samples selenized and measured by RBS, ERDA, XRD and TEM are listed in Table 7.1.

7.3.1 $MoSe_2$ orientations at substrate temperatures of 450 °C and 580 °C

All Mo/Si substrates presented in this subsection were selenized by use of method (i) (section 2.2.5). Fig. 7.10 shows the temperature dependence of the $MoSe_2$ layer thickness. A selenization duration of 40 min was chosen to achieve relatively large $MoSe_2$ layer thicknesses. For substrate temperatures lower than about 550 °C, the

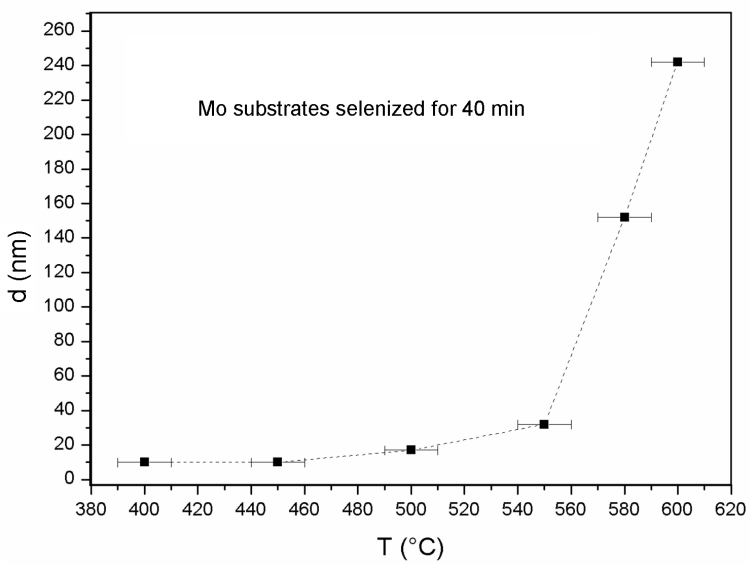

Figure 7.10: $MoSe_2$ layer thickness versus substrate temperature during the selenization process; for temperatures lower than about 550 °C, the $MoSe_2$ layer thickness is rather low, but it increases rapidly with increasing temperature for substrate temperatures higher than about 550 °C.

$MoSe_2$ layers reach a rather small thickness of about 10-30 nm, whereas the $MoSe_2$ layer thickness increases strongly for substrate temperatures higher than about 550 °C. It appears that for these two temperature ranges (below and above about 550 °C), different processes dominate the $MoSe_2$ growth. Assuming the rates of these processes proportional to differences in thickness d, the activation energies can be estimated to be about 0.4 eV for the dominating process below 550 °C and 2.5 eV for the dominating process above 550 °C.
For a sample with $MoSe_2$ produced at 580 °C, the XRD measurements (Fig. 7.4a)

Table 7.1: Selenization conditions, $MoSe_2$ thicknesses and c-axis orientations with respect to the Mo surface of samples studied by RBS, ERDA, XRD and TEM. The $MoSe_2$ thicknesses were determined by means of RBS and ERDA, the $MoSe_2$ c-axis orientations by means of XRD and TEM. Those orientations which were not confirmed by XRD or TEM measurements are indicated by question marks.

Sample	Duration (min)	Method	$MoSe_2$ thickness	c-axis orientation
Mo single crystal, 100, selenized at 580 °C	120	(i)	1500	parallel
Mo single crystal, 110, selenized at 580 °C	120	(i)	1700	parallel
Mo single crystal, 111, selenized at 580 °C	120	(i)	1300	parallel
Mo/Si, selenized at 580 °C	180	(i)	516	parallel
Mo/Si, selenized at 580 °C	60	(i)	300	parallel
Mo/Si, selenized at 580 °C	60	(ii)	30	perpendicular
Mo/5nm NaF/Si, selenized at 580 °C	60	(ii)	18	perpendicular?
Mo/10nm NaF/Si, selenized at 580 °C	60	(ii)	18	perpendicular?
Mo/15nm NaF/Si, selenized at 580 °C	60	(ii)	18	perpendicular
Mo/Si, selenized at 450 °C	60	(i)	10	perpendicular
Mo/Si, selenized at 450 °C	60	(ii)	5	perpendicular
Mo/5nm NaF/Si, selenized at 450 °C	60	(ii)	11	perpendicular?
Mo/10nm NaF/Si, selenized at 450 °C	60	(ii)	21	perpendicular?
Mo/15nm NaF/Si, selenized at 450 °C	60	(ii)	21	perpendicular

show some texture of both the Mo and the $MoSe_2$ layers, indicating at least partial epitaxial growth of both layers in the present samples (on Si substrate). With increasing temperature, the different thermal expansions of Mo and $MoSe_2$ probably lead to a change in the lattice mismatch and thus a change of the preferred c-axis orientation. For a substrate temperature of 450 °C, selenization for 10, 20, 30, 40 and 60 min always resulted in the same $MoSe_2$ layer thickness of about 10 nm. This indicates that the c-axis orientation of the $MoSe_2$ layer might be perpendicular to the Mo substrate for a substrate temperature of 450 °C, and thus the $MoSe_2$ growth rate is very small owing to the small diffusion rates of Se through the $MoSe_2$ layer.
It has been shown that selenization of Mo at 580 °C results in a $MoSe_2$ orientation with the c-axis parallel to the Mo surface (Fig. 7.5a). Fig. 7.11a shows the BF-TEM image of the interface between $MoSe_2$ formed at 450 °C and Mo. The layered structure of the $MoSe_2$ covers the Mo substrate uniformly and has a thickness of about 10 nm. The Se-Mo-Se sheaths of the layered structure are oriented preferentially parallel to the Mo surface. The HR-TEM image of this $MoSe_2$/Mo interface (Fig. 7.11b) shows that the measured distance between every second sheath of the $MoSe_2$ layer, 1.29 nm, agrees well with the lattice constant c of the hexagonal 2H-$MoSe_2$ structure, $c = 1.29$ nm [135]. Direct comparison of

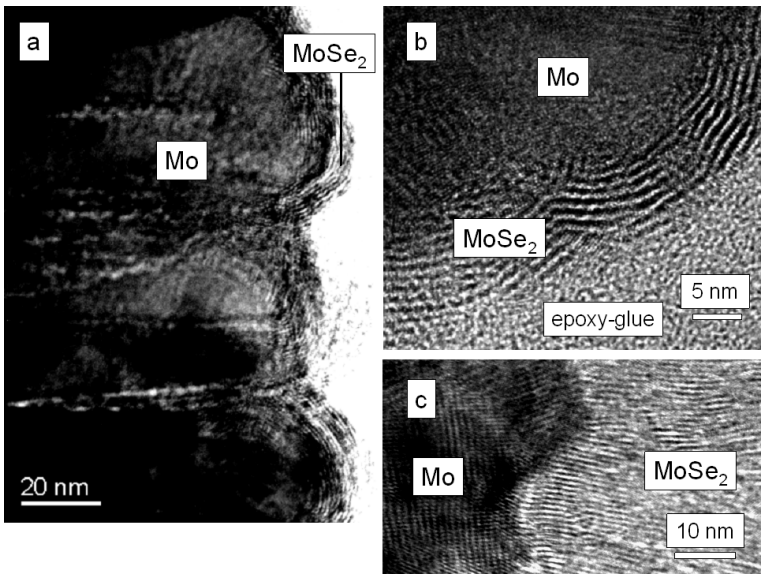

Figure 7.11: (a) Bright-field transmission electron micrograph of the interface between $MoSe_2$ formed at 450 °C and Mo. (b) High-resolution transmission electron micrograph of the same interface. (c) High-resolution transmission electron micrograph of the interface between $MoSe_2$ formed at 580 °C and Mo (the same sample as shown in Fig. 7.5a).

the orientations of the *c*-axes of $MoSe_2$ layers grown at 450 °C (Figs. 7.11a and b) and at 580 °C (Fig. 7.11c, the same sample as shown in Fig. 7.5a) reveals a change from perpendicular to parallel with respect to the Mo surface.

Mallouky et al. [143] found that also for sputtered $MoSe_2$, the *c*-axis orientation depends on the substrate temperature: for lower substrate temperatures, the *c*-axis was perpendicular, for higher ones it was parallel to the substrate. Even if those $MoSe_2$ layers were formed by dc diode sputtering and not by selenization of Mo substrates, a similar temperature behavior may be assumed also for these sputtered $MoSe_2$ films.
Nishiwaki et al. [140] deposited CIGS on Mo/SLG substrates at various temperatures and found that the thickness of the intermediate $MoSe_2$ layer formed between CIGS and Mo increased with increasing substrate temperature, particularly gradually for temperatures above 550 °C (similarly to the behavior shown in Fig. 7.10). These results may indicate that the change in orientation found for the $MoSe_2$/Mo/Si samples also occurs for CIGS/$MoSe_2$/Mo/SLG stacks, i.e., for CIGS solar cells.

7.3.2 Dependence on the Mo orientation

The XRD patterns of the Mo single crystals (oriented in [100], [110] and [111]) selenized at 580 °C (Fig. 7.12) reveal a pronounced texture of $MoSe_2$ in [11.0]. Also, it is clear from these measurements that the $MoSe_2$ orientation is independent from the orientation of the Mo single crystals. To understand this, it has to be considered that the $MoSe_2$ growth is based on a reaction of Se with Mo, rather than a deposition of Se atoms or molecules on the Mo surface. Thus, the Mo orientation needs not to influence the $MoSe_2$ texture. The RBS measurements of these samples show a very thick $MoSe_2$ layer on top of the single-crystalline Mo substrates (see Table 7.1). The $MoSe_2$ thicknesses are between 1.3 and 1.7 µm. On the contrary, for polycrystalline Mo, the selenization at 580 °C for 3 h using method (i) (section 2.2.5) led to a $MoSe_2$ thickness of about 500 nm (see Table 7.1). Fig. 7.13a shows a HR-TEM micrograph of oriented $MoSe_2$ sheaths, grown on single crystal Mo with [110] orientation, which have a much more pronounced preferential orientation than those of the $MoSe_2$ grown on polycrystalline Mo shown in Figs. 7.5a and 7.11c. Considering the very small grain sizes of polycrystalline Mo (several nm), its surface roughness can be assumed to be much larger than that of Mo single crystals. This increased surface roughness may result in a less pronounced $MoSe_2$ texture with the *c*-axis parallel to the Mo surface, thus reducing the Se diffusion through the layered $MoSe_2$ structure and leading to smaller $MoSe_2$ thicknesses. The interface between the $MoSe_2$ and the single crystal Mo is abrupt, as revealed by the HR-TEM micrograph shown in Fig. 7.13b.

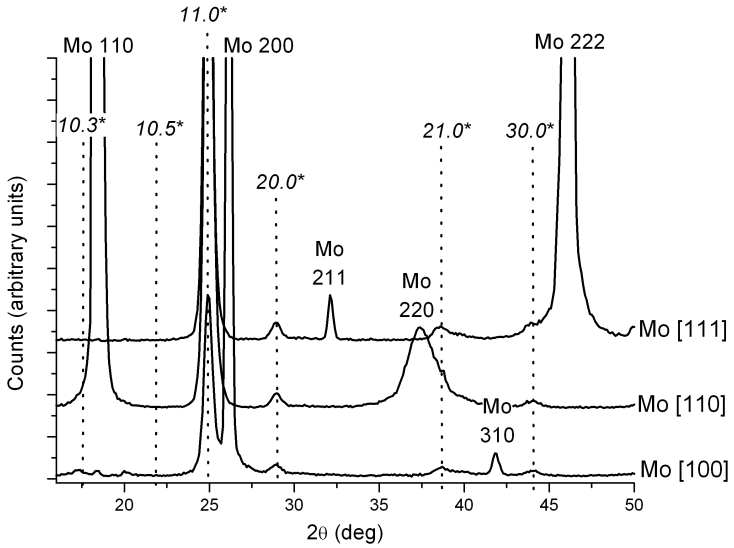

Figure 7.12: X-ray diffraction patterns of Mo single crystals selenized at 580 °C; these patterns reveal a pronounced orientation of $MoSe_2$ in [11.0], irrespective of the Mo orientations. The peaks from $MoSe_2$ are marked with stars.

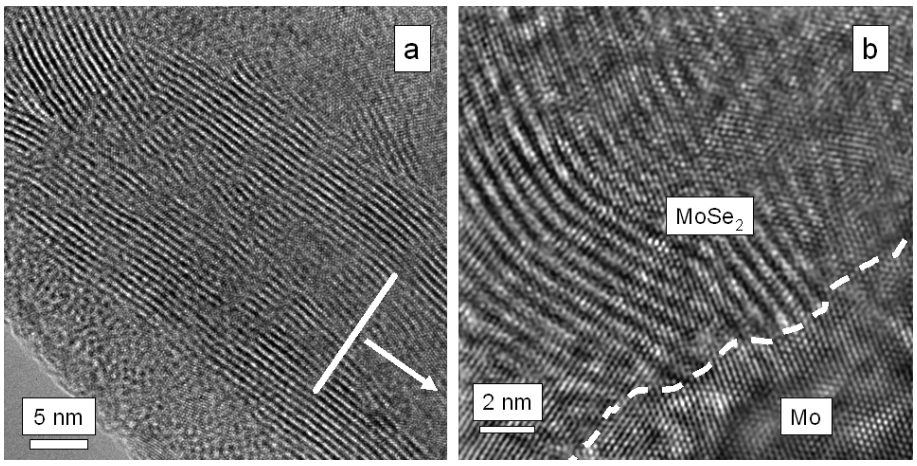

Figure 7.13: (a) High-resolution transmission electron micrograph of a $MoSe_2$ layer formed at 580 °C on single crystal Mo; the preferred orientation of the $MoSe_2$ layer is much more pronounced than that of $MoSe_2$ grown on polycrystalline Mo under the same conditions. The arrow indicates the direction to the interface, its orientation is given by the bar (b) High-resolution transmission electron micrograph of the interface between $MoSe_2$ and Mo oriented in [110]; the interface is indicated by a dashed line.

7.3.3 Effect of Na

As already mentioned in sections 1.5 and 5.2.2, Na affects the growth of several layers in CIGS solar cells and thus also the solar-cell performance. Considering the importance of the $MoSe_2$ layer and of its orientation, it is interesting to reveal whether Na has any impact on the $MoSe_2$ growth. While the selenization experiments for the previous sections was conducted by use of method (i), for the effect of Na, a selenization method with a considerably lower background pressure and also lower Se source temperature was chosen (method (ii), section 2.2.5). Thus, similar conditions as for the CIGS deposition in an MBE machine were obtained. The considerably smaller thickness of $MoSe_2$ layers in Mo/Si stacks selenized at 580 °C using method (ii) (see Table 7.1) may be traced back to the substantially lower Se source temperature in this process (section 2.2.5).

The RBS measurements reveal that for the Si/Mo and Si/NaF/Mo stacks selenized at 580 °C, the $MoSe_2$ thicknesses are considerably larger for the Na-free samples (see Table 7.1). The XRD patterns in Figs. 7.14a and b show the only peaks which can be related to $MoSe_2$ and indicate that the preferential growth of $MoSe_2$ in [10.0] and [11.0] is suppressed when Na is present in the samples. As mentioned above, the preferential $MoSe_2$ growth in [10.0] and [11.0] may facilitate the diffusion of Se through the already formed $MoSe_2$, thus leading to larger $MoSe_2$ thicknesses.
For the Si/Mo and Si/NaF/Mo stacks selenized at 450 °C, the XRD patterns in Fig. 7.14c show the only peaks which can be related to $MoSe_2$ and may indicate that, with increasing NaF thickness, the preferred orientation in [00.1] for $MoSe_2$ layers grown at 450 °C becomes more pronounced, i.e., the average orientation of the *c*-axis of the $MoSe_2$ layer appears to be perpendicular to the Mo surface. Also, the $MoSe_2$ layer thicknesses increase with increasing Na concentration (see Table 7.1).
HR-TEM images from $MoSe_2$/Mo interfaces of the $MoSe_2$/Mo/NaF(15nm)/Si stacks grown at 450 and 580 °C (Fig. 7.15) confirm the results obtained by XRD and show that for both samples, the *c*-axes of the $MoSe_2$ layers are in average perpendicular to the Mo surface. Also, the spacings between the layered structures of the $MoSe_2$ layers in both samples agree well with those of the 2H-$MoSe_2$ crystal structure. The 450 °C sample exhibits considerably larger Mo grain sizes (about 80-100 nm) than the 580 °C sample (about 10-20 nm), which may explain why only for the 450 °C sample, the XRD patterns in Fig. 7.14 indicate a preferential growth in [00.1], i.e., with a *c*-axis orientation in average perpendicular to the Mo surface (for very small Mo grains, the Mo surface roughness is quite enhanced, and thus, the XRD pattern of this sample indicates no preferential growth for the $MoSe_2$ layer, although its *c*-axis orientation is in average perpendicular to the Mo surface,

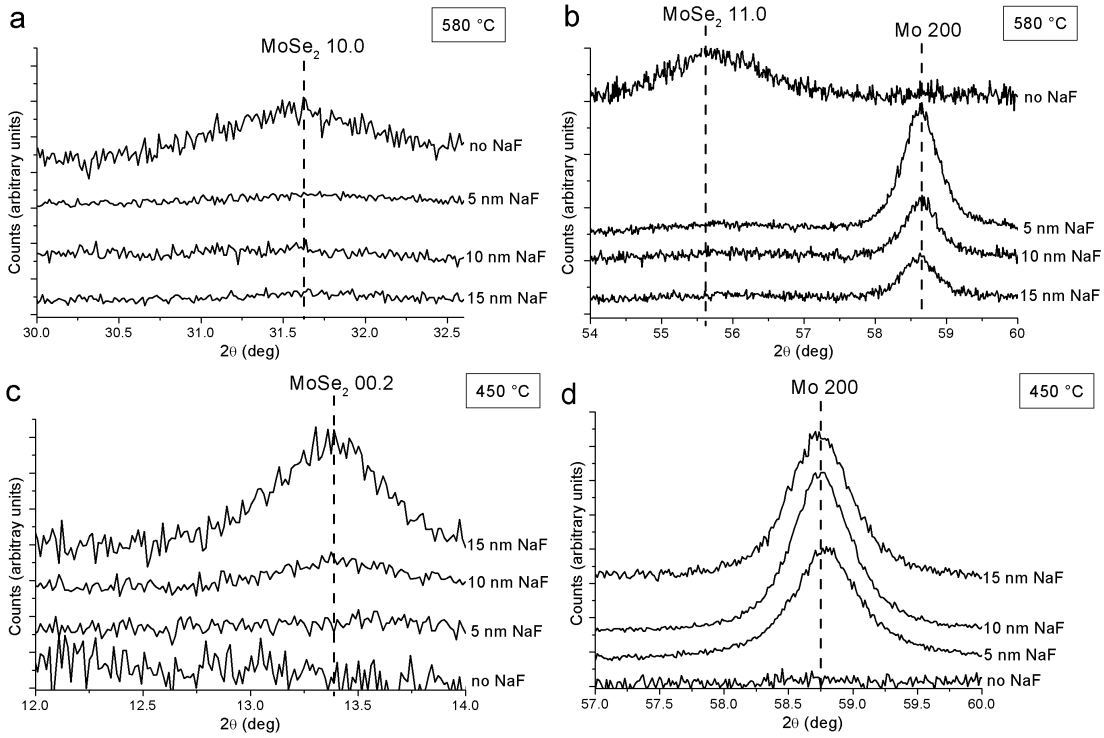

Figure 7.14: (a) and (b) XRD patterns of Si/Mo and Si/NaF/Mo stacks selenized at 580 °C. (c) and (d) XRD patterns of Si/Mo and Si/NaF/Mo stacks selenized at 450 °C. These patterns show the only peaks which can be related to $MoSe_2$ and to Mo {100} planes in a range from 5 to 90°.

as, e.g., shown for the 580 °C sample in Fig. 7.15). The $MoSe_2$ layer thickness of the 450 °C sample is everywhere about 20 nm, whereas the 580 °C sample shows $MoSe_2$ layer thicknesses varying between 4 and 20 nm.

For further considerations, it is important to point out that for the Na-containing samples, Na is probably present on the surface of the Mo layer prior to the $MoSe_2$ formation since the Mo/NaF/Si stacks are heated to 450 and 580 °C prior to the selenization, which may induce the dissociation of NaF into Na and F ions. Na normally shows a high mobility, especially along grain boundaries of the Mo layer. Bodegård et al. [144] provided an explanation for this behavior: Mo easily oxidizes, and Mo oxide phases are present at the Mo grain boundaries. These oxides, mainly MoO_3, may act as intercalation hosts for Na and thus may be responsible for the rapid diffusion and high solubility of Na in Mo thin films.
ERDA measurements on $MoSe_2$/Mo/NaF(15nm)/Si stacks grown at 450 and 580 °C (Fig. 7.16) reveal the presence of Na in these $MoSe_2$ layers. This suggests that Na diffuses from Mo into $MoSe_2$ during the $MoSe_2$ growth. From these ERDA

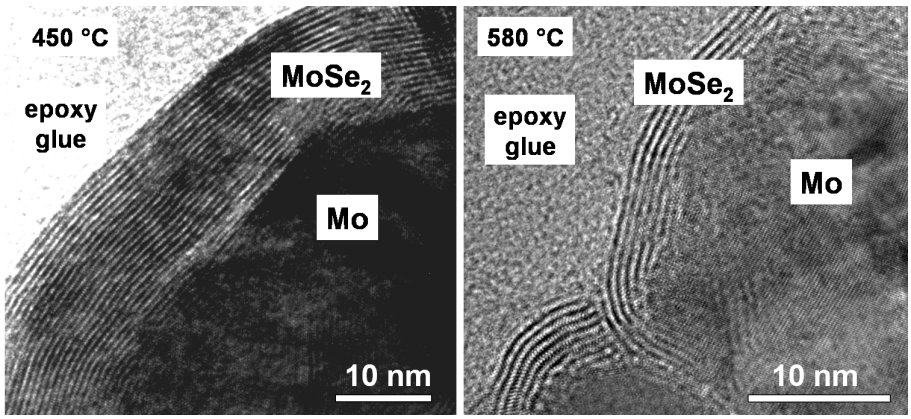

Figure 7.15: High-resolution transmission electron micrographs of $MoSe_2$/Mo interfaces. The Mo/NaF/Si stacks of these samples were selenized at 450 and 580 °C, and the NaF films had a thickness of 15 nm. The $MoSe_2$ layer thickness of the 450 °C sample is about 20 nm over the whole specimen, whereas the 580 °C sample shows $MoSe_2$ layer thicknesses ranging from 4 to 20 nm.

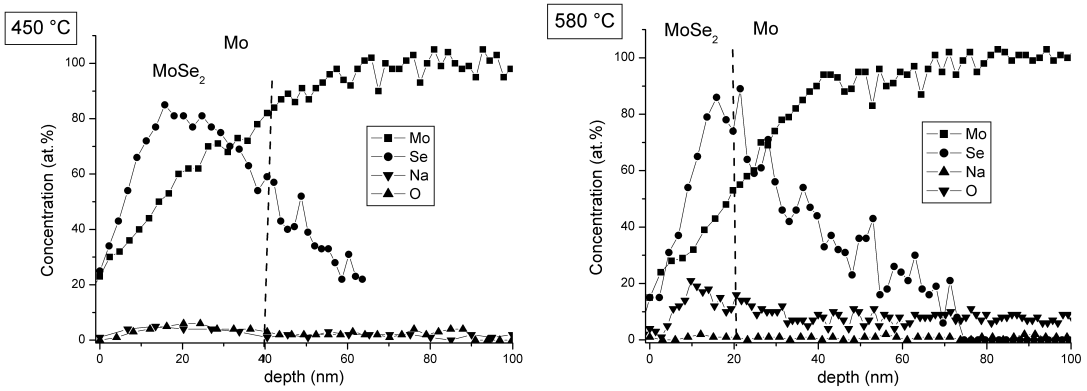

Figure 7.16: Depth profiles of Mo, Se, Na, and oxygen of $MoSe_2$/Mo/NaF(15nm)/Si stacks grown at 450 and 580 °C, obtained by elastic recoil detection analysis. By means of these measurements, the $MoSe_2$ layer thicknesses were determined to be 40 and 20 nm for samples grown at 450 and 580 °C (however, these thicknesses were much more accurately determined by means of TEM to be 20 nm and 4-20 nm; see Fig. 7.15.)

Table 7.2: Elemental concentrations in $MoSe_2$ and Mo layers of $MoSe_2$/Mo/15nm NaF/Si and $MoSe_2$/Mo/Si stacks grown at 450 and 580 °C, extracted from flight-time spectra obtained by elastic recoil detection analysis.

Sample	[O] (at.%) in $MoSe_2$	[O] (at.%) in Mo	[Na] (at.%) in $MoSe_2$	[Na] (at.%) in Mo
$MoSe_2$/Mo/Si grown at 450 °C	17	4	-	-
$MoSe_2$/Mo/15nm NaF/Si grown at 450 °C	5	3	5	1
$MoSe_2$/Mo/Si grown at 580 °C	3	5	-	-
$MoSe_2$/Mo/15nm NaF/Si grown at 580 °C	14	10	<1	1

measurements (summarized in Table 7.2), the Na concentrations in the $MoSe_2$ layers can be estimated to be about 5 at.% for the 450 and below 1 at.% for the 580 °C samples. Why the Na concentration is significantly larger in the 450 °C sample is not yet understood. It may be that at elevated temperatures, NaF dissociates, and both, Na and F ions, tend to diffuse along grain boundaries to the surface of the sample where they evaporate at a rate determined by the substrate temperature. Fluorine may evaporate to a much larger extent than Na. This assumption is supported by the fact that fluorine could not be found in the samples by means of ERDA measurements, thus, it is assumed that F is present in the samples only to a negligible extent ($\leq$ 0.01 at.%).

Apart from Na, also oxygen is found in these $MoSe_2$/Mo/NaF(15nm)/Si and also in the $MoSe_2$/Mo/Si stacks (Table 7.2) at considerable concentrations. For the samples grown at 450 °C, the oxygen concentration in the $MoSe_2$ and Mo layers is larger in the Na-free sample. This enhanced oxygen concentration may be one reason for the significantly smaller $MoSe_2$ thickness in case of the Na-free $MoSe_2$/Mo/Si stack: MoO_x formed at Mo grain boundaries and on the Mo surface may reduce considerably the amount of metallic Mo which may be selenized, i.e., it impedes the $MoSe_2$ growth kinetics.
But why is the $MoSe_2$ layer thickness for the 450 °C samples larger when Na is present? Apparently, Na may be more easily oxidized than Mo, thus increasing the amount of metallic Mo available for selenization.

For the $MoSe_2$/Mo/NaF(15nm)/Si and $MoSe_2$/Mo/Si stacks grown at 580 °C, exactly the opposite behavior as at 450 °C is found: the oxygen concentration in the $MoSe_2$ and Mo layers is larger in the Na-containing sample. This behavior gives, as in the case of the 450 °C sample, one reason for the significantly smaller $MoSe_2$ thickness in case of the stack with Na.
From the results obtained by RBS, XRD and HR-TEM (Table 7.1, Figs. 7.14 and 7.15), it appears that at 580 °C, the presence of Na affects a $MoSe_2$ growth with the *c*-axis of 2H-$MoSe_2$ oriented perpendicular to the Mo surface. Morales et al. [145] reported about a distortion of the 2H-$MoSe_2$ crystal structure induced by the intercalation of Na. By means of XRD measurements on Na-intercalated $MoSe_2$ crystals, these authors identified a phase transformation from 2H-$MoSe_2$ to 1T-Na_xMoSe_2 ($0.3 \leq x \leq 0.8$) upon the intercalation of Na (the lattice constant c increased from 1.29 nm to 1.51 nm). For the $MoSe_2$ layers shown in Fig. 7.15, such a phase transition can not be revealed. As already mentioned, the spacings of the layered structures of the $MoSe_2$ layers studied by means of TEM all agree well with those of the 2H-$MoSe_2$ crystal structure. Probably, the Na concentrations in the $MoSe_2$/Mo/NaF(15nm)/Si stacks are not sufficient to change the lattice constant c to a measurable extent. Still, the intercalating Na certainly may destabilize the 2H-$MoSe_2$ structure, which may explain the change in *c*-axis orientation from perpendicular to parallel with respect to the Mo surface.

The results obtained by XRD, HR-TEM and ERDA (Figs. 7.14, 7.15 and 7.16) indicate that the Mo/NaF(15nm)/Si stack selenized at 450 °C exhibits larger Mo grains and also a larger $MoSe_2$ layer thickness, compared with the 580 °C sample. That large oxygen concentrations lead to small Mo grain sizes has also been found by Scofield et al. [146]. It may be assumed that since Mo oxide phases are present at the Mo grain boundaries, a larger oxygen concentration leads to an increase of the grain-boundary density in Mo, i.e., to a decrease of the average grain size. In addition, Palm et al. [68] showed that that Cu(In,Ga)(S,Se)$_2$ absorbers formed on oxygen-rich Mo exhibited much thinner $MoSe_2$ layers, compared with those formed on oxygen poor Mo, which agrees well with the results presented here.

From Figs. 7.14b and d it is apparent that Mo grows in part preferentially in [100] direction when Na is present. It is not clear how Na may influence the texture of Mo, which regularly shows a preferential growth in [110] direction. According to the equilibrium Mo-Na phase diagram [138], an intermetallic Mo-Na phase does not exist. However, Martin et al. [147] reported that for Na-doped MoO_3, the coordination of Mo changes from octahedral to tetrahedral upon Na doping, i.e., the incorporation of Na in the MoO_3 lattice induces a phase transformation. Similar processes may also occur for MoO_3 - or generally MoO_x - phases, if present at Mo grain boundaries for the $MoSe_2$/Mo/NaF/Si stacks. Such a phase transformation

may be one explanation for the partly preferential growth of Mo in [100] direction for Na-containing samples as found by means of XRD.

It is interesting to note that for 2H-MoS_2, which exhibits a crystal structure similar to 2H-$MoSe_2$, Na intercalation also resulted in a considerable increase of the lattice parameter c, as revealed by Somoano et al. [148]. Moreover, the results shown by these authors indicate a large increase of the free electron density and a rise of the Fermi level induced by the intercalation of Na in 2H-MoS_2. This way, the electron-hole interaction is effectively screened by the increased electron density, and the excitons are disrupted. Therefore, these intercalated compounds can be considered to be metallic in nature [149].
Such a semiconductor-metal transition upon Na intercalation may also occur in 2H-$MoSe_2$ since both, 2H-$MoSe_2$ and 2H-MoS_2, exhibit similar energy-band structures (owing to similar crystal structures). This possible transition needs to be taken into account when characterizing the role of $MoSe_2$ as buffer layer between CIGS and any back contact.

7.4 Conclusions

The formation of $MoSe_2$ was studied on polycrystalline Mo layers and Mo single crystals in dependence of the substrate temperature, the Mo orientation and the Na concentration. For all $MoSe_2$, a hexagonal crystal structure was found. A $MoSe_2$ layer formed at 580 °C showed a homogeneous composition with the c-axis oriented parallel to the Mo substrate. For a substrate temperature of 580 °C, the diffusion constant of Se through $MoSe_2$ was estimated.
For substrate temperatures lower than about 550 °C, the $MoSe_2$ layer thickness remains rather small, whereas for substrate temperatures higher than 550 °C, the $MoSe_2$ layer thickness increases strongly with increasing temperature. It was shown that a $MoSe_2$ layer formed at 450 °C has a c-axis oriented preferably perpendicular to the Mo surface, whereas at 580 °C, the c-axis is oriented preferably parallel to the Mo surface. The smaller $MoSe_2$ layer thickness at 450 °C can be explained by a Se diffusion through $MoSe_2$ reduced by a c-axis orientation perpendicular to the Mo surface.
The orientation of the Mo substrate has no influence on the preferred orientation of $MoSe_2$. Also, Na was shown to induce a $MoSe_2$ growth with the c-axis oriented perpendicular to the Mo surface at 580 °C. For the 450 °C samples, it appears that Na reduces the oxygen concentration in Mo, probably because Na is more easily oxidized than Mo. Thus, the amount of metallic Mo is enhanced, which may lead to the larger $MoSe_2$ thicknesses found for samples with Na. In addition, both, the $MoSe_2$ layer thickness and the Mo grain size, are affected by the oxygen

concentration in Mo prior to the selenization.

First solar cells on ITO back contact with intentionally grown $MoSe_2$ intermediate layers showed clearly a better photovoltaic performance than without the $MoSe_2$ intermediate layer, and efficiencies of up to 11.8% were achieved in substrate configuration (Fig. 7.17). In addition, Matheis et al. [150] reported 13.4% efficiency solar cells on $MoSe_2$/ZnO:Al back contact. These and the present results indicate that $MoSe_2$ layers can be used as buffer layer for quasi-ohmic contact and to develop high-efficiency CIGS solar cells on, e.g., a TCO back contact.

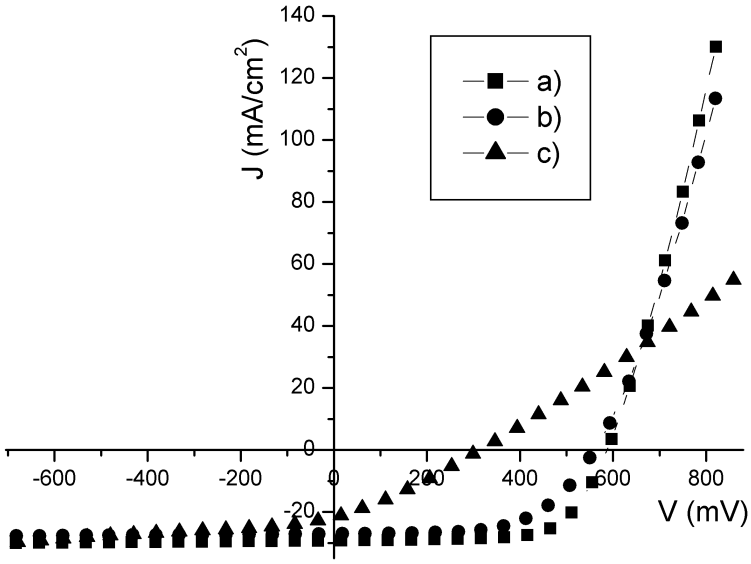

Figure 7.17: j-V characteristics under AM1.5 illumination of CIGS solar cells in substrate configuration with ITO/$MoSe_2$ back contact (a and b) and with ITO back contact (c). To form an intentionally grown $MoSe_2$ intermediate layer on ITO back contact, for cell (a) the Mo was selenized at 450 °C, for cell (b) at 580 °C for 30 min. Cell (c) was processed in the same run as cell (b), but covered during the selenization. The processing of these solar cells and the I-V measurements were kindly performed by D. Brémaud, Thin-Film Physics group, ETH Zurich, Switzerland.

Chapter 8

Concluding remarks and outlook

During the course of the present thesis, interfaces between CIGS and various buffer layers, as well as the growth of $MoSe_2$ as buffer-layer material between CIGS and any metal/semimetal back contact have been studied. In the following, a summary of the outcome and considerations on possible further studies of these layers and interfaces will be given.

- Within the scope of the present work, only the structural and chemical properties of CIGS/buffer interfaces have been studied. On the impacts of microstructural and chemical features at these interfaces (such as the formation of a Cu-depleted (and Cd- or In-enriched) Cu-(In,Ga)-Se layer) on the electronic properties of the *p*-*n* heterojunction certain assumptions have been made. Confirmation of these assumptions may be provided by measurements of the electrical properties of CIGS/buffer interfaces by means of, e.g., STM, SKPM or EBIC measurements (see section 1.6)

- Cu diffusion from CIGS into the buffer layer is a process which has been found to have occurred for all CIGS/buffer interfaces studied, not only for the CIGS/CdS and CIGS/In_xS_y interfaces presented here but also for CIGS/ZnSe and CIGS/Zn(O,S) interfaces (not shown here). The impact of Cu on the electrical and optical properties of the buffer is clear only in the case of CdS. Bube et al. [91] reported that Cu doping of CdS increases its photoconductivity which may affect the electronic properties of the CIGS/CdS heterojunction under illumination. For co-evaporated In_xS_y thin films, it was shown by Barreau et al. [103] that Cu reduces the band-gap energy of In_xS_y considerably. However, it is not clear how this reduction affects the solar-cell performance. In general, no information on the influence of Cu on the *p*-*n* heterojunction formation in CIGS/buffer systems is available. Further studies are thus necessary.

- As revealed at interfaces between CIGS and In_xS_y deposited by various techniques, for substrate temperatures during the In_xS_y deposition above about 250 °C, $CuIn_5S_8$ forms instead of In_xS_y. Since this formation has been found for different deposition methods, it appears to be a general phenomenon for CIGS/In_xS_y interfaces, independent of the deposition technique. Although the present assumptions based on structural and chemical analyses were sufficient to rationalize why the cells with $CuIn_5S_8$ show very bad solar-cell efficiencies, it would still be necessary to reveal the electrical properties of the $CuIn_5S_8$ layers and CIGS/$CuIn_5S_8$ interfaces of these cells. Furthermore, it was found that for interfaces between CIGS and In_2S_3 layers deposited by spray-ion layer gas reaction [151] - a non-vacuum technique, in contrast to ALD, evaporation or sputtering) - at 300 °C, no $CuIn_5S_8$ layer formed at the CIGS/In_2S_3 interface (results not shown in the present thesis). This result may indicate that impurities (such as oxygen) may affect the $CuIn_5S_8$ growth considerably and possibly impede its formation.

- Oxygen as impurity plays an important role in all of the buffer layers and CIGS/buffer systems studied in the frame of the present thesis. Barreau et al. [103] showed that oxygen leads to an increase in the band-gap energy of co-evaporated In_xS_y layers. Oxide phases in Mo and $MoSe_2$ layers appear to have a considerable impact on the growth of these layers, as mentioned in chapter 7 of the present thesis. Oxide phases have also been identified in CBD-CdS buffers (e.g., [152]), however, it is not yet clear how these phases affect the electrical properties of the CdS layer and thus the solar-cell performance. Further studies are thus required.

- The $MoSe_2$ growth under variation of divers parameters has been investigated. It is now partly understood how the substrate temperature affects the $MoSe_2$ growth and that the Mo orientation does not play any role. However, in order to apply $MoSe_2$ as buffer between CIGS and any metal/semimetal, variations of further parameters have to be performed and studied in order to control these in a base-line production: the influence of Cu, In and Ga on the $MoSe_2$ growth as well as the effects of the Se source temperature and the presence of Na. Although the latter parameter has already been studied in the present thesis, it is still not clear how Na influences the structural and electrical properties of $MoSe_2$. Also, different Na precursors or different ways to introduce Na into the system may lead to different properties of the $MoSe_2$ layer.

References

[1] A.E. Becquerel, "Mémoires sur les effêts électriques produits sous l'influence des rayons," *Comptes rendus de l'Academie Scientifique*, vol. 9, p. 561, 1839.

[2] W.G. Adams and R.E. Day, "The action of light on selenium," *Proc. Roy. Soc. London*, vol. 25, p. 113, 1876.

[3] D.M. Chapin, C.S. Fuller, and G.L. Pearson, "A new silicon p-n junction photocell for converting solar radiation into electrical power," *J. Appl. Phys.*, vol. 25, p. 676, 1954.

[4] SolarBuzz Europe, Inc., "Marketbuzz 2005: annual world solar photovoltaic (PV) market report," March 2005. Contact information: P.O. Box 767, Woking GU21 4AR, United Kingdom, info@solarbuzz.com.

[5] E.A. Alsema, "Energy Pay-back Time and CO_2 Emissions of PV Systems," *Prog. Photovolt. Res. Appl.*, vol. 8, p. 17, 2000.

[6] M.A. Green, K. Emery, D.L. King, S. Igari, and W. Warta, "Solar Cell Efficiency Table (Version 25)," *Prog. Photovolt. Res. Appl.*, vol. 13, p. 49, 2005.

[7] J. Parkes, R.D. Tomlinson, and M.J. Hampshire, "The fabrication of p and n type single crystals of $CuInSe_2$," *J. Cryst. Growth*, vol. 20, p. 315, 1973.

[8] J.L. Shay, S. Wagner, and H.M. Kaspar, "Efficient $CuInSe_2$/CdS solar cells," *Appl. Phys. Lett.*, vol. 27, no. 2, p. 89, 1975.

[9] L.L. Kazmerski, F.R. White, and G.K. Morgan, "Thin-film $CuInSe_2$-CdS heterojunction solar-cells," *Appl. Phys. Lett.*, vol. 29, no. 4, p. 268, 1976.

[10] A.M. Barnett and A. Rothwarf, "Thin-film solar cells; a unified analysis of their potential," *IEEE Trans. Elec. Dev.*, vol. ED-27, p. 615, 1980.

[11] J.J. Loferski, "Theoretical considerations governing the choice of the optimum semiconductor for photovoltaic solar energy conversion," *J. Appl. Phys.*, vol. 27, no. 7, p. 777, 1956.

[12] W. Shockley and H.J. Queisser, "Detailed balance limit of efficiency of *p-n* junction solar cells," *J. Appl. Phys.*, vol. 32, no. 3, p. 510, 1960.

[13] C.D. Mathers, "Upper limit of efficiency for photovoltaic solar-cells," *J. Appl. Phys.*, vol. 48, no. 7, p. 3181, 1977.

[14] P. Migliorato, J.L. Shay, H.M. Kasper, and S. Wagner, "Analysis of electrical and luminescent properties of $CuInSe_2$," *J. Appl. Phys.*, vol. 46, no. 4, p. 1777, 1975.

[15] W.S. Chen, J. M. Stewart, B. J. Stanbery, W. E. Devany, and R.A. Mickelsen, "Development of thin-film polycrystalline $CuIn_{1-x}Ga_xSe_2$ solar cells," in *Conference Record of the 19th IEEE Photovoltaic Specialists Conference, New Orleans, Lousiana, USA*, p. 1445, IEEE, New York, USA, 1987.

[16] C. Bellabarba and C. Rincon, "Temperature dependence of the fundamental absorption edge in $CuGaSe_2$," *Jpn. J. Appl. Phys., Suppl.*, vol. 32-3, p. 599, 1993.

[17] A.M. Gabor, J.R. Tuttle, D.S. Albin, M.A. Contreras, R. Noufi, and A.M. Hermann, "High-efficiency $CuIn_xGa_{1-x}Se_2$ solar cells made from $(In_x, Ga_{1-x})_2Se_3$ precursor films," *Appl. Phys. Lett.*, vol. 65, no. 2, p. 198, 1994.

[18] T. Dullweber, O. Lundbergb, J. Malmström, M. Bodegård, L. Stolt, U. Rau, H.W. Schock, and J.H. Werner, "Back surface band gap gradings in $Cu(In, Ga)Se_2$ solar cells," *Thin Solid Films*, vol. 387, p. 11, 2001.

[19] M.L. Fearhealey, "The phase relations in the Cu,In,Se systems and the growth of $CuInSe_2$ single crystals," *Solar Cells*, vol. 16, p. 91, 1986.

[20] R. Herberholz, U. Rau, H.W. Schock, T. Haalboom, T. Gödecke, F. Ernst, C. Beilharz, K.W. Benz, and D. Cahen, "Phase segregation, Cu migration and junction formation in $Cu(In, Ga)Se_2$," *Eur. Phys. J. AP*, vol. 6, p. 131, 1999.

[21] M. Krejci, *Preparation and characterization of heteroepitaxial $CuIn_xSe_y$ layers and $Cu(In, Ga)Se_2$ substrate solar cells.* PhD thesis, ETH Zurich, Switzerland, 1999.

[22] R.M. Burgess, W.S. Chen, W.E. Devaney, D.H. Doyle, N.P. Kim, and B.J. Stanberry, "Electron and proton radiation effects on GaAs and $CuInSe_2$ thin film solar cells," in *Conference Record of the 20th IEEE Photovoltaic Specialists Conference, Las Vegas, Nevada, USA*, p. 909, IEEE, New York, USA, 1988.

[23] B.M. Basol, V.K. Kapur, C.R. Leidholm, and A. Halani, "Flexible and light weight copper indium diselenide solar cells," in *Conference Record of the 25th IEEE Photovoltaic Specialists Conference, Washington D.C., USA*, p. 157, IEEE, Piscataway, New Jersey, USA, 1996.

[24] U. Rau, A. Jasenek, H.W. Schock, J. G. L. Roche, A. Robben, and K. Bogus, "Radiation induced defects in $Cu(In, Ga)Se_2$ solar cells - comparison of electron and proton irradiation," in *Conference Record of the 28th IEEE Photovoltaic Specialists Conference, Anchorage, Alaska, USA*, p. 1032, IEEE, Piscataway, New Jersey, USA, 2000.

[25] D. Brémaud, D. Rudmann, G. Bilger, H. Zogg, and A.N. Tiwari, "Towards the development of flexible CIGS solar cells on polymer films with efficiency exceeding 15%," in *Conference Record of the 31st IEEE Photovoltaic Specialists Conference, Lake Buena Vista, Florida, USA, 2005*, p. 223, IEEE, Piscataway, New Jersey, USA, 2005.

[26] A. Rockett and R.W. Birkmire, "$CuInSe_2$ for photovoltaic applications," *J. Appl. Phys.*, vol. 70, no. 7, p. R81, 1991.

[27] H.W. Schock and R. Noufi, "CIGS-based solar cells for the next millennium," *Prog. Photovolt. Res. Appl.*, vol. 8, p. 151, 2000.

[28] B.J. Stanbery, "Copper indium selenides and related materials for photovoltaic devices," *Critical Reviews in Solid State and Materials Sciences*, vol. 27, no. 2, p. 73, 2002.

[29] A. Romeo, M. Terheggen, D. Abou-Ras, D.L. Bätzner, F.-J. Haug, M. Kälin, D. Rudmann, and A.N. Tiwari, "Development of Thin-film $Cu(In, Ga)Se_2$ and CdTe Solar Cells," *Prog. Photovolt. Res. Appl.*, vol. 12, p. 93, 2004.

[30] M. Cardona, M. Weinstein, and G.A. Wolff, "Ultraviolet reflection spectrum of cubic CdS," *Phys. Rev.*, vol. 140, no. 2A, p. A633, 1965.

[31] M. Cardona and G. Harbeke, "Optical properties and band structure of wurtzite-type crystals and rutile," *Phys. Rev.*, vol. 137, no. 5A, p. A1467, 1965.

[32] R.R. Potter, C. Eberspacher, and L. Fabick, "Device analysis of $CuInSe_2$/(Cd,Zn)S/ZnO solar cells," in *Conference Record of the 18th IEEE Photovoltaic Specialists Conference, Las Vegas, Nevada, USA, 1985*, p. 1659, IEEE, New York, USA, 1985.

[33] K. Mitchell, C. Eberspacher, J. Ermer, and D. Pier, "Single and tandem junction $CuInSe_2$ cell and module technology," in *Conference record of the 20th IEEE Photovoltaic Specialists Conference, Las Vegas, Nevada, USA, 1988*, p. 1384, IEEE, New York, USA, 1988.

[34] W.Y. Liang and A.D. Yoffe, "Transmission spectra of ZnO single crystals," *Phys. Rev. Lett.*, vol. 20, no. 2, p. 59, 1968.

[35] P.O. Grabitz, U. Rau, and J.H. Werner, "Electronic inhomogeneities and the role of the intrinsic ZnO layer in $Cu(In, Ga)Se_2$ thin-film solar cells," in *Proceedings of the 20th European Photovoltaic Solar Energy Conference and Exhibition, Barcelona, Spain, 2005*, WIP Munich and ETA Florence, 2005. To be published.

[36] T. Minemoto, Y. Hashimoto, T. Satoh, T. Negami, H. Takakura, and Y. Hamakawa, "$Cu(In, Ga)Se_2$ solar cells with controlled conduction band offset of window $Cu(In, Ga)Se_2$ layers," *J. Appl. Phys.*, vol. 89, no. 12, p. 8327, 2001.

[37] U. Rau and H.W. Schock, "Electronic properties of $Cu(In, Ga)Se_2$ heterojunction solar cells - recent achievements, current understanding, and future challenges," *Appl. Phys. A*, vol. 69, p. 131, 1999.

[38] M.R. Kaelin, *Low-cost* $Cu(In, Ga)Se_2$ *absorbers from nanosized precursor materials for thin-film solar cells.* PhD thesis, ETH Zurich, Switzerland, 2005.

[39] J. Kessler, M. Ruckh, D. Hariskos, U. Rühle, R. Menner, and H.W. Schock, "Interface engineering between $CuInSe_2$ and ZnO," in *Conference Record of the 23rd IEEE Photovoltaic Specialists Conference, Louisville, Kentucky, USA, 1993*, p. 447, IEEE, New York, USA, 1993.

[40] A. Romeo, R. Gysel, S. Buzzi, D. Abou-Ras, D.L. Bätzner, D. Rudmann, F. Kurdesau, H. Zogg, and A.N. Tiwari, "Properties of CIGS solar cells developed with evaporated II-VI buffer layer," in *Technical Digest of the 14th International Photovoltaic Science and Engineering Conference, Bangkok, Thailand*, p. 705, 2004. To be published in Solar Energy Materials & Solar Cells.

[41] M. Rusu, T. Glatzel, C.A. Kaufmann, A. Neisser, S. Siebentritt, S. Sadewasser, T. Schedel-Niedrig, and M.Ch. Lux-Steiner, "High-efficient ZnO/PVD-CdS/Cu(In, Ga)Se_2 thin film solar cells: formation of the buffer-absorber interface and transport properties," *MRS Symp. Proc.*, vol. 865, p. F14.25.1, 2005.

[42] R.J. Matson, O. Jamjoum, A.D. Buonaquist, P.E. Russell, L.L. Kazmerski, P. Sheldon, and R.K. Ahrenkiel, "Metal contacts to $CuInSe_2$," *Solar Cells*, vol. 11, no. 301, 1984.

[43] K. Orgassa, H.W. Schock, and J.H. Werner, "Alternative back contact materials for thin-film Cu(In, Ga)Se_2 solar cells," *Thin Solid Films*, vol. 431-432, p. 387, 2003.

[44] P.E. Russell, O. Jamjoum, R.K. Ahrenkiel, L.L. Kazmerski, R.A. Mickelsen, and W.S. Chen, "Properties of the Mo-$CuInSe_2$ interface," *Appl. Phys. Lett.*, vol. 40, no. 11, p. 995, 1982.

[45] W.N. Shafarman and J.E. Phillips, "Direct current-voltage measurements of the Mo/$CuInSe_2$ contact on operating solar cells," in *Conference Record of the 25th IEEE Photovoltaic Specialists Conference, Washington D.C., USA, 1996*, p. 917, IEEE, Piscataway, New Jersey, 1996.

[46] T. Wada, N. Kohara, T. Negami, and M. Nishitani, "Chemical and structural characterization of Cu(In, Ga)Se_2/Mo interface in Cu(In, Ga)Se_2solar cells," *Jpn. J. Appl. Phys.*, vol. 35, p. L1253, 1996.

[47] T. Wada, N. Kohara, S. Nishiwaki, and T. Negami, "Characterization of the Cu(In, Ga)Se_2/Mo interface in CIGS solar cells," *Thin Solid Films*, vol. 387, p. 118, 2001.

[48] T. Kubart, T. Polcar, L. Kopecký, R. Novák, and D. Nováková, "Temperature dependence of tribological properties of MoS_2 and $MoSe_2$ coatings," *Surf. Coat. Techn.*, vol. 193, p. 230, 2005.

[49] J. Wennerberg, J. Kessler, M. Bodegård, and L. Stolt, "Damp heat testing of high performance CIGS thin film solar cells," in *Proceedings of the 2nd World Conference on Photovoltaic Energy Conversion, Vienna, Austria, 1998* (J. Schmid, H.A. Ossenbrink, P. Helm, H. Ehmann, and E.D. Dunlop, eds.), p. 1161, Office for Official Publications of the European Communities, Luxembourg, 1998.

[50] P.J. Rostan, J. Mattheis, G. Bilger, U. Rau, and J.H. Werner, "Formation of transparent and ohmic ZnO:Al/$MoSe_2$ contacts for bifacial Cu(In, Ga)Se_2

solar cells and tandem structures," *Thin Solid Films*, vol. 480-481, p. 67, 2005.

[51] K. Granath, L. Stolt, M. Bodegård, A. Rockett, and D. Schroeder, "Sodium in sputtered Mo back contacts for $Cu(In, Ga)Se_2$ devices: incorporation, diffusion and relationship to oxygen," in *Proceedings of the 14th European Photovoltaic Solar Energy Conference, Barcelona, Spain, 1997* (H.A. Ossenbrink, P. Helm, and H. Ehmann, eds.), p. 1278, Stephens & Associates, Bedford, 1997.

[52] A. Rockett, K. Granath, S. Asher, M.M. Al-Jassim, F. Hasoon, R. Matson, B. Basol, V.K. Kapur, J.S. Britt, T. Gillspie, and C. Marshall, "Na incorporation in Mo and $CuInSe_2$ from production processes," *Sol. En. Mat. Sol. Cells*, vol. 59, p. 255, 1999.

[53] J. Hedström, H. Ohlsen, M. Bodegård, A. Kylner, L. Stolt, D. Hariskos, M. Ruckh, and H.W. Schock, "$ZnO/CdS/Cu(In, Ga)Se_2$ thin film solar cells with improved performance," in *Conference record of the 23rd IEEE Photovoltaic Specialists Conference, Louisville, Kentucky, USA, 1993*, p. 364, IEEE, New York, USA, 1993.

[54] J. Holz, F. Karg, and H. v. Philipsborn, "The effect of substrate impurities on the electronic conductivity in CIS thin films," in *Proceedings of the 12th European Photovoltaic Solar Energy Conference, Amsterdam, The Netherlands, 1994* (R. Hill, W. Palz, and P. Helm, eds.), vol. 2, p. 1592, Stephens & Associates, Bedford, 1994.

[55] M.A. Contreras, B. Egaas, P. Dippo, J. Webb, J. Granata, K. Ramanathan, S. Asher, A. Swartzlander, and R. Noufi, "On the role of Na and modifications to $Cu(In, Ga)Se_2$ absorber materials using thin-MF (M=Na, K, Cs) precursor layers," in *Conference Record of the 26th IEEE Photovoltaic Specialists Conference, Anaheim, California, USA, 1996*, p. 359, IEEE, Piscataway, New Jersey, USA, 1996.

[56] D. Rudmann, *Effects of sodium on growth properties of $Cu(In, Ga)Se_2$ thin films and solar cells*. PhD thesis, ETH Zurich, Switzerland, 2004.

[57] C.H. Henry, K. Nassau, and J.W. Shiever, "Double-donor-acceptor pair lines and the chemical identification of the I_1 lines in CdS," *Phys. Rev. Lett.*, vol. 24, no. 15, p. 820, 1970.

[58] C. Heske, D. Eich, R. Fink, E. Umbach, S. Kakar, T. van Buuren, C. Bostedt, L.J. Terminello, M.M. Grush, T.A. Callcott, F.J. Himpsel, D.L. Ederer,

R.C.C. Perera, W. Riedl, and F. Karg, "Localization of Na impurities at the buried CdS/Cu(In, Ga)Se_2 heterojunction," *Appl. Phys. Lett.*, vol. 75, no. 14, p. 2082, 1999.

[59] N. Barreau, J.C. Bernède, and S. Marsillac, "Study of the new β-In_2S_3 containing Na thin films. Part II: Optical and electrical characterization of thin films," *J. Cryst. Growth*, vol. 241, p. 51, 2002.

[60] J. Sterner, J. Malmström, and L. Stolt, "Study on ALD In_2S_3/Cu(In, Ga)Se_2 interface formation," *Prog. Photovolt. Res. Appl.*, vol. 13, p. 179, 2005.

[61] D. Eich, U. Herber, U. Groh, U. Stahl, C. Heske, M. Marsi, M. Kiskinova, W. Riedl, R. Fink, and E. Umbach, "Lateral inhomogeneities of Cu(In, Ga)Se_2 absorber films," *Thin Solid Films*, vol. 361, p. 258, 2000.

[62] C.-S. Jiang, R. Noufi, K. Ramanathan, H.R. Moutinho, and M.M. Al-Jassim, "Electrical modification in Cu(In, Ga)Se_2 thin films by chemical bath deposition process of CdS films," *J. Appl. Phys.*, vol. 97, no. 5, p. 053701, 2005.

[63] A. Klein, W. Jaegermann, J. Fritsche, R. Hunger, D. Kraft, F. Säuberlich, T. Schulmeyer, and B. Späth, "Interfaces in thin film solar cells," in *Conference Record of the 31st IEEE Photovoltaic Specialists Conference, Lake Buena Vista, Florida, USA, 2005*, p. 205, IEEE, Piscataway, New Jersey, USA, 2005.

[64] K. Ramanathan, R. Noufi, J. Granata, J. Webb, and J. Keane, "Prospects for in situ junction formation in $CuInSe_2$ based solar cells," *Sol. En. Mat. Sol. Cells*, vol. 55, p. 15, 1998.

[65] M.J. Romero, M.M. Al-Jassim, R.G. Dhere, F.S. Hasoon, M.A. Contreras, T.A. Gessert, and H.R. Moutinho, "Beam injection methods for characterizing thin-film solar cells," *Prog. Photovolt. Res. Appl.*, vol. 10, no. 7, p. 445, 2002.

[66] J.T. Heath, J.D. Cohen, and W.N. Shafarman, "Bulk and metastable defects in $CuIn_{1-x}Ga_xSe_2$ thin films using drive-level capacitance profiling," *J. Appl. Phys.*, vol. 95, no. 3, p. 1000, 2004.

[67] M. Bodegård and L. Stolt, "The influence of sodium on the grain structure of $CuInSe_2$ films for photovoltaic applications," in *Proceedings of the 12th European Photovoltaic Solar Energy Conference, Amsterdam, The Netherlands*, vol. 2, p. 1743, Stephens & Associates, Bedford, 1994.

[68] J. Palm, V. Probst, A. Brummer, W. Stetter, R. Tölle, T.P. Niesen, S. Visbeck, O. Hernandez, M. Wendl, H. Vogt, H. Calwer, B. Freienstein, and F. Karg, "CIS module pilot processing applying concurrent rapid selenization and sulfurization of large area thin film precursors," *Thin Solid Films*, vol. 431-432, p. 514, 2003.

[69] M. Powalla, B. Dimmler, R. Schaeffler, G. Voorwinden, U. Stein, H.-D. Mohring, F. Kessler, and D. Hariskos, "CIGS solar modules: Progress in pilot production, new developments and applications," in *Proceedings of the 19th European Photovoltaic Solar Energy Conference and Exhibition, Paris, France, 2004* (W. Hoffmann, J.-L. Bal, H. Ossenbrink, W. Palz, and P. Helm, eds.), p. 1663, WIP-Munich and ETA-Florence, 2004.

[70] D. Lincot and R. Ortega Borges, "Chemical bath deposition of cadmium sulfide thin films. *In situ* growth and structural studies by combined quartz microbalance and electrochemical impedance techniques," *J. Electrochem. Soc.*, vol. 139, no. 7, p. 1880, 1992.

[71] A. Strohm, L. Eisenmann, R.K. Gebhardt, A. Harding, T. Schlötzer, D. Abou-Ras, and H.W. Schock, "ZnO/In_xS_y/Cu(In, Ga)Se_2 solar cells fabricated by coherent heterojunction formation," *Thin Solid Films*, vol. 480-481, p. 162, 2005.

[72] T. Gödecke and K. Schubert, "On the phase diagram InS_M," *Z. Metallkde.*, vol. 76, p. 358, 1985.

[73] D. Hariskos, R. Menner, E. Lotter, S. Spiering, and M. Powalla, "Magnetron sputtering of indium sulfide as the buffer layer in Cu(In, Ga)Se_2-based solar cells," in *Proceedings of the 20th European Photovoltaic Solar Energy Conference and Exhibition, Barcelona, Spain, 2005*, WIP Munich and ETA Florence, 2005. To be published.

[74] D. Williams and C. Carter, *Transmission electron microscopy. A textbook for materials science.* Plenum Press, New York, 1996.

[75] C. Meyer, D. Hauge, and the GATAN software team. Gatan Inc., 5933 Coronado Lane, Pleasanton, CA, USA.

[76] L.R. Doolittle, "A semiautomatic algorithm for Rutherford backscattering analysis," *Nucl. Instrum. Methods*, vol. B15, p. 227, 1986.

[77] J. Kessler, K.O. Velthaus, M. Ruckh, R. Laichinger, and H.W. Schock, "Chemical bath deposition of CdS on $CuInSe_2$ etching effects and growth kinetics," in *Proceedings of the 6th International Photovoltaic Science and*

Engineering Conference, New Delhi, India, 1992 (B.K. Das and S.N. Singh, eds.), p. 1005, 1992.

[78] D. Lincot, R. Ortega-Borges, J. Vedel, M. Ruckh, J. Kessler, K.O. Velthaus, D. Hariskos, and H.W. Schock, "Chemical bath deposition of CdS on $CuInSe_2$, combining dry and wet processes for high efficiency thin-film solar cells," in *Proceedings of the 11th European Photovoltaic Solar Energy Conference, Montreux, Switzerland, 1992* (W. Palz, C. De Reyff, H. Kiess, P. Helm, and L. Guimarães, eds.), p. 870, 1992.

[79] D. Schmid, M. Ruckh, F. Grunwald, and H.W. Schock, "Chalcopyrite/defect chalcopyrite heterojunctions on the basis of $CuInSe_2$," *J. Appl. Phys.*, vol. 73, p. 2902, 1993.

[80] A. Kylner, "The chemical bath deposited $CdS/Cu(In, Ga)Se_2$ interface as revealed by X-Ray photoelectron spectroscopy," *J. Electrochem. Soc.*, vol. 146, no. 5, p. 1816, 1999.

[81] C. Palache, H. Berman, and C. Frondel, *The system of mineralogy.* Wiley, New York, 7th ed., 1958.

[82] R.J. Traill and R.W. Boyle, "Hawleyite, isometric cadmium sulphide, a new mineral," *Am. Mineral.*, vol. 40, p. 555, 1955.

[83] T. Wada, "Microstructural characterization of high-efficiency $Cu(In, Ga)Se_2$ solar cells," *Sol. En. Mat. Sol. Cells*, vol. 49, p. 249, 1997.

[84] J.S. Chen, E. Kolawa, C.M. Garland, and M.-A. Nicolet, "Microstructure of polycrystalline $CuInSe_2$/Cd(Zn)S heterojunction solar cells," *Thin Solid Films*, vol. 219, p. 183, 1992.

[85] M.J. Furlong, M. Froment, M.C. Bernard, R. Cortès, A.N. Tiwari, M. Krejci, H. Zogg, and D. Lincot, "Aqueous solution epitaxy of CdS layers on $CuInSe_2$," *J. Cryst. Growth*, vol. 193, p. 114, 1998.

[86] V. Nadenau, D. Hariskos, H.W. Schock, M. Krejci, F.-J. Haug, A.N. Tiwari, H. Zogg, and G. Kostorz, "Microstructural study of the $CdS/CuGaSe_2$ interfacial region in $CuGaSe_2$ thin film solar cells," *J. Appl. Phys.*, vol. 85, no. 1, p. 534, 1999.

[87] T. Nakada, "Nano-structural investigations on Cd-doping into $Cu(In, Ga)Se_2$ thin films by chemical bath deposition process," *Thin Solid Films*, vol. 361-362, p. 346, 2000.

[88] C.-Y. Yeh, Z.W. Lu, S. Froyen, and A. Zunger, "Zincblende - wurtzite polytypism in semiconductors," *Phys. Rev. B*, vol. 46, no. 16, p. 10086, 1992.

[89] G. Hug, A. Loiseau, and P. Veyssiére, "Weak-beam observation of a dissociation transition in TiAl," *Philos. Mag. A*, vol. 57, p. 499, 1988.

[90] K.S. Knight, "The crystal structures of $CuInSe_2$ and $CuInTe_2$," *Mat. Res. Bull.*, vol. 27, no. 2, p. 161, 1992.

[91] R.H. Bube, *Photoconductivity in solids.* Wiley, New York, 1960.

[92] C.-S. Jiang, F.S. Hasoon, H.R. Moutinho, H.A. Al-Thani, M.J. Romero, and M.M. Al Jassim, "Direct evidence of a buried homojunction in $Cu(In, Ga)Se_2$ solar cells," *Appl. Phys. Lett.*, vol. 82, no. 1, p. 127, 2003.

[93] T. Wada, S. Hayashi, Y. Hashimoto, S. Nishiwaki, T. Sato, T. Negami, and M. Nishitani, "High efficiency $Cu(In, Ga)Se_2$ (CIGS) solar cells with improved CIGS surface," in *Proceedings of the 2nd World Conference and Exhibition on Photovoltaic Energy Conversion, Vienna, Austria* (J. Schmid, H.A. Ossenbrink, P. Helm, H. Ehmann, and E.D. Dunlop, eds.), p. 403, 1998.

[94] N. Romeo, A. Bosio, V. Canevari, R. Tedeschi, S. Sivelli, A. Romeo, and F.V. Kurdesau, "Development of a novel precursor for the preparation by selenization of high efficiency $Cu(In, Ga)Se_2$/CdS thin film solar cells," in *Proceedings of the 19th European Photovoltaic Solar Energy Conference and Exhibition, Paris, France, 2004* (W. Hoffmann, J.-L. Bal, H. Ossenbrink, W. Palz, and P. Helm, eds.), p. 1796, WIP Munich and ETA Florence, 2004.

[95] N. Naghavi, S. Spiering, M. Powalla, B. Canava, and D. Lincot, "High-efficiency copper indium gallium diselenide (CIGS) solar cells with indium sulfide buffer layers deposited by atomic layer chemical vapor deposition (ALCVD)," *Prog. Photovolt.*, vol. 11, p. 437, 2003.

[96] S. Gall, N. Barreau, S. Harel, J.C. Bernède, and J. Kessler, "Material analysis of PVD-grown indium sulphide buffer layers for $Cu(In, Ga)Se_2$-based solar cells," *Thin Solid Films*, vol. 480-481, p. 138, 2005.

[97] N. Naghavi, R. Henriquez, V. Laptev, and D. Lincot, "Growth studies and characterisation of In_2S_3 thin films deposited by atomic layer deposition (ALD)," *Appl. Surf. Sci.*, vol. 222, p. 65, 2004.

[98] H. Hahn and W. Klingler, "Über die Kristallstrukturen des In_2S_3 and In_2Te_3," *Z. anorg. Chem.*, vol. 260, p. 97, 1949.

[99] F. Py, M. Womes, J. Durand, J. Olivier-Fourcade, J.C. Jumas, J.M. Esteva, and R.C. Karnatak, "Copper in In_2S_3: a study by X-ray diffraction, diffuse reflectance and X-ray absorption," *J. Alloys. Comp.*, vol. 178, p. 297, 1992.

[100] K. Granath, M. Bodegård, and L. Stolt, "The effect of NaF on $Cu(In, Ga)Se_2$ thin film solar cells," *Sol. En. Mat. Sol. Cells*, vol. 60, p. 279, 2000.

[101] A. Rockett, J.S. Britt, T. Gillespie, C. Marshall, M.M. Al Jassim, F. Hasoon, R. Matson, and B. Basol, "Na in selenized $Cu(In, Ga)Se_2$ on Na-containing and Na-free glasses: distribution, grain structure, and device performances," *Thin Solid Films*, vol. 372, p. 212, 2000.

[102] D. Rudmann, A.F. da Cunha, M. Kaelin, F. Kurdesau, H. Zogg, and A.N. Tiwari, "Efficiency enhancement of $Cu(In, Ga)Se_2$ solar cells due to post-deposition Na incorporation," *Appl. Phys. Lett.*, vol. 84, no. 7, p. 1129, 2004.

[103] N. Barreau, J. Bernède, and J. Kessler, "Influence of oxygen, sodium and copper on the properties of PVD-grown indium sulfide," in *Proceedings of the 19th European Photovoltaic Solar Energy Conference and Exhibition, Paris, France* (W. Hoffmann, J.-L. Bal, H. Ossenbrink, W. Palz, and P. Helm, eds.), p. 223, WIP Munich and ETA Florence, 2004.

[104] N. Naghavi, J.-F. Guillemoles, D. Lincot, B. Canava, A. Etcheberry, S. Taunier, S. Spiering, M. Powalla, L. Legras, and M. Lamirand, "Analysis of high efficiency cadmium free CIGS solar cells with indium sulfide buffer layers deposited by atomic layer chemical vapor deposition," in *Proceedings of the 19th European Photovoltaic Solar Energy Conference and Exhibition, Paris, France* (W. Hoffmann, J.-L. Bal, H. Ossenbrink, W. Palz, and P. Helm, eds.), p. 1772, WIP Munich and ETA Florence, 2004.

[105] N. Naghavi, S. Spiering, M. Powalla, B. Canava, A. Taisne, J.-F. Guillemoles, S. Taunier, A. Etcheberry, and D. Lincot, "Towards better understanding of high efficiency Cd-free CIGS solar cells using atomic layer deposited indium sulfide buffer layers," *Mat. Res. Soc. Symp. Proc.*, vol. 763, p. B9.9.1, 2003.

[106] S. Spiering, D. Hariskos, M. Powalla, N. Naghavi, and D. Lincot, "Cd-free $CuIn(S, Se)_2$ thin-film solar modules with In_2S_3 buffer layer by ALCVD," *Thin Solid Films*, vol. 431-432, p. 359, 2003.

[107] G.A. Steigmann, H.H. Sutherland, and J. Goodyear, "Crystal structure of beta-In_2S_3," *Acta Cryst.*, vol. 19, no. 6, p. 967, 1965.

[108] W.J. Duffin and J.H.C. Hogg, "Crystalline phases in the system In-In_2S_3," *Acta Cryst.*, vol. 20, no. 4, p. 566, 1966.

[109] J.I. Pankove, *Optical processes in semiconductors.* Prentice Hall, Inc., Englewood Cliffs, New Jersey, 1971.

[110] R. Nomura, K. Konishi, and H. Matsuda, "Single-source organometallic chemical vapour deposition process for sulphide thin films: introduction of a new organometallic precursor $Bu^nIn(SPr^i)2$ and preparation of In_2S_3 thin films," *Thin Solid Films*, vol. 198, p. 339, 1991.

[111] T. Asikainen, M. Ritala, and M. Leskelä, "Growth of In_2S_3 thin films by atomic layer epitaxy," *Appl. Surf. Sci.*, vol. 82/83, p. 122, 1994.

[112] C. Guillén, T. Garc'ia, J. Herrero, M.T. Gutiérrez, and F. Briones, "Tailoring growth conditions for modulated flux deposition of In_2S_3 thin films," *Thin Solid Films*, vol. 451-452, p. 112, 2004.

[113] W.-T. Kim and C.-D. Kim, "Optical energy band gaps for β-In_2S_3thin-films deposited by spray pyrolysis," *J. Appl. Phys.*, vol. 60, no. 7, p. 2631, 1986.

[114] T. Nishino and Y. Hamakawa, "Preparation and properties of InS single crystals," *Jpn. J. Appl. Phys.*, vol. 16, no. 8, p. 1291, 1977.

[115] U. Rau, D. Braunger, R. Herberholz, H.W. Schock, J.-F. Guillemoles, L. Kronik, and D. Cahen, "Oxygenation and air-annealing effects on the electronic properties of $Cu(In, Ga)Se_2$ films and devices," *J. Appl. Phys.*, vol. 86, p. 497, 1999.

[116] A.G. Fitzgerald and G. Thomas, "Electron microscope observations of twinning and phase transformations in indium sulfide crystals," *Phys. Stat. Sol.*, vol. 25, p. 263, 1968.

[117] N. Barreau, J.C. Bernède, S. Marsillac, C. Amory, and W.N. Shafarman, "New Cd-free buffer layer deposited by PVD: In_2S_3 containing Na compounds," *Thin Solid Films*, vol. 431-432, p. 326, 2003.

[118] N.A. Allsop, A. Schönmann, H.-J. Muffler, M. Bär, M.C. Lux-Steiner, and C.-H. Fischer, "Spray-ILGAR indium sulfide buffers for $Cu(In,Ga)(S,Se)_2$ solar cells," *Prog. Photovolt: Res. Appl.*, 2005. In press.

[119] A. Usujima, S. Takeuchi, S. Endo, and T. Irie, "Optical and electrical properties of $CuIn_5S_8$ and $AgIn_5S_8$ single crystals," *Jpn. J. Appl. Phys.*, vol. 20, p. L505, July 1981.

[120] T. Walter and H. W. Schock, "Structural and electrical investigations of the anion exchange in polycrystalline $CuIn(S, Se)_2$ thin films," *Jpn. J. Appl. Phys., Suppl.*, vol. 32-3, p. 116, 1993.

[121] J.J.M. Binsma, L.J. Giling, and J. Bloem, "Phase relations in the system Cu_2S-In_2S_3," *J. Cryst. Growth*, vol. 50, p. 429, 1980.

[122] F.O. Adurodija, J. Song, S.D. Kim, S.K. Kim, and K.H. Yoon, "Characterization of $CuInS_2$ thin films grown by close-spaced vapor sulfurization of co-sputtered Cu-In alloy precursors," *Jpn. J. Appl. Phys.*, vol. 37, no. 8, p. 4248, 1998.

[123] N.S. Orlova, I.V. Bodnar, and E.A. Kudritskaya, "Crystal Growth and Properties of the $CuIn_5S_8$ and $AgIn_5S_8$ Compounds," *Cryst. Res. Techn.*, vol. 33, no. 1, p. 37, 1998.

[124] L. Gastaldi and L. Scaramuzza, "Single-crystal structure analysis of the spinel copper pentaindium octasulphide," *Acta Cryst. B*, vol. 36, p. 2751, 1980.

[125] A. Likforman, M. Guittard, A. Tomas, and J. Flahaut, "Mise évidence d'une solution solide de type spinelle dans le diagramme de phase du systeme In-S," *J. Solid State Chem.*, vol. 34, p. 353, 1980.

[126] Y. Ohmuro, T. Ohachi, and I. Taniguchi, "Ionic conduction of Ag^+ and Cu^+ ions in vacancy defect spinel compounds $(MIn_5S_8)_{1-x}(In_2S_3)_x$ (M = Cu or Ag, x < 1) in microwave regime," *Solid State Ionics*, vol. 79, p. 53, 1995.

[127] S.C. Abrahams and J.L. Bernstein, "Piezoelectric nonlinear optic $CuGaSe_2$ and $CdGeAs_2$: Crystal structure, chalcopyrite microhardness, and sublattice distortion," *J. Phys. Chem.*, vol. 61, no. 3, p. 1140, 1974.

[128] N. Barreau, S. Marsillac, and J.C. Bernède, "Physico-chemical characterization of β-In_2S_3 thin films synthesized by solid-state reaction, induced by annealing, of the constituents sequentially deposited in thin layers," *Vacuum*, vol. 56, p. 101, 2000.

[129] N. Kamoun, S. Belgacem, M. Amlouk, R. Bennaceur, J. Bonnet, F. Touhari, M. Nouaoura, and L. Lassabatere, "Structure, surface composition, and electronic properties of β-In_2S_3 and β-$In_{2-x}Al_xS_3$," *J. Appl. Phys.*, vol. 89, no. 5, p. 2766, 2001.

[130] C. Heske, R. Fink, E. Umbach, W. Riedl, and F. Karg, "Na-induced effects on the electronic structure and composition of $Cu(In, Ga)Se_2$ thin-film surfaces," *Appl. Phys. Lett.*, vol. 68, no. 24, p. 3431, 1996.

[131] F.-J. Haug, D. Rudmann, A. Romeo, H. Zogg, and A.N. Tiwari, "Electrical properties of the heterojunction in $Cu(In, Ga)Se_2$ superstrate solar cells," in

Proceedings of the 3rd World Conference on Photovoltaic Energy Conversion, Osaka, Japan, 2003 (K. Kurokawa, L. Kazmerski, B. McNelis, M. Yamaguchi, C. Wronski, and W. Sinke, eds.), p. 2853, Arisumi Printing Inc., Japan, 2003.

[132] D. Ohmori, T. Tokado, and T. Nakada, "$Cu(In_{1-x}, Ga_x)Se_2$ thin film solar cells using indium tin oxide back contacts fabricated by different deposition processes," in *Technical Digest of the 14th International Photovoltaic Science and Engineering Conference, Bangkok, Thailand, 2004* (?, ed.), p. 605, ?, 2004. to be published in Solar Energy Materials & Solar Cells.

[133] T. Nakada, Y. Hirabayashi, and T. Tokado, "$Cu(In_{1-x}, Ga_x)Se_2$-based thin film solar cells using transparent conducting back contacts," *Jpn. J. Appl. Phys.*, vol. 41, no. 11A, p. L1209, 2002.

[134] M. Terheggen, H. Heinrich, G. Kostorz, A. Romeo, D. Baetzner, A. Bosio, and A.N. Tiwari, "Structural and chemical interface characterization of CdTe solar cells by transmission electron microscopy," *Thin Solid Films*, vol. 431-432, p. 262, 2003.

[135] M.K. Agarwal and T. Talele, "Growth conditions and structural characterization of molybdenum sulphoselenide single crystals: (MoS_xSe_{2-x}, $0 \leq x \leq 2$)," *Mater. Res. Bull.*, vol. 20, p. 329, 1985.

[136] J.E. Dutrizac, "Reaction of Se vapor with molybdenum metal," *Canadian Metallurgical Quaterly*, vol. 10, no. 2, p. 115, 1971.

[137] N. Wakatsuki and Y. Sasaki, "Kinetics and diffusing species of the high-temperature selenidization of molybdenum," *Bull. Chem. Soc. Jpn.*, vol. 67, no. 5, p. 1290, 1994.

[138] L. Brewer and R.H. Lamoreaux, *Atomic Energy Review, Special issue No. 7. Molybdenum: physico-chemical properties of its compounds and alloys*, ch. Phase diagrams, p. 319. International Atomic Energy Agency, Vienna, 1980.

[139] L. Fister and D.C. Johnson, "Controlling solid-state reaction mechanisms using diffusion length in ultra-thin superlattice composites," *J. Am. Chem. Soc.*, vol. 114, p. 4639, 1992.

[140] S. Nishiwaki, N. Kohara, T. Negami, M. Nishitani, and T. Wada, "$MoSe_2$ layer formation at $Cu(In, Ga)Se_2$/Mo interfaces in high efficiency $Cu(In_{1-x}, Ga_x)Se_2$ solar cells," *Jpn. J. Appl. Phys.*, vol. 37, p. L71, 1998.

[141] B.L. Evans and P.A. Young, "Optical absorption ans dispersion in molybdenum disulphide," *Proc. Roy. Soc. London A*, vol. 284, no. 1398, p. 402, 1965.

[142] S.H. El-Mahalawy and B.L. Evans, "Temperature dependence of the electrical conductivity and Hall coefficient of 2H-MoS_2, $MoSe_2$, WSe_2, and $MoTe_2$," *Phys. Stat. Sol. B*, vol. 79, p. 713, 1977.

[143] A. Mallouky and J.C. Bernède, "Characterization of $MoSe_2$ thin films," *Thion Solid Films*, vol. 158, p. 285, 1988.

[144] M. Bodegård, K. Granath, L. Stolt, and A. Rockett, "The behaviour of Na implanted into Mo thin films during annealing," *Sol. En. Mat. Sol. Cells*, vol. 58, p. 199, 1999.

[145] J. Morales, J. Santos, and J.L. Tirado, "Electrochemical studies of lithium and sodium intercalation in $MoSe_2$," *Solid State Ionics*, vol. 83, p. 57, 1996.

[146] J.H. Scofield, S. Asher, D. Albin, J. Tuttle, M. Contreras, D. Niles, R. Reedy, A. Tennant, and R. Noufi, "Sodium diffusion, selenization, and microstructural effects associated with various Mo back contact layers for CIS-based solar cells," in *Proceedings of the 1st World Conference and Exhibition on Photovoltaic Energy Conversion, Waikoloa, Hawaii, USA, 1994*, p. 164, IEEE, Piscataway, New Jersey, USA, 1994.

[147] C. Martin, I. Martin, V. Rives, and P. Malet, "Changes in the structure of TiO_2 supported molybdena induced by Na doping," *J. Catalysis*, vol. 147, p. 465, 1994.

[148] R.B. Somoano, V. Hadek, and A. Rembaum, "Alkali metal intercalates of molybdenum disulfide," *J. Chem. Phys.*, vol. 58, no. 2, p. 697, 1973.

[149] J.V. Acrivos, W.Y. Liang, J.A. Wilson, and A.D. Yoffe, "Optical studies of metal-semiconductor transmutations produced by intercalation," *J. Phys. C*, vol. 4, p. L18, 1971.

[150] J. Matheis, J. Rostan, U. Rau, and J.H. Werner, "Carrier collection in $Cu(In, Ga)Se_2$ solar cells with transparent ZnO:Al back contacs," in *Technical Digest of the 14th International Photovoltaic Science and Engineering Conference, Bangkok, Thailand, 2004* (?, ed.), p. 593, ?, 2004. to be published in Solar Energy Materials & Solar Cells.

[151] Ch.-H. Fischer, H.-J. Muffler, M. Bär, T. Kropp, A. Schönmann, S. Fiechter, G. Barbar, and M.Ch. Lux-Steiner, "Spray-ion layer gas reaction (ILGAR)

- a novel low-cost process for the deposition of chalcopyrite layers up to the micrometer range for photovoltaic application," *J. Phys. Chem. B*, vol. 107, p. 7516, 2003.

[152] A. Kylner, J. Lindgren, and L. Stolt, "Impurities in chemical bath deposited CdS films for $Cu(In, Ga)Se_2$ solar cells and their stability," *J. Electrochem. Soc.*, vol. 143, no. 8, p. 2662, 1996.

List of Figures

List of Tables

Abbreviations and symbols

α	absorption coefficient
A	constant
ALD	atomic layer deposition
AM	air mass
AES	Auger electron spectrometry
BF	bright field
CBD	chemical bath deposition
CCD	charge-coupled device
CGS	$CuGaSe_2$
CIGS	$Cu(In, Ga)Se_2$
CIS	$CuInSe_2$
CL	cathodoluminescence
CTEM	conventional transmission electron microscopy
d	thickness
d_{hkl}	lattice spacing
dc	direct current
D	diffusion constant
DF	dark field
η	efficiency
E	energy
E_{CB}	conduction-band energy
E_{g}	band-gap energy
E_{F}	Fermi energy
E_{VB}	valence-band energy
EBIC	electron-beam induced current
ED	electron diffraction
EDX	energy-dispersive x-ray spectrometry

EELS	electron energy-loss spectrometry
EF	energy filtered
FEG	field-emission gun
FF	fill factor
I	transmitted intensity
I_0	initial intensity
IPE	Institut für Physikalische Elektronik, University of Stuttgart, Germany
ITO	indium tin oxide
j	current density
j_{sc}	short-circuit current density
PIPS	precision ion polishing system
PL	photolumniscence
ρ	density
rf	radio frequency
R	reflectance
SAED	selected-area electron diffraction
SIMS	Secondary ion-mass spectrometry
SKPM	scanning Kelvin probe microscopy
STEM	scanning transmission electron microccopy
STM	scanning tunnelling microscopy
t	time
t_{sel}	selenization duration
T	transmission
TCO	transparent conducting oxide
TEM	transmission electron microccopy
UPS	ultra-violet photoelectron spectrometry
V	voltage
V_{oc}	open-circuit voltage
XPS	x-ray photoelectron spectrometry
ZSW	Zentrum für Solarenergie- und Wasserstoff-Forschung, Stuttgart, Germany

Curriculum Vitae

Daniel Abou-Ras

Date of birth:	20 January 1975
Place of birth:	Freiburg im Breisgau, Germany
Nationality:	German

Sep 1985 - Jun 1994	Wentzinger-Gymnasium, Freiburg, Germany
Aug 1994 - Oct 1995	Civil Service at the Diakonie hospital, Freiburg, Germany
Oct 1995 - Sep 1996	Stay abroad in Israel
Oct 1996 - Sep 2002	Studies of physics at the University of Freiburg, Germany; diploma thesis on dye-sensitized solar cells with charge-accumulation layers; graduation as Dipl. Phys.
Jan 1997 - Jun 1999	Assistant at the Fraunhofer Institute for Solar Energy Systems, Freiburg, Germany
Sep 1999 - Jul 2000	Studies of physics at the Université Paris-Sud, Orsay, France (ERASMUS scholarship)
Jan - Jun 2000	Research stay at the Institute d'Électronique Fondamentale, Orsay, France (mixed-valence manganites)
Apr 2001 - Sep 2002	Assistant at the Materials Research Centre, Freiburg, Germany
Oct 2002 - present	Research collaborator and Ph.D. student at the ETH Zurich, Switzerland
Nov 2002 - present	Unsalaried work for the academic job-exchange board Telejob (www.telejob.ch); as accountant, president and CEO; board member of the Association of Academic Staff at ETH Zurich (AVETH)
Mar 2005	MRS Graduate Student Gold Award, received at the MRS 2005 Spring Meeting, San Francisco, CA, USA